UNIVERSITY OF PARMA

Ph.D. IN BIOTECHNOLOGY AND LIFE SCIENCES

CYCLE XXXIII

Biomolecular characterization of a rat model of lung fibrosis: investigation of its translational potential in Idiopathic Pulmonary Fibrosis (IPF)

Coordinator:

Professor Marco Ventura

Tutor:

Professor Simone Ottonello

PhD Student: Martina Bonatti

Academic years 2017/2018 – 2019/2020

ABSTRACT

Idiopathic pulmonary fibrosis (IPF) is a progressive, multifactorial and irreversible pulmonary disorder that leads, in a few years, to the progressive deconstruction of lung architecture, until death for respiratory failure or associated comorbidities[1]. Despite recent progresses, effective pharmacological treatments are not yet available for the treatment of this disease, except for two recently approved drugs that can slow-down lung function decline without stopping or reverting the disease[2]. Although several models of lung fibrosis have been set-up recently, a fully comprehensive preclinical animal model capable of recapitulating all the characteristic features of human IPF is not yet available. Despite some limitations, the bleomycin (BLM)-induced lung fibrosis murine model is currently viewed as the best preclinical approximation of IPF[3,4]. The presently limited understanding of IPF, along with the lack of predictive preclinical models have hindered the development of novel effective drugs for this complex disease.

In this Ph.D. work, performed in collaboration with Chiesi Farmaceutici, I characterised and optimised a BLM-induced lung fibrosis rat model, with the aim to obtain a multidisciplinary view of the model and expand the currently limited knowledge of the mechanisms underlying lung fibrosis. An additional, related aim was to gain a deeper understanding of the translational potential of the BLM rat model with regard to the human disease, particularly its usefulness for the development of better drugs against IPF. To achieve these goals, a whole transcriptomic analysis and histopathological characterization were performed in two key *in-vivo* experiments: a time course study and a pharmacological curative study with nintedanib, one of the IPF approved drugs. The multilevel analysis that accompanied these two experiments showed that the pathological condition induced by BLM in the rat model set-up in this Ph.D. thesis work, closely resembled lung fibrosis and was responsive to a reference, clinically approved IPF drug. Moreover, transcriptomic analyses performed in this experimental set-up revealed the existence of specific gene signatures, enriched in pathways and processes that hold great promise as new IPF biomarkers and therapeutic targets.

TABLE OF CONTENTS

1. Introduction

1.1 The Interstitial Lung Diseases and Idiopathic Interstitial Pneumonias

Interstitial lung disease (ILD) is a wide-ranging term which includes more than 200 different lung disorders with similar features regarding the clinical, radiological and physiological profile, but large variability in terms of clinical course, treatment and prognosis[5]. ILDs are characterised by variable degrees of inflammation and fibrosis that affect the pulmonary interstitium[5,6] and they can be divided in inflammation dominant diseases or in fibrosis dominant diseases. However, the most important classification that distinguished ILDs in two major classes is the presence or the absence of a known cause of disease induction. ILDs that have an uncertain or unknown origin are defined as idiopathic interstitial pneumonias (IIPs)[6].

The IIPs are a group of ILDs of unknown causes which in turn include seven disease categories as defined by the statement of 2002 and following update of 2013 of the American Thoracic Society/European Respiratory Society (ATS/ERS)[7,8]. These categories shared various features, but they are adequately dissimilar from one another to be nominated as separate pathological entities[9]. All the disease categories are reported in in the following table.

Table 1.1. Principal histologic and radiologic characteristics of the different IIP categories (table adapted from the American Thoracic Society/European Respiratory Society International Multidisciplinary Consensus of the 2002[9]).

DISEASE CATEGORIES	Histologic Patterns	Usual Radiographic Features
Idiopathic Pulmonary Fibrosis (IPF)	Usual Interstitial Pneumonia (UIP)	Basal-predominant reticular abnormality with volume loss
Nonspecific Interstitial Pneumonia (NSIP)	Nonspecific Interstitial Pneumonia (NSIP)	Ground glass and reticular opacity
Cryptogenic Organizing Pneumonia (COP)	Organizing Pneumonia (OP)	Patchy bilateral consolidation
Acute Interstitial Pneumonia (AIP)	Diffuse Alveolar Damage (DAD)	Progressive diffuse ground glass density/consolidation
Respiratory Bronchiolitis-Associated Interstitial Lung Disease (RB-ILD)	Respiratory Bronchiolitis (RB)	Bronchial wall thickening; ground glass opacity
Desquamative Interstitial Pneumonia (DIP)	Desquamative Interstitial Pneumonia (DIP)	Ground glass opacity
Lymphoid Interstitial Pneumonia (LIP)	Lymphoid Interstitial Pneumonia (LIP)	Reticular opacities, nodules

1.2 Idiopathic Pulmonary Fibrosis (IPF)

Among the IIPs, idiopathic pulmonary fibrosis (IPF) is the most common category. Physicians and radiologists of the mid-20st century had chosen the name Idiopathic Pulmonary Fibrosis for describing a fibrotic condition of the lung with unknown cause, but the ATS International Consensus Statement of 2000 provided a more complete and structured definition defining IPF as a "specific form of chronic fibrosing interstitial pneumonia limited to the lung"[7]. As mentioned in **Table 1.1**, the histopathological pattern that categorises patients with IPF is the UIP. The hallmark feature of this pattern is the presence of damaged areas heterogeneously distributed within healthy tissue, characterized by epithelial cell hyperplasia, undressing basement membrane, architectural alteration in the form of honeycomb and/or fibrosis, and accumulation of fibroblasts foci (cluster of proliferating fibroblasts capable of producing areas of new fibrosis)[2]. The distribution of this abnormalities presents not only a spatial heterogeneity, intended as damaged areas alternate with areas of normal tissue, but they also show a temporal heterogeneity[2,10]. This latter concept refers to the simultaneous presence of areas of active/new fibrosis, characterized by fibroblast foci and areas of old fibrosis, represented by large agglomerates of collagen and extracellular matrix[2,10]. In this pattern, the alveolar walls are so compromised by the presence of excessive deposition of collagen and other components of the extracellular matrix (ECM) that they lose their original structure. In the final phases of the disease, the lung architecture is totally altered and the alveoli are replaced with large airspaces, filled by inflammatory cells and dense scars, that greatly decreases lung function[11]. The histological and radiological appearance of the UIP pattern are reported in **Figure 1.1**.
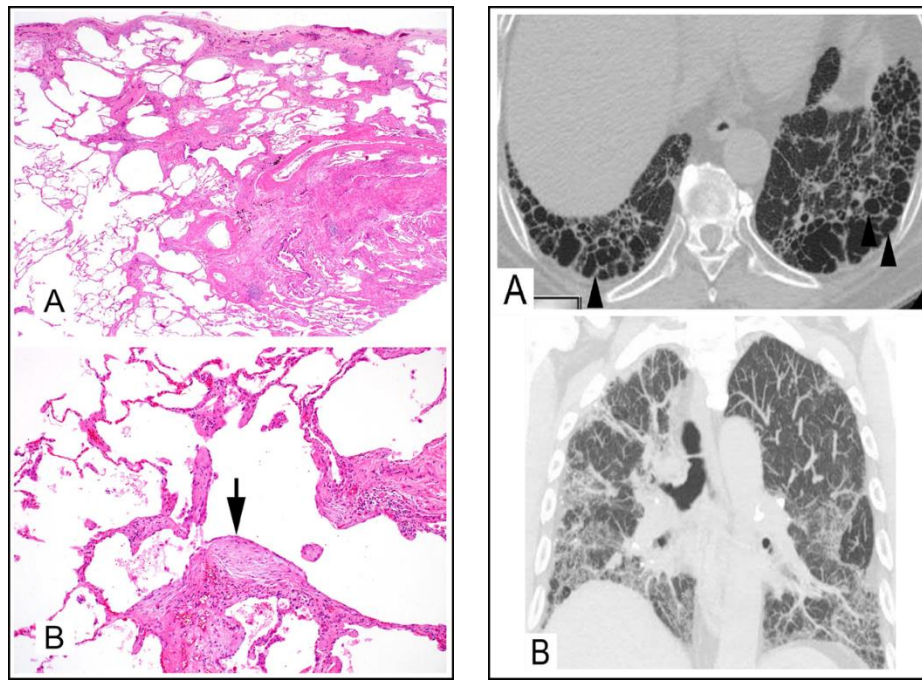
Figure 1.1 *Histological (left panel) and radiological (right panel) appearance of the UIP pattern of IPF (images and description taken from Smith et al. 2017[10]).* ● *Image A of left panel, shows the spatial heterogeneity of the pattern UIP, displaying areas of lung fibrosis (lower right part of the image) alternate with areas of normal lung parenchyma (lower left part of the image). In the **image B** of the same panel, the black arrow highlights a fibroblast focus, that, according to the authors, represents a hallmark of the temporal heterogeneity.* ● *The **image A of the right panel** display a sagittal CT section of an IPF patient, and the **image B** display a coronal maximum intensity projection of the same lungs. These images are reported by Smith and colleagues to show the "typical apico-basilar gradient of fibrosis" and the high concentration of honeycombing structure existing in lung bases.*

1.2.1 Symptoms and Diagnosis

There are many symptoms leading to the suspect of IPF, but the clinical features of the disease are considered nonspecific. For example, the initial symptoms, which usually lead a patient to ask medical attention, are unproductive cough, dyspnoea and shortness of breath during exercise[10,12], and unfortunately in many cases these manifestations are attributed to other diseases or aging. Then, as the disease advances, patients show shortness of breath even during the normal life activities and the cough degenerates[12]. Raghu and colleagues in the guidelines for diagnosis and management of IPF suggest to consider IPF in all adult subjects with an incomprehensible dyspnoea, cough, bibasilar inspiratory crackles (a defined sound produced by the lungs during breathing that recall the sound of Velcro) and finger clubbing (deformation state of all the fingers which assume a

shape similar to drum sticks)[13]. Another typical clinical evidence of IPF is the progressive decline in forced vital capacity (FVC), that represents the primary endpoint of clinical studies. Technically, the FVC is the amount of air volume (measured in litres) that can be breathed out applying a maximal effort, after a full inspiration. Data originated from some clinical trials reported, in IPF patients treated with placebo, a range from 0.15 to 0.22 L in annual decline of FVC[14,15].

Since the clinical symptoms are nonspecific, the diagnosis of IPF is a complex procedure and it results from a progressive exclusion of other lung diseases through the evaluation of different clinical evidence by an experienced multidisciplinary team[13]. The diagnosis is articulated in a series of steps, and after the exclusion of other ILDs with a known aetiology (e.g., forms of lung fibrosis associated with environmental exposures, drug toxicity etc.), the identification of the UIP pattern is essential to proceed to the diagnosis. UIP pattern can be identified with the use of High-Resolution Computed Tomography (HRCT) or in combination with surgical lung biopsy (SLB), when possible[13].

Considering the criticalities connected to SLB, the ATS/ERS/JRS/ALAT 2011 guidelines clarify the situations in which this type of procedure should be considered and that is when the HRCT provides images that lead to the identification of patterns classified as "possible UIP" or "inconsistent UIP".[13] The current guidelines are globally accepted and when the UIP pattern is easily recognised the diagnostic procedure proceeds quite rapidly. However, in most cases the diagnosis of IPF is very difficult and often it requires many years before being issued with negative effects on the patients. This aspect highlights the need to identify new biomarkers useful for early diagnosis and predictive of disease progression, to allow prompt intervention with pharmacological treatments.

1.2.2   Clinical Course of The Disease

There are three different clinical courses of the disease defining the IPF progression, but at the beginning it is very difficult to associate each patient with a specific clinical course[13]. The three types of disease progression listed below, could be considered as distinct phenotypes of the disease[13]:

- Relatively stable progression: patients can survive more than 5 years;

- Fluctuating progression: patients alternate periods of relative stability to sudden episodes of worsening of the clinical conditions, called acute exacerbations of IPF (AE-IPF);

 - Accelerated progression: patients get drastically worse in a very short time and survive no more than 1 year from the diagnosis[16].

1.2.3 Risk Factors

As I reported in the first paragraph, IPF is a disease with unknown causes, and for this reason it includes the word "idiopathic" in the name. Despite this, there are a series of risk factors that have been identified as potential agents able to increase the chances of developing IPF. Risk factors are important aspects to consider in a heterogeneous disease such as IPF, because they can help to define sub-populations of patients for personalized medicine, to accelerate the time of diagnosis and to better understand the pathogenesis of the disease.

The typical IPF patient is a man (almost the 70% of all diagnosed cases world wide), with a mean age of 65 years old (large scale studies have proved an increased incidence and prevalence of IPF in patients with an old age) and with a past as a smoker (a history of cigarette smoking is very common in IPF, with prevalence between 41–83%). These information put the attention on the risk factors that probably have the greatest impact on the disease: age, gender and constant contact with cigarette smoke[17]. Ageing contributes to the pathogenesis of IPF probably through an irregular telomere shortening and a senescent phenotype of lung fibroblasts that alters the response of this type of cells to the lung injury, while the exact contribution of the gender is still unlcear[17]. On the other hand, it is easier to understand the contribution of cigarette smoke to the pathogenesis of IPF. The effects that this agent has on lung health are well known, and many of them are associated with some key point of the development of the disease. Besides the direct irritating effect on the lung epithelium, cigarette smoke can overexpress genes of the EMT and act negatively on important

biological processes, like telomere shortening and stress of the endoplasmic reticulum. Moreover, it has been shown that nicotine is able to induce the production of TGF-β[17].

Other well-known risk factors are some genetic variants that in some cases lead to a familial clustering of pulmonary fibrosis[18] and they are listed below:

- Genes of the surfactant proteins: SFTPA2 (Pulmonary surfactant-associated protein A2); SFTPC (Pulmonary surfactant-associated protein C); ABCA3 (ATP Binding Cassette Subfamily A Member 3);

- Genes related to the maintenance of telomers: TERC (Telomerase RNA Component); TERT (Telomerase Reverse Transcriptase);

- Genes implicated in the host defense: MUC5B (Mucin 5B, Oligomeric Mucus/Gel-Forming). Other important and well known risk factors are schematized in **Figure 1.2.**
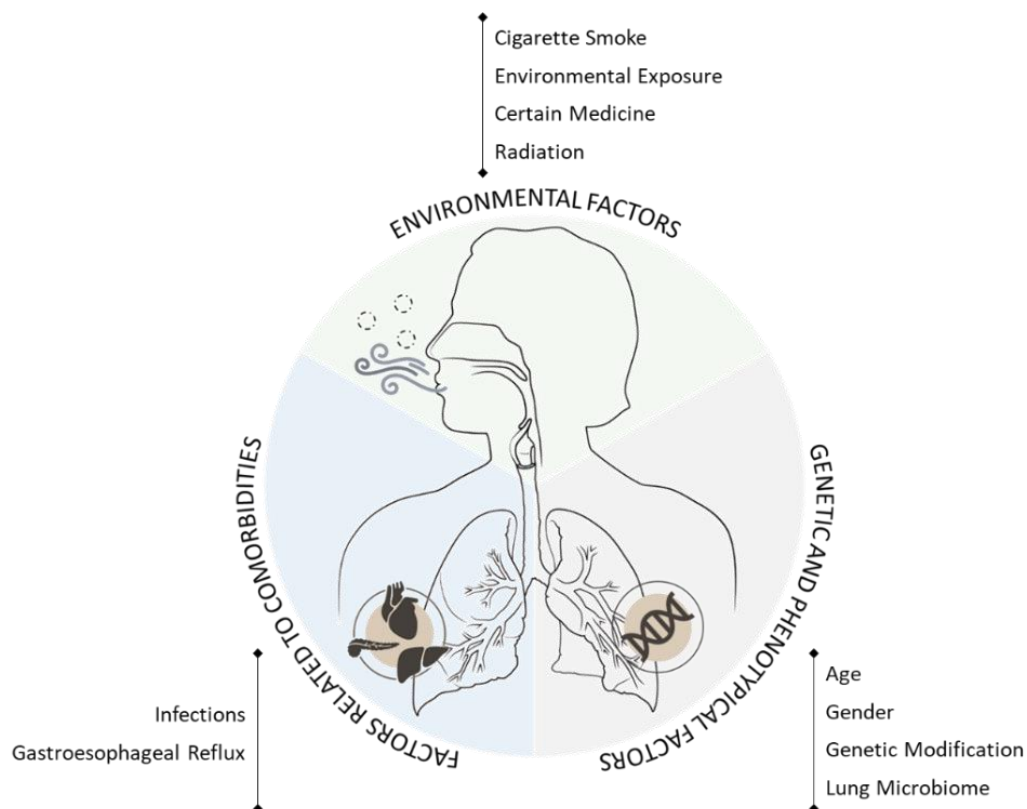
Figure 1.2 *Graphical representation of the most important risk factors associated to the onset of the disease, divided in three different categories (images realized based on information reported by Zaman and colleagues[17]).*

1.3 Epidemiology of IPF

IPF is usually regarded as a rare disease, but recently, the scientific/medic community described an increased incidence and prevalence of the disease among different populations and it has been reported that IPF is the most common form of ILD[19]. The incidence and prevalence of IPF fluctuate considerably between countries and years because the epidemiologic data are influenced by external factors (like ethnicity, exposure to environmental or other risk factors, etc.) and depend on the method of data collection and on the applied diagnostic criteria. For these reasons the epidemiologic data must be considered as estimated[13]. Data obtained in the first years of the XX century reported an overall prevalence of 20.2 cases per 100,000 population for male and 13.2 cases per 100,000 population for female, while the incidence rate was 10.7 per 100,000 persons/years for male and 7.4 persons/years for female[20]. However, as reported at the beginning of the paragraph, the epidemiological rates of IPF are constantly increasing. Indeed, studies conducted in USA in the first years of the new millennium reported a prevalence rate of 14-42.7 per 100,000 persons and an incidence rate of 6.8-16.3 per 100,000[21]. Moreover, a recent study conducted in UK reported that the incidence increased 78% between 2000 and 2012, and the prevalence was doubling[22]. Thinking in global terms, the most recent data report that the rate of world-wide incidence is between 2.8–9.3 per 100,000/year in North America and Europe, while in Asia and South America are significantly lower[19]. The progress of the disease is inexorable, and the mortality for this disease is considered high; generally patients die after 3-5 years from diagnosis[21] and the 5-year survival is estimated at around 20%[1].

1.4 Pathogenesis of IPF

Despite the growing accumulation of data and clinical evidence of the disease, the pathogenesis of IPF remains not completely understood. However, the prevailing hypothesis leads to a series of studies that clarified the role of different type of cells and pathways[23]. The normal wound healing process consists of a sequence of overlapping molecular and cellular events that occur through the integration of dynamic processes involving soluble mediators, blood cells and parenchymal cells with the aim to repair and restore the function of damaged tissues. In adult organisms this process is not exactly the same employed during embryonic formation of new tissues and so results in a partial restoration of the tissue with formation of scars[23]. For reasons still not well known, the healing process is completely altered in IPF probably due to aging and genetic predisposition, leading to considerable tissue remodelling and the replacement of functional tissue with permanent fibrous scar tissue[4]. Current hypothesis proposes a pathogenesis that could be schematized in 3 different point, that temporally follow one another:

- Damage of the alveolar epithelium;

- Defective tissue regeneration of the damaged alveolar space;

- Deconstruction of lung architecture due to an excessive deposition of fibrotic material.

All these events inevitably lead to a progressive loss of pulmonary physiology and function[23,24] and are schematized in **Figure 1.3**.

1.4.1 Damaging of The Alveolar Epithelium - The Role of The Alveolar Epithelial Cells

Recent evidence suggests that IPF is the result of the occurrence of different and repeated micro-injuries at level of the alveolar epithelium. Indeed, both intrinsic (i.e. genetic and aging) and environmental (i.e. cigarette smoke, pollution and infections) factors have been linked to injury/disfunction of alveolar epithelial cells that serves as an early initiating event leading to the ongoing tissue remodelling and fibroproliferation that triggers the pathology[4]. All the above

reported risk factors do not necessarily lead to the development of IPF, but unquestionably they increase the individual chances of developing it[25].

The alveolar epithelium is composed by a monolayer of alveolar epithelial cells (AECs) covered with surfactant and leaning on the epithelial basement membrane, that communicate directly with the endothelial cells; this disposition allows the rapid diffusion of gas between alveolar airspace and blood[24]. The AEC are divided into two types based on their shape and function:

- AECs type I (flat morphology): these cells are the most represented within the alveolus and are highly specialized in gas exchange[23].

- AECs type II (cuboidal morphology): these cells are responsible of lung homeostasis through the secretion of surfactant components, interact with fibroblasts and mediate the reparative processes of the alveolar epithelium thanks to their ability to proliferate and differentiate[24].

Epithelial cell injury leads to apoptosis of the AECs type I revealing an uncovering basal lamina and in a normal context the AECs type II proliferate and differentiate to repair the damaged alveolar epithelium. This process is altered in IPF, so the AECs, left after the damage, are unreasonably activated and produce a series of profibrotic stimuli, particularly transforming growth factor-β (TGF-β), that cause the recruitment of inflammatory cells and fibroblasts[23], which begins a complex chemical cross-talk with the AECs[24]. Under the influence of different pro-fibrotic growth factors and cytokines, AECs drop the typical features and markers of fully differentiated epithelial cells and become mesenchymal cells with reduced cell adhesion and increased motility in a well-known process called epithelial to mesenchymal transition (EMT)[23]. These altered alveolar epithelial cells, release a series of mediators that regulate the activation and proliferation of fibroblasts[24].

1.4.2   *Defective Tissue Regeneration of The Damaged Alveolar Space - The Role of Fibroblasts*

Fibroblasts are the most abundant cells of the connective tissue and they are also the most active in producing tropocollagen, an intermediate step of collagen formation, and ground substance, an

unstructured gel-like component, composed by fibronectin and glycoproteins, that is placed between cells and fibres in connective tissue[26,27]. These cells possess a flat and elongated shape and play a central part in wound healing. Indeed, after an injury, fibroblasts migrate to the site of damage and facilitate the healing process producing ECM components as a scaffold for the regeneration of the tissue[26,27]. These cells can be activated by different signalling mediators, among which the major player is TGF-β, and after the activation they can proliferate, migrate and/or transform into another cellular type, but in some cases, for reasons still unknown, they get out of control of their activity and produce a pathological fibrotic response.

After injury, as mentioned before, fibroblast can differentiate in another type of cell, the myofibroblast, a contractile and ECM secretory cell, with a marked resistance to apoptosis, that give an essential contribute to the wound healing process, but that can severely impairs the functionality of the tissue when contraction and ECM accumulation become disproportionate, like in IPF[23,28]. Despite the main original source are resident fibroblasts, myofibroblasts can originate also from bone marrow-derived progenitors of fibroblasts, and from AECs that have undergone EMT[29].

In IPF lung fibroblasts and myofibroblasts are principally clustered near the air–tissue interface in the form of fibroblast foci and they are responsible for the active new production of ECM components that gradually are accumulated in the tissue destroying the articulated structures of the lung[23].

1.4.3   Deconstruction of The Lung Architecture - The Role of The Extracellular Matrix

In a healthy pulmonary context, the extracellular matrix (ECM) structure and turnover are dynamically tuned to optimize physiological function. However, during the pathological context of IPF there is an excessive production of the matrix proteins, which do not undergo any turnover[24]. The regulation of ECM turnover is achieved by two different group of proteins, the matrix

metalloproteinases (MMPs) and tissue inhibitors of metalloproteinases (TIMPs) and an unbalance in the abundance and expression of these two groups of proteins is registered in IPF patients[24].

This disparity in production/disruption of matrix components leads to a massive accumulation of complex and messy ECM structure that results in the physical distortion of the lung structures, with consequent effects on pulmonary functions[23].

The production, deposition and remodelling of ECM products, like different types of collagen, is achieved by fibroblasts and myofibroblasts in response to different mediators. However, the negative effect of collagen production is not due only to its accumulation in the lung tissue, but also to its uncorrected processing and organization which make the lung stiffer as the disease progresses[23]. It has been reported that the stiffness of the ECM can have an influence on the activity of lung fibroblasts. Indeed, if fibroblasts are grown in-vitro on a substrate with increased stiffness, they may differentiate to myofibroblasts and display other pro-fibrotic features like increased proliferation and collagen production[30]. It is also demonstrated that, in IPF, the altered ECM can induce changes in the gene expression of different types of collagen and ECM remodelling enzymes in fibroblasts[30]. Finally, altered ECM organization and mechanical properties can create a fibrogenic niche that by modulating the phenotypes and destinies of the residing cells further promotes the progression of lung fibrosis[31]. All these results show a possible positive feedback loop between pro-fibrotic cells (like activated fibroblasts) and pathological ECM in which, as defined by Fernando J. Martinez and colleagues "the fibrotic ECM is both a cause and a consequence of fibroblast activation"[30].

1.4.4   The Contribution of Inflammation to Pathogenesis

Inflammation plays a significant part in IPF pathogenesis, but its role is controversial and this is partially due to the failure of different clinical trials of anti-inflammatory drugs for IPF treatment (this part will be discussed in paragraph 1.5.1)[32]. Nevertheless, new insights highlight an important

contribution of inflammation to IPF pathogenesis. Several cytokines and different inflammatory cells types have been implicated in the pathology, but their exact role remains unclear. For example, it is known that M2 macrophages possess a pro-fibrotic asset and promote wound healing through the secretion of several growth factors, like TGF-β, and production of components of the ECM; indeed, they are widely present in fibrotic lung tissue[32]. Despite this, there are sub-populations of M2 macrophages that can induce a degradation of ECM through the MMPs, so macrophages can have pro- or anti-fibrotic effects, which depending on the tissue context[32].

Certainly, IPF does not result from an initial inflammatory insult but the role of inflammation in orchestrating existing fibrotic responses and its relationship to environmental and genetic factors, disease outcomes, and potential therapies deserve further in-depth investigations.
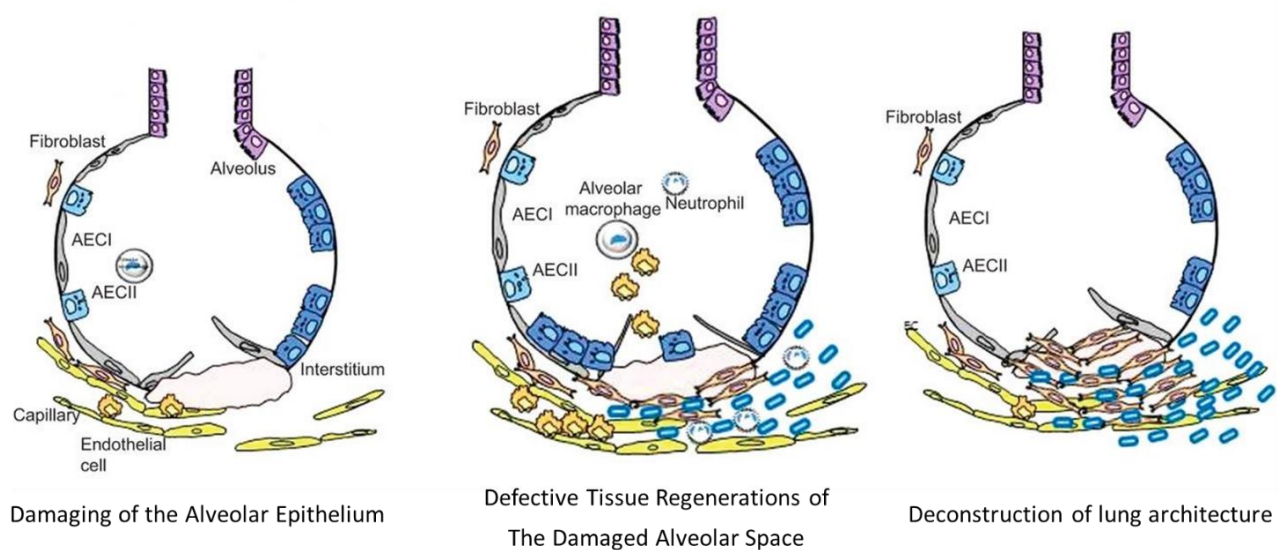
Figure 1.3 *The different steps of the pathogenesis of IPF (images adapted and modified from Wuyts and colleagues, 2013[33]).*

1.5 Therapeutic Solutions Available for The Treatment of IPF

The therapeutic approaches attempted in clinical trials for IPF have undergone a huge change over the past few years thanks to the new knowledge on the pathogenesis of the disease and to a better definition of the diagnostic criteria. However, most of the clinical trials over the last decade has proved unsuccessful for lack of efficacy or harmful effects, and in the history of the disease only two drugs have been approved by the major drug regulatory agencies for the treatment of IPF: pirfenidone and nintedanib. However, current antifibrotic treatment halts disease progression but does not cure the disease itself. The only possibility to improve the survival of patients with IPF is the lung transplantation, but this option is available only for a small portion of selected patients. For this reason the medical need in IPF it has always been very high[1].

1.5.1 Before The FDA-Approved Antifibrotic Drug - The Chronic Inflammatory Disorder Paradigm

At the beginning of the history of IPF, scientists and physicians thought that pulmonary fibrosis was a direct consequence of a long process of inflammation. Based on best evidence available at that time, researchers reasoned that the damage suffered at the level of the alveoli would lead to the beginning of a strong interstitial inflammatory response that was the cause of fibrosis seen in IPF[34]. For all these reasons, in the past, the standard of care for patients with IPF was a therapy based on anti-inflammatory and immunosuppressive drugs, nevertheless, none of these therapies proved effective in treating the disease[1,35] and in a phase III clinical trial based on anti-inflammatory and immunosuppressive the study was stopped due to increased mortality[36].

Despite the failure of these types of treatments, it is undeniable that inflammation play a role in the disease. Some inflammatory cells can act as pro-fibrotic mediators and other types of cells can have anti-fibrotic proprieties. Moreover, emerging evidence suggest that inflammation could have a different role in different sub-populations of IPF patients, and this could be one of the reasons why anti-inflammatory drugs have not worked in the past[32].

1.5.2   The New Paradigm of IPF - The Age of The Anti-Fibrotic Drugs

The ineffectiveness of the anti-inflammatory and immunosuppressive therapies in addition to the new paradigm of the disease, which puts at the centre of pathogenesis an abnormal wound healing process resulting in a scarred lung parenchyma, had led the scientific community to shift the attention towards molecules with antiproliferative and antifibrotic properties. On the wave of this new information in the last 10 years two different anti-fibrotic molecules were approved for the treatment of IPF, as I mentioned at the beginning of this paragraph. Unfortunately, neither of the two drugs is able to completely block the disease, but they are only able to slow it down as reflected by lung function trend towards improvement[1].

Pirfenidone (5-methyl-1-phenyl-2-(1H)-pyridone (complete chemical structure is reported in **Figure 1.4**) is a small molecule with a pleiotropic effect developed by InterMune Inc. (now Roche) and approved by the two major drug agencies, the European Medicines Agency (EMA) and the American Food and Drug Administration (FDA) in 2011 and 2014 respectively. The most common commercial names attributed to this compound are Esbriet® and Etuary®, and it is usually sold for oral administration. Pirfenidone possesses anti-inflammatory, anti-fibrotic and antioxidant properties, which laed to the decrease of collagen accumulation and to the inhibition of fibroblast-myofibroblast transition, but the exact mechanism of action of the molecule is still unknow[1,35]. From several *in-vitro* studies, it is supposed that this drug acts on tumour necrosis factor alpha (TNF-α) and on the TGF-β pathways, and probably is the modulation of these two pathways that carried out respectively the anti-inflammatory and antifibrotic actions of the molecule[1]. At a clinical level, Pirfenidone proved to be able to decrease FVC decline and reduce the rate of acute exacerbations, which affect IPF patients[2]. Despite the beneficial properties, the molecule has a series of adverse effects that weaken the precarious condition of patients. The most frequent side effects described are gastrointestinal problems, cutaneous rash and photosensitivity[2].

Nintedanib (ethanesulfonic acid;methyl 2-hydroxy-3-[N-[4-[methyl-[2-(4-methylpiperazin-1-yl)acetyl]amino]phenyl]-C-phenylcarbonimidoyl]-1H-indole-6-carboxylate, complete chemical structure is reported in **Figure 1.4**) is a small molecule that acts at intracellular level and is reported to inhibit a series of multiple tyrosine kinases receptors where the most affected are: fibroblast growth factor receptor (FGFR), platelet-derived growth factor receptor (PDGFR) and vascular endothelial growth factor receptor (VEGFR)[37]. Tyrosine kinases regulate a series of cell processes that include differentiation, growth, metabolism, and apoptosis; indeed, the compound originates from a chemical lead optimisation programme started to identify inhibitors of the angiogenesis for the treatment of cancer. However, in chronic fibrotic proliferative diseases such as IPF, the simultaneous activation of different receptor tyrosine kinase pathways suggested that a multi-target inhibitor of these receptors could be a good therapeutic option for fibrotic disease[38]. For this reason, the molecule was tested for use as an antifibrotic drug and given the positive results of phase III clinical trials, nintedanib was approved for the treatment of IPF by the EMA and FDA, in 2015 and 2014 respectively. The molecule was developed by Boehringer Ingelheim under the commercial name of Ofev® and Vargatef®.

At a biological level, Nintedanib, mainly inhibiting VEGFR, FGFR, and PDGFR, interferes with a series of biological processes that are important for the development and progression of IPF, among which, the fibroblast to myofibroblast transition (FMT) and the excessive production and deposition of ECM components, like collagen[1]. At a clinical level, nintedanib can reduce the incidence of acute exacerbations (AE) and the risk of disease progression, can improve the FVC decreasing its rate of decline, and overall, can improve the quality of life[1,2]. Nintedanib has some adverse effects mainly affecting the gastro-intestinal tract, which in some cases require the use of antiemetic and antidiarrheal drugs to improve the physical conditions of the IPF patients[1,2].

Pirfenidone   Nintedanib
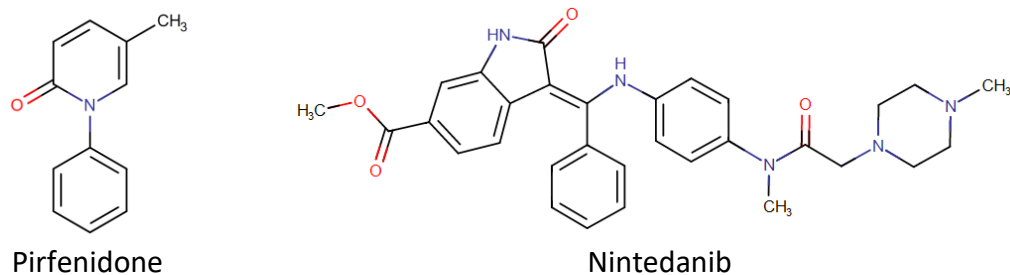
Figure 1.4 Molecular structure of pirfenidone and nintedanib. Image obtained on DRUGBANK website.

Since the two drugs have very similar beneficial effects, one wonders which drug could be better prescribe to a patient with IPF. Actually, there aren't head-to-head randomized clinical trials to evaluate which of the two antifibrotic drug have the major effect in treating IPF, so the decision was mainly focus on what is more appropriate for each single patient. Pirfenidone is to be preferred to nintedanib in patients with a high risk of bleeding, due to the inhibiting effect on VEGF receptor signal of nintedanib[2]. On other hand, nintedanib may be considered instead of pirfenidone in patients that possess dermatologic pathology or that cannot avoid sun exposure, because, as mentioned before, this molecule produces photosensitivity and cutaneous rash as a side effect[2].

1.5.3   Non-Pharmacological Approaches and Novel Therapies

As the disease progress, the symptoms greatly affect the patient's quality of life, so to help them and ameliorate their living conditions a series of non-pharmacological treatment are suggested, like pulmonary rehabilitation and supplemental oxygen therapy. Pulmonary rehabilitation is a non-pharmacological approach used for improving the functional capacities of lungs affected by different chronic diseases. Practically is a program that acts through exercise training on respiratory muscles, like thoracic stretch and expansion during deep-breathing exercises. In pathologies such as IPF, this type of approach has been shown to improve respiratory symptoms and ameliorates the quality of life[1,2]. Also, the supplemental oxygen therapy proved to be a treatment that could improve respiratory symptoms, exercise endurance and quality of life in IPF patients, although there are not many studies supporting this type of treatment with solid data[1,2].

The need of more effective drugs, also with an adequate safety profile, with the increasing understanding of IPF patho-biology, had led to an exponential growth in the number of clinical trials of novel molecules and combination therapy[1]. And in the last years, a series of clinical trials evidenced promising solutions in terms of safety and efficacy, the most significant are reported in **Figure 1.5**.
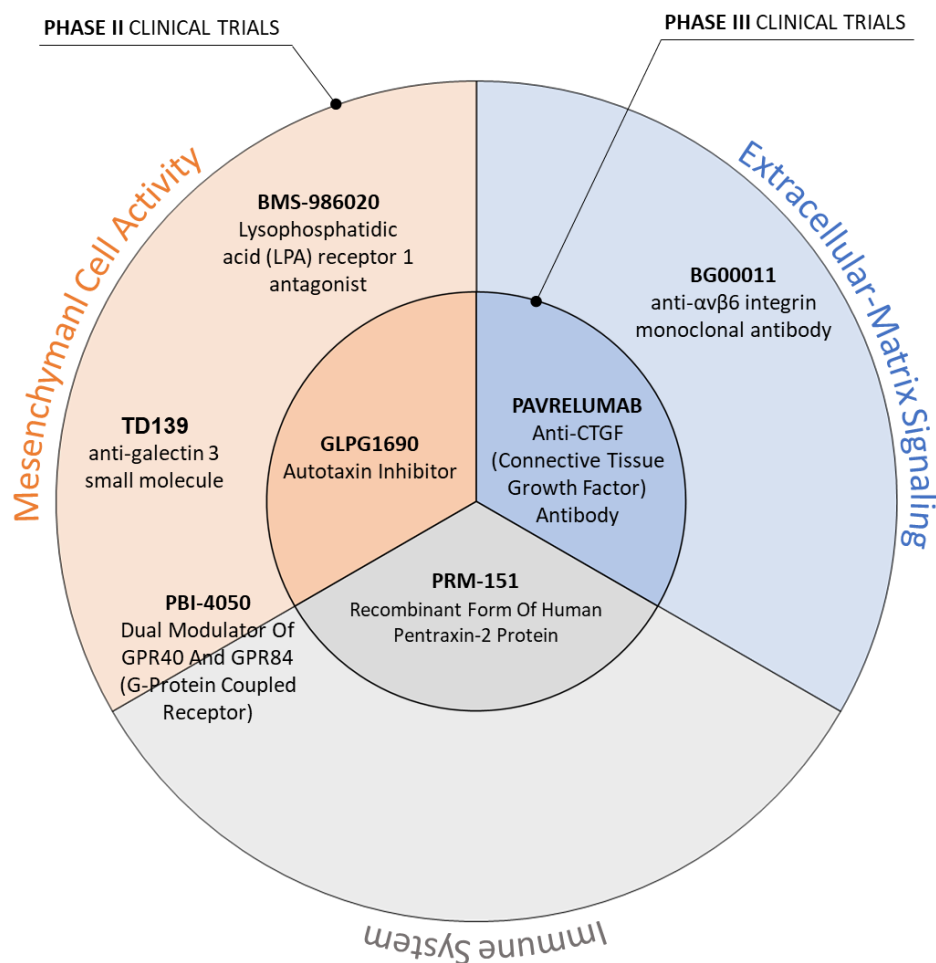
Figure 1.5 Most advanced promising drug candidates for IPF taken from Saito, S et al 2019[2], divided on the basis of the clinical phase in which they are actually located (information taken from https://www.clinicaltrials.gov/ct2/home) and of the target on which they interfere.

1.6 Preclinical Models to Study Lung Fibrosis

Modelling human IPF is difficult due to its complex aetiology and pathogenesis. However, most of our understanding of this disease is based on experimental models that have changed over time, increasing in complexity and accuracy as quickly as the increasing of new pathological evidence and the availability of new and emerging technologies. To date, many models of lung fibrosis are available to be used in preclinical studies, both *in-vitro* and *in-vivo.*

1.6.1 In-vitro Models of Pulmonary Fibrosis

During the pathogenesis of IPF, different type of cells contributes in a different way to the onset and progression of the disease. The primary and simplest *in-vitro* model of lung fibrosis evaluates one cell type at a time in a two-dimensional (2D) environment. In this type of model, widely used to investigate cells response to different agents, immortalized cells (like non-small cell adenocarcinoma: A549 and lung fibroblasts: IMR-90s) are cultured on plastic or glass substrates and stimulated with a pro-fibrotic agent (the most used is the TGFβ) or extracellular matrix cues. In this way, the model provides an easy and fast way to profiling cells for pro-fibrotic read-outs with or without different treatments and has the advantage to be suitable for development of high throughput *in-vitro* assays for screening of anti-fibrotic agents. Despite this, it remains an unsatisfactory approach since it investigates the response of cells that are completely isolated from their biological context. For this reason, during the years *in-vitro* models of lung fibrosis are improved with the aim of give a more complex view of what happens to the cells in a pro-fibrotic environment, where different types of cells communicate each-other and are grown on a complex biological matrix. Complex matrices of biological origin have therefore begun to be used to cultivate cells in an environment similar to the lung one and the cultures gradually moved from 2D to 2.5D and to 3D, until the realization of very complex models.

Among 3D models deserve a mention the models based on hydrogel systems, lung organoids, lung -on-a-chip and precision cut lung slices (PCLS). Hydrogels are water-base polymers with different grade of cross-linking that are employed as scaffold for *in-vitro* models, specially fibroblast cultures, to reproduce the natural structure of the ECM[39]. Collagen type I-based hydrogels *in-vitro* models are very helpful in the study of fibroblast behaviour when exposed to chemical and physical stimuli induced by the ECM[39].

Lung organoids are multi-cellular structures capable of self-assembly similarly to what is happening in the various embryonic phases of pulmonary development[40] and they can be produced from different type of pluripotent stem cells. These organoids can mimic the typical cell-cell and cell-matrix complicated interactions existing inside the lung, and for this reason they represent a significant improvement respect to 2D cultures[39].

Lung-on-a-chip are 3D tissue models replicating not only the lung structure with all the cell and matrix interactions, but also the mechanical stimulus of breathing and blood flow.

Among the *in-vitro* models, the one proved to be most promising for screening compounds and supporting preclinical studies is the PCLS *ex-vivo* model. PCLs are obtained from fresh human/animal lung tissue filled with liquid agarose and subsequently cut into 300–1000 μm thick slices for *in-vitro* culture; in this way the tissue remains as it was inside the original organ[41]. This model replicates cell-cell and cell-matrix interactions present in the lung structure better than other 3D in vitro models, and even if it doesn't reproduce lung functions, it represents the best combination of biological complexity, high-throughput capacity and tissue culture period[41]. Considering all these aspects, a combination of preclinical studies performed in ex vivo (PCLS) and in vitro models is always needed to better mimic the fibrogenesis process in human.
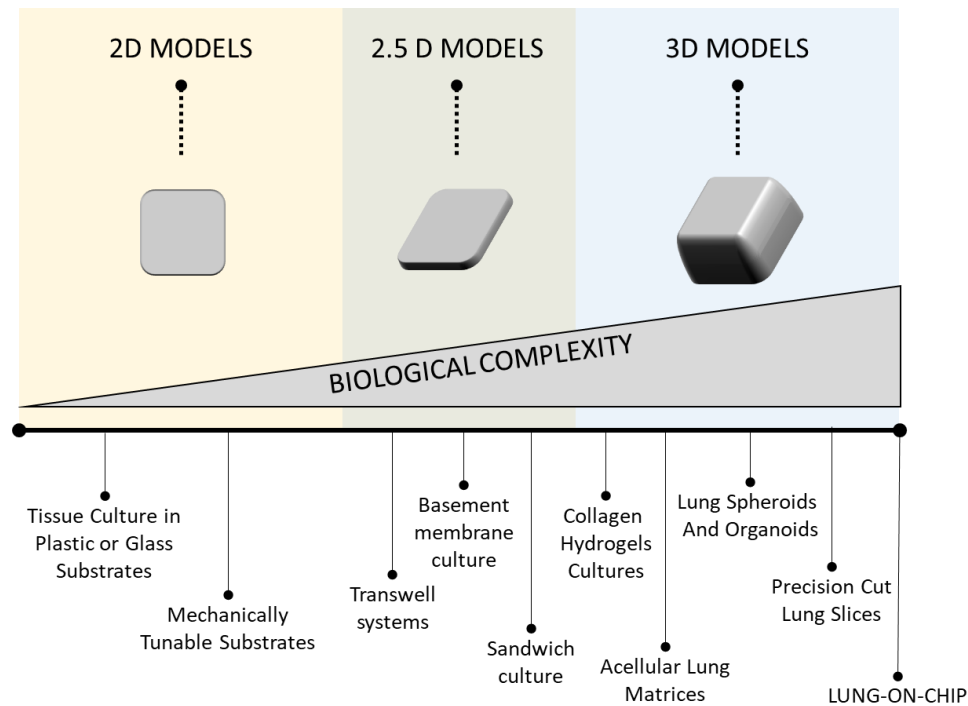
Figure 1.6 *Recap of all the in-vitro models of lung fibrosis, divided based on complexity and dimensionality (images produced based on information reported by Sundarakrishnann and colleagues[41]). The biological complexity of the model increases gradually adding biological matrices, 3D environment, biological interactions and mechanical stimulus typical of the lung function.*

1.6.2   In-vivo Models of Pulmonary Fibrosis

Despite the development of innovative *in-vitro* models with the addition of an increasing level of biological complexity, through the use of new technologies and biological matrices in the culture media, these models don't yet possess the same physiological environment of the *in-vivo* models and all the intricate cellular and matrix connections and stimulus that are present in living tissues.

Although various *in-vivo* lung fibrosis models have been used in recent years, a fully satisfactory animal model capable of recapitulating all the characteristic features of human IPF and showing features of progressive disease is not yet available. However, animal models of lung fibrosis are essential for the drug development process, both at target validation and drug discovery level. Moreover, the clinical trials of pirfenidone and nintedanib have been successfully completed and the preclinical experiments conducted in animals have contributed to the approval[4].

Although cases of spontaneous lung fibrosis are known in some common mammalians (like dogs, horses, cats and donkeys), rodents remain the most used preclinical models for lung fibrosis, since in these species fibrotic lesions have a rapid onset and their duration enable drug testing[3]. Moreover, rodents, being small animals, are easy to house and handle and the management costs are reduced compared to larger species[3]. Generally, among rodent models, the mouse is the first-line animal to study human diseases and to test safety and efficacy of therapeutic molecules, especially for the small size (respect for example to rat and guinea pig) that allows large-scale studies using few amounts of drugs to be tested. The mouse is widely used because it possesses anatomical and physiological characteristics very similar to humans; moreover its genome is totally sequenced and present over 95% of similarity to that possessed by humans[42].

Despite the mouse being the most studied and used animal model in the last years, recently the rat was widely used to substitute or complement it, in case the mouse model is considered inappropriate or insufficient to study and test a specific scientific question. This is possible because today a lot of information and techniques, which previously were exclusive only of the mouse, are available also for the rat[43]. Even if these two animals look similar, at taxonomic level, they are two different species, and they possess also a different genera, this means that there are many years of evolution that separate them and that they have distinct biological and behavioural characteristics[43].

In some cases, the rat is preferred by researchers, because its proportions enable to collect a greater amount of biological fluids and tissue; this is important for example when it is necessary to perform different techniques on a single sample. Moreover, in several cases, it is more comparable to the corresponding human condition and for this reason it represents a better model for some types of disease[43]. For example, in studies of cognition and memory, the rat was preferred to other rodent

species because its neuronal physiological systems involved in learning and memory its more advanced and so referable to human condition[43].

Regarding the study of IPF, at present, the "Official American Thoracic Society Workshop Report about the Use of Animal Models for the Preclinical Assessment of Potential Therapies for Pulmonary Fibrosis" recommends the mouse as a first-line animal, but it is reported that the rat model may have a histopathology that is more related to the human IPF, even if the response to lung injury is analogous[3]. Indeed, in the same report, the rat is recommended as the second species, putting the attention on the possibility to use rats to support the target validation and drug discovery process or in case of an impossibility to use the mouse[3]. Considering that a single model doesn't resemble all the characteristic of the disease, the possibility to expand the model with two or more animal models of different species could be a good choice to improve the efficacy of preclinical studies[4]. Among the various experimental agents that are being used to induce lung fibrosis, bleomycin (BLM) is the most common, due to its fast action leading to the early appearance of histopathological alterations that closely mimic the acute phase of the disease[4], but there are other agents available that are capable to induce lung fibrosis and they are briefly discussed in **Table 1.2**.

Table 1.2 *Common agents employed to produce lung fibrosis in rodents and description of the main characteristics of their related animal model[4,44].*

AGENT OF INJURY Name of the model	PRINCIPAL CHARACTERISTICS	ADVANTAGES & DISADVANTAGES
FLUORESCENT ISOTHIOCYANATE FITC-Induced Lung Fibrosis	FITC, an artificial chemical compound, acts as a hapten and binds to lung proteins forming a storage that produces a prolonged injury that leads to lung fibrosis.	**ADV: ●Robust and Persistent Fibrosis; ●Possibility to visualize the areas of lung fibrosis with immunofluorescence imaging.** DIS: ●Absence of IPF-like lesions (i.e. fibroblast foci); ●Variability due to batch and particle size; ●No-clinical relevance.
ASBESTOS Asbestos-Induced Lung Fibrosis	The injection of asbestos fibres into the lungs produces fibrosis through the induction of a programmed cell death of the alveolar epithelial cell, polarization of macrophages, and overproduction of pro-fibrotic cytokines.	**ADV: ●Similarity with IPF features; ● Fibrosis similar to an occupational form of human lung fibrosis.** DIS: ●Significant amount of time required to develop fibrosiss; ●In some cases the damage is irregularly distributed between lungs.
SILICA Silica-Induced Lung Fibrosis	Silica particles, administrated directly in the lungs, are ingested by macrophages that produce pro-fibrotic cytokines, growth factors and TGFβ. Fibrotic nodules are formed around the particles.	**ADV: ●Persistent Fibrosis; ●Fibrosis similar to an occupational form of human lung fibrosis.** DIS: ●Absence of IPF-like lesions (i.e. fibroblast foci); ●Fibrosis is strain-dependent; ●Problem with the route of administration.
RADIATION Radiation-Induced Lung Fibrosis	Radiation hits pneumocytes (both type I and II) and leads to a direct damage of the DNA with consequent cell death and attraction of macrophages in the area of injury.	**ADV: ●Persistent Fibrosis; ●Fibrosis similar to the occupational form of human fibrosis.** DIS: ●Absence of IPF-like lesions (i.e. fibroblast foci); ●Long time to develop lung fibrosis; ●Fibrotic effect dependent on inflammation and less on TGF-β;

In addition to the models reported in the table, there are other models obtained using genetic techniques (i.e. viral vectors or genetic engineering). The most employed include the over production of cytokines, where the TGFβ was the most widely used (but also some interleukin and TNF-α). These models result in an early inflammatory response followed by fibrosis, but frequently they produce variable type of injury that consequently leads to problems in the reproducibility of severity and extent of the lesions[4]. Moreover, in these models the biological environment is altered

and there is a non-physiologic amount of some gene products that can alter the natural pathways involved in the development of lung fibrosis and may provide a distorted picture of the pathogenesis[44]. An alternative *in-vivo* model of lung fibrosis that has been developed is the humanized mouse model of IPF. In this particular animal model, diseased cells obtained from IPF patients, like altered fibroblasts, were inoculated in severe combined immune deficient (SCID) mice and after several weeks the mice develop pro-fibrotic features visible both at histological and biomarker level[45]. Despite the model being quite promising, the fibrosis requires a long period of development, moreover, it is not easy to find cells from IPF patients[45].

Recently are growing in importance also the age-related models, considering that IPF is an age-related disease as explained in paragraph 1.2.3. Indeed, it has been demonstrated that older mice are more inclined to developed lung fibrosis when exposed to pro-fibrotic stimuli[4]. Moreover, a model with a specific deletion of one telomeric gene, demonstrate that telomere dysfunction (one of the principal characteristics of aging) in type II AECs is sufficient to cause lung fibrosis[46].

1.6.3 The Bleomycin-Induced Lung Fibrosis Models

As mentioned in the previous paragraph, the BLM-induced lung fibrosis rodent model is the most used animal model to study pulmonary fibrosis and it is also the most employed in preclinical studies during the drug development process for IPF.

BLM is an antibiotic molecule produced by *Streptomyces verticillus* (complete structure is reported in **Figure 1.7**) that was employed as a chemotherapeutic agent for the treatment of different types of cancer and that has revealed a pro-fibrotic activity, especially in lungs, in oncologic patients after a series of intravenous treatments[4]. Given the capabilities of the molecule to produce lung fibrosis in human, BLM was used to modelling pulmonary fibrosis in rodents to better understand the mechanisms of fibrotic lung disease like IPF[47].

BLM produces single and double-strand DNA breaks in cells and thus causes a pseudo-apoptotic process, that is an apoptosis characterized by a rapid fragmentation of the genetic material[47]. The lungs are most affected by the cytotoxic effect of the molecule because they possess lower levels of a BLM-inactivating enzyme (BLM hydrolase) with respect to other organs[4]. The mechanism of DNA strand break is still unknown, but it has been proposed that BLM is able to chelate metal ions, producing a pseudoenzyme that reacts with oxygen leading to an overproduction of reactive oxygen species (superoxide and hydroxide free radicals) able to cleave the DNA structure[4]. This type of damage leads in a couple of days to the programmed death of the alveolar epithelial cells, that attracts different types of inflammatory cells producing an excessive accumulation of inflammatory infiltrate in the site of injury after about 7 days after the administration of the molecule[4]. This primary inflammatory phase leads to the activation, proliferation and migration of fibroblasts, which start to produce an excessive and increasing amount of ECM, a process that ends with the formation of lung fibrosis, usually three-four weeks after the administration of BLM[47].
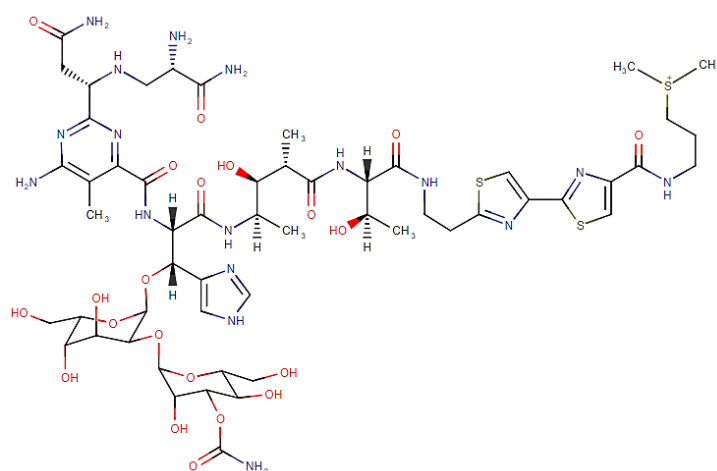
Figure 1.7 *Molecular structure of BLM. Glycoprotein produced by a natural biological process. Image obtained on DRUGBANK website.*

However, the pattern of lung fibrosis is dependent by the route of administration of BLM. The intratracheal delivery is the most commonly employed because the treatment is limited to the lung and so it recapitulates better the human phenotype, but recently also the oropharyngeal

administration is used for the same reason[4]. In addition to topic administration, in literature described also systemic routes of administration (subcutaneous, intraperitoneal and intravenous) of BLM that produce an initial injury at the level of the pulmonary vascular endothelium, before damaging the alveolar epithelium, reflecting similar features of human bleomycin-induced pneumonitis[48].

Considering the temporal heterogeneity of IPF and the hypothesis that repeated events of lung injury are responsible of the disease development, various publications proposed the repetitive administration of BLM to mimic some of the findings noted in the human disease. In particular, a repeated intratracheal administration of BLM has been shown to produce a more robust and long-lasting response that could at least in part reproduce IPF progression[3]. Regardless of the similarities between human pulmonary fibrosis and the bleomycin model of lung fibrosis, the model generates many controversies in the scientific community related to its ability to mimic IPF. This is mainly linked to the aspect that BLM induces a reversible fibrosis, while in IPF patients the fibrosis is progressive and irreversible. The use of repetitive administration of the compound can only partially solve this problematic[47], this characteristic of the model may offer an opportunity to study the biological way to resolve lung fibrosis[48].

Moreover, the histopathology is not fully consistent with the hallmark features of IPF, even if fibroblastic foci have been described, the distribution of fibrosis is different (basal, sub-pleural distribution for IPF vs distribution focalized around bronchi)[47,48], and the effect of bleomycin is strain-dependent, especially for the mouse[48]. Finally, the BLM model is characterized by an initial and severe inflammatory phase, and pharmacological interventions that stop this phase are often protective, while IPF is not considered an inflammatory disease and inflammatory drugs has been revealed ineffective[47,48].

Despite the explained disadvantages, the murine model of intratracheal BLM delivery is currently viewed as the best preclinical approximation of IPF, mimicking important elements of the progressive fibrogenesis seen in IPF patients, which allowed to understand some important features of lung disease and contributed to the approval of two drugs for the treatment of IPF[3,4].

Regardless the limits that animal models may have, we need to select the best of them in terms of translatability and management, and characterize it as thoroughly as possible to understand what "questions" can be asked to the model to solve problems related to the disease that cannot be ask to human patients, as clearly explained by Jun Tashiro and colleagues[4]: "An animal model is a simple representation of a complex biology system. Critics focusing on the reasons why an animal model cannot fully reproduce human disease are not helpful and do not elicit a solution". Despite the growing ethical need to reduce the number of animals used in research, without animal models, complicated diseases such as IPF, could remain without a pharmacological solution for a long time. The idea to replace it with innovative and refined *in-vitro* models is promising and encouraging, but there is still a long way to go.

1.7 "OMICS" Approaches to Study Complex Diseases

In the last years, the overall analysis of the whole transcriptional response of the genome to diverse stimuli or pathological conditions has been one of the most employed methods to study human diseases at the molecular level and thanks to this approach, many therapeutic targets and diagnostic biomarkers and have been identified in numerous human diseases[49].

Considering the limited understanding of IPF pathogenesis the omic analysis of the transcriptome profiling and other advanced molecular biology approaches may provide detailed information on the dysfunctional cellular processes associated to complex pathologies such as fibrotic degeneration, including causative cues and new potential drug targets. Indeed, different transcriptomic approaches with varying levels of deepness and complexity have been successfully applied in recent years to IPF, as reported in the review of Vukmirovic and Kaminski[50]. Although many points remain to be clarified - most notably the causative ranking of the dysfunctional processes revealed by transcriptome analyses and their potential for translation to preclinical models - these studies have allowed the identification of a number of new candidate genes and pathways that may be extremely relevant for the onset and progression of the disease. These genome-wide IPF investigations have been flanked by companion studies performed in various murine models of BLM-induced lung fibrosis[51–56], topic that will be discussed in more detail in the paragraph 5 dedicated to the discussion. Despite the reportedly higher histopathological similarities between IPF and BLM-induced rat fibrosis and the possibility to use rats to support some critical points of the drug development process, only a few studies have been reported in the latter preclinical model[51,52], . In addition, none of the rat studies conducted so far has employed a data-mining strategy exploring time-dependent variations in transcriptional signatures to gain potentially more insightful information on the progression of BLM-induced lung damage.

2. AIM OF THE WORK

IPF is a multifactorial pulmonary disease, still poorly understood and difficult to diagnose, with an unpromising fate for patients who are affected. None of the medications available on the market is able to definitively cure the disease, because the only two drugs approved for the treatment of IPF (pirfenidone and nintedanib) can only slowdown the rate of decline in lung function. All these considerations make IPF a disease with a high clinical need. In addition, the preclinical models available to study this disease are not capable to completely reproduce the features of the human disease and consequently they hinder the identification of mechanisms of action with a clear positive effect on the outcome of the disease.

Despite these limitations, knowledge on IPF has improved in recent years, mainly through the use of several types of molecular biology approaches performed on animal models of lung fibrosis. Undeniably, reliable and translationally relevant animal models of lung fibrosis are indispensable tools for the development of new drugs and also represent an essential component for a better understanding of etiopathogenetic mechanisms underlying the disease.

Therefore, the main goal of my Ph.D. thesis work was to characterise and optimise a BLM-induced lung fibrosis rat model, in order to acquire a deeper understanding of the model and expand the currently limited knowledge on the mechanisms underlying lung fibrosis. An additional related aim was to pinpoint the translational potential of the model with regard to the human disease, particularly as a tool for the development of new drugs against IPF. To achieve these goals, a whole biomolecular and histopathological characterization was performed in two experimental setups:

- A time course study: to understand the most important features that characterize the evolution, progression and the partial resolution of BLM-induced lung fibrosis;

- A pharmacological curative study with one of the IPF approved drugs in order to evaluate the impact of an anti-fibrotic drug on the model and its functional validation.

The parallel analysis of gene expression, histology and biomarkers evaluation, provided the opportunity to integrate and correlate different types of information, with the potential to improve the features of the animal model for drug-response studies and to contribute to the development of novel therapies and diagnostic biomarkers in the fight against IPF.

3. MATERIALS AND METHODS

3.1 In-vivo Activities

3.1.1 Substances

- Bleomycin: bleomycin sulphate from *S. verticillus,* 1.5-2.0 units/mg solid powder for solution (Sigma-Aldrich, St. Louis, Missouri, USA);

- Clinically-approved bleomycin: bleomycin sulphate, 15000 International Units (IU), powder for solution for injection/infusion (Baxter Oncology GmbH, Germany);

- Nintedanib (NINT): Nintedanib free base 100 mg/kg (Carbosynth, Compton UK);

- Methyl Cellulose: Methyl Cellulose dry powder (Sigma-Aldrich, USA);

- RNAlater™: aqueous, non-toxic tissue storage solution for the immediate RNase inactivation and RNA stabilization (Sigma-Aldrich, USA);

- Formalin solution: formalin 10%, Q Path®, buffered 10% (VWR Q-Path Chemicals, Radnor, Pennsylvania, USA).

3.1.2 Animals

Male Sprague-Dawley (SD) rats, weighing 200-250 g at arrival, were supplied by Charles River Italia, Lecco (Italy). Animals were housed two or three per cage and lighting in the holding room was controlled (light 7.00-19.00, dark 19.00-7.00). The animals had free access to controlled tap water and to a standard certified laboratory rat diet (VRF1, Special Diets Service, UK, for Charles River Italia). The animals were checked for abnormalities or signs of health problems after arrival in the animal facility. Before any use, animals followed an acclimatisation period of at least 5 days. No prophylactic or therapeutic treatment was administered to any animals during the acclimatisation period. All the experimental procedures and conditions involving experimental animals were reviewed and approved by the local ethics committees and authorized by the Italian Ministry of Health (authorization number 33/2016-PRPAH) and were performed in full compliance with the international European ethics standards in conformity to directive 2010/63/EU, Italian D.Lgs

26/2014, and the revised "Guide for the Care and Use of Laboratory Animals" (Guide for the Care and Use of Laboratory Animals, 1996).

3.1.3 Intratracheal Administration of Substances - Procedure

The animals underwent a cycle of gas anaesthesia (sevoflurane 4% in oxygen) and were placed supine on an animal support stand that had an inclination of about 45° with respect to the work surface (supine head up). Rubber bands were attached to the incisor teeth, holding the mouth open and a small otoscope (Welch-Allyn NY, U.S.A.) accessorized with an intubation speculum (Hallowell EMC, Pittsfield, MA, USA) was used to visualise the trachea. Substances were instilled intratracheally using a patented device that works by manual pressure and allows to administer an air-free concentrated plume of liquid aerosol directly into the lungs (Penn Century Microsprayer - Penn-Century Inc., Philadelphia, USA). The injection of liquid substances was followed by injection of 0.3 ml of air to facilitate the equally distribution of substances throughout the lungs.

3.1.4 Oral Administration of Substances - Procedure

The oral administration was performed via oral gavage in a volume of 10 ml/kg. Animals were gently handled and placed vertical head up and immobilized, in this way the procedure can be carried out without causing damage to the animal. The procedure was performed with a flexible plastic cannula attached to a syringe. The cannula was passed through the pharynx and inserted directly into the oesophagus and the liquid substances were administered directly into the stomach of rats.

3.1.5 Time Course Study - Workflow

BLM or its vehicle (saline solution, SAL) for controls animals, were instilled intratracheally at the starting point of the protocol and after 4 days. The dose used for the BLM was 2 UNIT/kg/0.6 ml. During the time course study, the body weight of the animals was measured twice a week. The animals were sacrificed at different time points from the first administration of BLM (T0), as described in the **Figure 3.1** and different biological samples were collected. For each time-point,

except for T0, two groups (BLM and SAL) of 8 animals were treated (at the end of experiment in the BLM-T56 group the animals were only 6 due to the mortality recorded during the experiment, see paragraph 4.1.1). Moreover, at T0, 6 untreated animals (naïve), representative of the basal conditions, were sacrificed. All animals were anaesthetised with sevoflurane (4% in oxygen) and sacrificed by bleeding from the abdominal aorta.
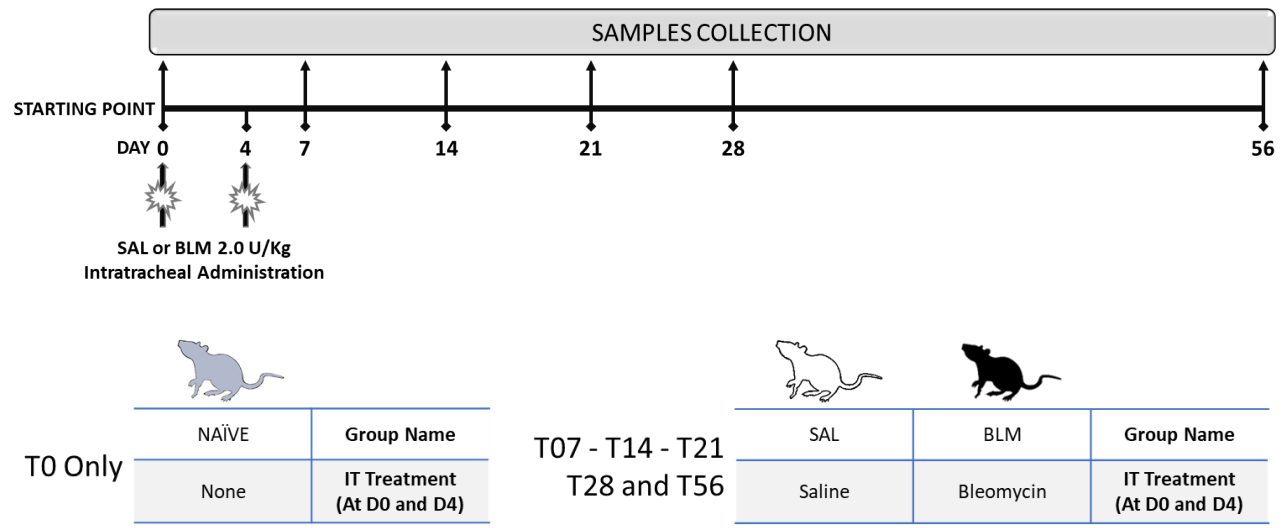
Figure 3.1 Time Course Study – Experimental Scheme and Group Classification

3.1.6 Dose Response Study with a Clinically Approved BLM - Workflow

A clinically approved BLM (Baxter) was instilled intratracheally at the starting point of the protocol and after 4 days, at the dose of 0.5, 1.0 and 2.0 UNIT/kg/0.6 ml. The control group received SAL only. During the experiment the body weight of the animals was measured twice a week. The animals were sacrificed 28 days after the first administration of BLM (T0) and the different biological samples were collected. The experimental plan included 4 groups of 8 animals: SAL, BLM 0.5, BLM 1.0 and BLM 2.0 (at the end of experiment in the BLM 2.0 group the animals were only 6 due to the mortality recorded during the experiment, see paragraph 4.4.1), a graphical explanation of the experimental schemes and of the groups classification is reported in **Figure 3.2**. All animals were anaesthetised with sevoflurane (4% in oxygen) and sacrificed by bleeding from the abdominal aorta.
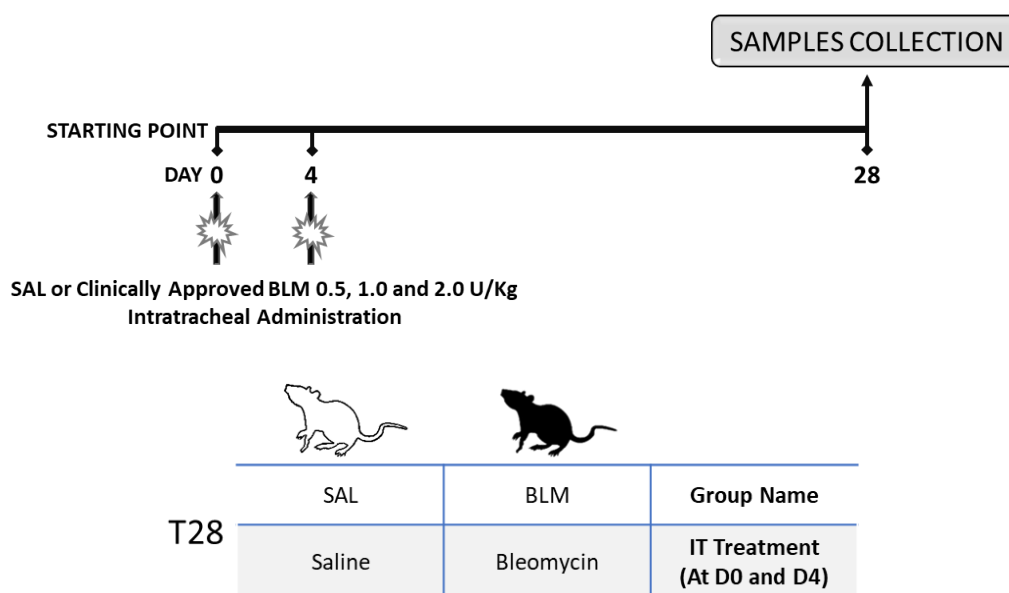
Figure 3.2 *Dose Response Study - Experimental Scheme and Group Classification*

3.1.7 Curative Protocol Study with Nintedanib - Workflow

A clinically approved BLM (Baxter) was instilled intratracheally at the starting point of the protocol and after 4 days, at the dose of 1.0 UNIT/kg/0.5 ml. The control group received SAL only. The therapeutic protocol started seven days after the first administration of BLM and then continued for three weeks. At day 7, the animals treated with BLM were randomized and divided in two groups of 6 animals, one of them received nintedanib and the other received its vehicle for all the three weeks of treatment. The protocol consisted of an oral daily treatment with nintedanib 100 mg/kg, prepared by suspension in methyl cellulose (0.5% in water), that represented therefore the vehicle. The animals treated with SAL received the vehicle for all the three weeks of treatment. During the experiment the body weight of the animals was measured twice a week. The animals were sacrificed 28 days after the first administration of BLM and different biological samples were collected. To summarize, 3 groups of 6 animals were included in this experiment: SAL, BLM and NINT. A graphical explanation of the experimental schemes and of the group classification is reported in **Figure 3.3**. All animals were anaesthetised with sevoflurane (4% in oxygen) and sacrificed by bleeding from the abdominal aorta.
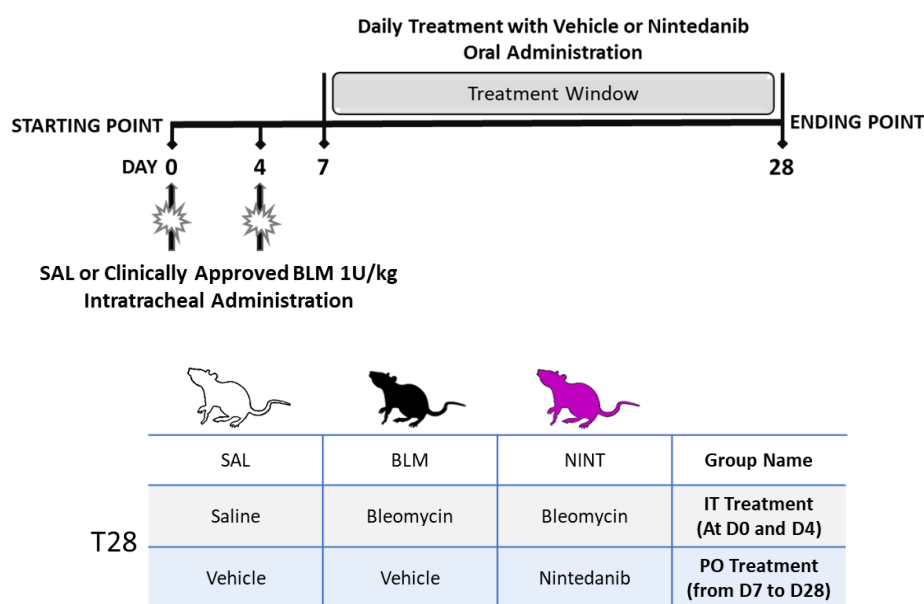
**Figure 3.3** *Curative Protocol Study with Nintedanib - Experimental Scheme and Group Classification*

3.1.8   Biological Samples Collection

- BLOOD: The whole blood was collected by cardiac puncture and analysed with an automated cell counting system (Sysmex Partec Italia - DASIT S.p.A., Italy).

- LUNGS: The whole lungs were removed, washed in saline solution and weighted. After this step, the 4 different right lung lobes were separated and stored in RNAlater™ for gene expression analysis or in liquid nitrogen for the protein analysis, while the single left lung lobes were designated for histological analysis and underwent a fixation process. Indeed, the left lungs were insufflated, through a tracheal cannula, with an amount of 10% formalin buffer necessary to expand the lungs (~4 ml) and stored in containers filled of 10% formalin buffer.
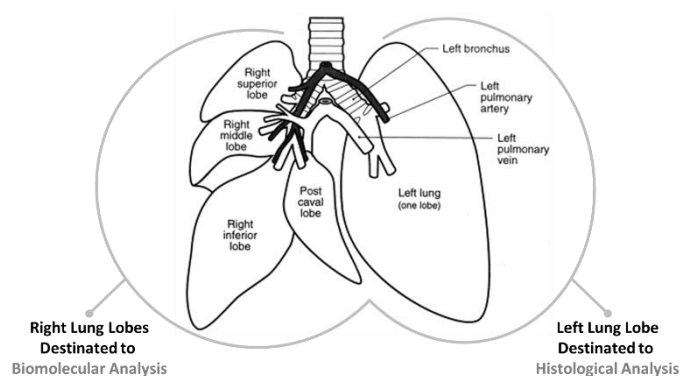
Figure 3.4 Graphical Representation of the Lung Processing. Image adapted from Sumihiko Nawata et al. (1997)[57].

3.2 In-vitro Activities

3.2.1 Biological Sample Processing

- Sample processing for RNA extraction: The RNAlater-conserved tissues were homogenized in QIAzol® Lysis Reagent (phenol-based reagent supplied by QIAGEN, Netherlands) with gentleMACS™ Dissociator (Miltenyi Biotec, Germany).

- Sample Processing for Protein analysis: frozen right lobes were weighed and homogenized in 10 ml of ice-cold 1X PBS per g of tissue, with gentleMACS™ Dissociator (Miltenyi Biotec, Germany) and Polytron PT2500E (Kinematica, Switzerland). After this step, the total right lung homogenates were aliquoted, and one aliquot was subjected to a three freezing/thawing cycles using liquid nitrogen and a thermal bath set at 37°C to lyse cells. Moreover, the cell lysates were centrifuged at 5000 g for 10 minutes to remove debris. This final lysate was used for all the protein analysis, while the homogenate without the subsequent procedures was used for the analysis of hydroxyproline (HYP).

- Sample Processing for Histological analysis: the left lung lobes, conserved in formalin solution, were paraffin included to obtain sections representing the long axis of the entire parenchyma. Each longitudinally oriented lung's left lobes were cut to obtain 5 μm thick slides and after that they were stained with Masson's Trichrome histological staining (activities performed by an external laboratory - Laboratory Unit of prof. F. Quaini and C. Lagrasta, Department of Medicine and Surgery, University of Parma, Italy). Masson's Trichrome is a histological staining protocol that employs three different reagents for staining collagen and ECM, muscle fibres, and erythrocytes. This staining protocol is usually employed for distinguishing cells from adjacent connective tissue, and for this reason it is highly used to evaluate pulmonary fibrosis and other connective tissue disease. Masson's Trichrome is one of the staining protocols recommended for the histologic assessment of morphology in lung fibrosis related studies[3].

3.2.2   Protein Analysis

The total amount of HYP, as a measure of collagen content, was determined with the Hydroxyproline Colorimetric Assay Kit (Sigma MAK008, USA) according to the manufacturer's protocol. The total amount of Serpin Family E Member 1 (Serpine1, alias Plasminogen Activator Inhibitor Type 1 (PAI-1)) and Thrombospondin 2 (Thbs2) were assessed with commercial ELISA kit (Sandwich Elisa Kit technology) according to the manufacturer's protocol.

For Thbs2 the kit used was: Rat THBS2 / Thrombospondin 2 (Sandwich ELISA) ELISA Kit - LS-F6601 (LSBio, Seattle, Washington, USA) and for Serpine1: Enzyme Immunoassay for Rat Plasminogen Activator Inhibitor (PAI-1) Total Antigen. Oxford Biomedical Research (Oxford, MI, USA).

3.2.3   RNA Extraction and Analysis

The RNA was extracted from the QIAZOL lung homogenate using the QIAcube robotic workstation with the miRNeasy Mini Kit (QIAGEN, Netherlands). DNase I treatment was performed in column following manufacturer's instructions. RNA purity and concentration were determined by spectrophotometry (Nanodrop ND-2000/200C – Thermo Fisher Scientific, USA) and the RNA integrity was evaluated with the Agilent 2100 Bioanalyzer system.

- RNAsequencing (performed by an external laboratory – Centro Di Ricerca Interdipartimentale Per Le Biotecnologie Innovative (CRIBI) – University of Padua – Italy): libraries for massive parallel RNA sequencing (RNAseq) were prepared with the QuantSeq FWD (Lexogen) kit and sequenced with the use of an Illumina NextSeq500 platform, which generated at least 30 million reads/sample (75 pb SE). Reads quality analysis was performed with the FastQC tool. Transcripts were aligned on the *Rattus norvegicus* genome (v. 6) with the STAR tool and counts were determined with the HTSeq-count tool using the latest Ensembl annotation (v. 101).

- Quantitative Reverse Transcriptase-Polymerase Chain Reaction (qRT-PCR): the qRT-PCR achieved in this project were performed using custom-RT² Profiler PCR Arrays and the related technology

(QIAGEN, Netherlands). The RT² Profiler PCR Array System allows the gene expression analysis of different genes using the accuracy and efficacy of the Real-time PCR technology with a high grade of reproducibility and confidence of the data obtained. Each array could profile at the same time the expression of several genes for each single biological replicate. Based on this technology, RNA was reverse transcribed using RT^2 First Strand Kit (a tool for cDNA synthesis and genomic DNA elimination in RNA samples for use with RT^2 Profiler PCR Arrays) following manufacturer's instructions (starting material: 0.5 µg of total RNA). The reverse transcription reaction was made with Eppendorf Mastercycler ep Gradient, (Eppendorf, Germany). After this step, the cDNA was added to a RT² SYBR Green ROX qPCR Mastermix and the final solution was charged on a custom RT^2 PCR Array (array designed using a set of gene of interest, not disclosed in this thesis, see paragraph 4.3.6) and then analysed with Applied Biosystems™ 7500 Real-Time PCR Systems (ThermoFisher Scientific - Waltham, Massachusetts, USA) following the manufacturer's protocol. Due to possible critical issue connected to the use of SYBR technology, a melting curve analysis was performed at the end of each single RT^2 PCR array.

3.2.4 Histological Analysis

Masson's trichrome stained slides were scanned with NanoZoomer S60 (Hamamatsu Photonics K.K., Shizuoka, Japan) and assimilated into the Visiopharm Integrator System, a pathology image analysis software (VIS; version 2017.2.4.3387) for an automated quantification of lung fibrosis. The automated analysis was performed with an optimized and internally validated VIS Analysis Protocol Packages (APPs). The APP was designed to identify and then quantify the fibrotic tissue, detecting accumulation of connective tissue, excess of collagen deposition and cellular hyperproliferation[58]. The software was able to identify these types of morphological structures through the setting of colour, intensity, and size thresholds. The VIS application, before any quantification, was set on the control animals of each experiment to exclude the physiological collagenous tissue. Large bronchi,

vessels and emphysema were excluded from the lung area. A graphical readout of the VIS APP workflow is reported in **Figure 3.5**.
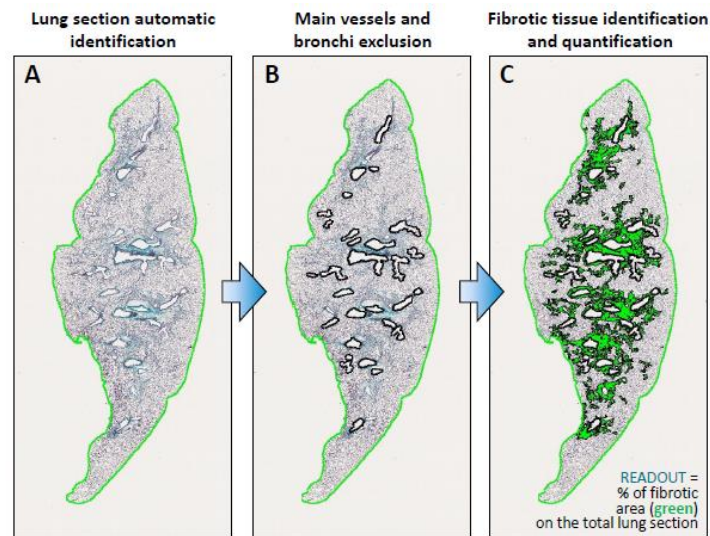
Figure 3.5 Graphical output of the workflow of the VIS App for quantification of lung fibrosis (image taken from a Chiesi abstract presented at the European Respiratory Society Congress 2019[58])

In addition, another histological analysis was performed by an expert histopathology to quantify and numerically evaluating the severity of lung fibrosis (analysis performed by external laboratories. For the Time Course Study Experiment the analysis was performed at HistoLab – Verona, Italy. The other two *in-vivo* experiments were analysed by the Laboratory Unit of prof. F. Quaini and C. Lagrasta, Department of Medicine and Surgery, University of Parma, Italy). The analysis was performed using a score evaluation method based on Ashcroft scale (grade 0 to 8), as described by Ashcroft et al. (1988)[59] and modified by Hübner et al. (2008)[60].

In this method, the lung sections were visualized by the observer using a x 10 magnification, and each observed field was individually assessed for severity of fibrosis through the assignation of a score between 0 and 8 following a specific scale of severity[59] (reported in **Table 3.1**). In each examined field, the predominant degree of fibrosis that occupied more than half of the field area, was recorded. If there were fields predominantly comprising of large bronchi/vessels or emphysema, they were not considered in the analysis[59,60]. The Ashcroft score for the whole lung section was obtained by averaging all the scores of all the analysed fields.

Table 3.1 *Description of the different Ashcroft Score, table taken from Hübner et all. (2008)*[60]

Grade of Fibrosis	Modified Scale
0	**Alveolar septa:** No fibrotic burden at the most flimsy small fibres in some alveolar walls **Lung structure:** Normal lung
1	**Alveolar septa:** Isolated gentle fibrotic changes (septum ≤3× thicker than normal) **Lung structure:** Alveoli partly enlarged and rarefied, but no fibrotic masses present
2	**Alveolar septa:** Clearly fibrotic changes (septum >3 × thicker than normal) with knot-like formation but not connected to each other **Lung structure:** Alveoli partly enlarged and rarefied, but no fibrotic masses
3	**Alveolar septa:** Contiguous fibrotic walls (septum >3 × thicker than normal) predominantly in whole microscopic field **Lung structure:** Alveoli partly enlarged and rarefied, but no fibrotic masses
4	**Alveolar septa:** Variable **Lung structure:** Single fibrotic masses (≤10% of microscopic field)
5	**Alveolar septa:** Variable **Lung structure:** Confluent fibrotic masses (>10% and ≤50% of microscopic field). Lung structure severely damaged but still preserved.
6	**Alveolar septa:** Variable, mostly not existent **Lung structure:** Large contiguous fibrotic masses (>50% of microscopic field). Lung architecture mostly not preserved
7	**Alveolar septa:** Non-existent **Lung structure:** Alveoli nearly obliterated with fibrous masses but still up to five air bubbles
8	**Alveolar septa:** Non-existent **Lung structure:** Microscopic field with complete obliteration with fibrotic masses

3.3 In-silico Activities

These activities were related only to the time course experiment and the curative protocol study with nintedanib.

3.3.1 General Bioinformatic Analysis

The Principal Component Analysis (PCA) is a multivariate statistical tool for reducing the number of variables of a big set of data, with the aim to increase the interpretability and minimize the loss of information[61]. It works generating a new lower set of uncorrelated variables (the principal components, PCs) that maximize variance[61]; in this way, the plotting of the first two/three PC in a cartesian graph can show a graphical representation of the variability of the experiment. The PCA showed in this work were performed with ClustVis[62] on the normalized read counts.

All the heatmap and the similarity matrix performed in this work were realized using Morpheus, a matrix visualization and analysis software (https://software.broadinstitute.org/morpheus).

The Venn Diagrams were performed using Venny, a web tool for comparing lists (Oliveros, J.C. (2007-2015) https://bioinfogp.cnb.csic.es/tools/venny/index.html).

The Graphical Network presented in this study was created using GeneMANIA[63] and was subsequently edited with Cytoscape[64].

3.3.2 Gene Expression Analysis

Differentially Expressed Genes (DEGs) between BLM or NINT and SAL samples were identified for each experiment with the Limma-voom tool. Genes were deemed as differentially expressed if the $\log_2$ fold-change (FC) was ≥ 1 or ≤ -1 and the adjusted p-value ≤ 0.05.

The pathway enrichment analysis performed on DEGs was realized using the Metascape analysis resource available online[65]. Only pathways with a Log false discovery rate (FDR) < -4 were considered as significantly enriched.

3.3.3 WeiGhted Correlation Network Analysis (WGCNA)

WGCNA is a technique of the system biology able to define the correlation profile among genes across transcriptomic data. The WGCNA identifies clusters (modules) of highly correlated genes using eigengene network methodology and it relates them one to another and to external traits, (provided by the user)[66]. In the WGCNA, the network could be signed (modules correspond to positively correlated genes) or unsigned (modules correspond to clusters of genes with high absolute correlations)[66]. In these experiments, all the performed WGCNA were based on unsigned network, so in this case, after the identification of the modules which presented a specific eigengene expression profile, it was assigned a module membership (MM) value to each gene of each module and this value was from 1 to -1 (respectively to express gene extremely correlated or anti correlated to a specific module profile). The MM values were flanked by a statistical significance (Log p-val).

- <u>In the time course study</u>, modules of co-expressed genes between the different groups of treatment (Naïve, SAL and BLM) during all the analysed time points were identified using the WGCNA package in R[66]. Only genes that have at least 10 counts in 22 samples out of 28 were kept for module construction (13.500 genes). Modules were identified using the blockwise-modules function (WGCNA package) set at default parameters, except for soft thresholding power = 8, minimum module size = 30 and mergeCutHeight = 0.25. The statistical significance of the correlation between gene expression module profiles and phenotypic traits (Ashcroft score, and % of Fibrosis) was evaluated using Pearson correlation.

- <u>In the curative experiment with nintedanib</u>, modules of co-expressed genes between the different groups of treatment (SAL, BLM and NINT) were identified using the WGCNA package in R[66]. Only genes that have at least 10 counts in all the samples, and 50 counts in 8 samples out of 12 were kept for module construction (11.306 genes). Modules were identified using the blockwise-modules function (WGCNA package) set at default parameters, except for soft thresholding power (bicor) =

4, minimum module size = 30 and mergeCutHeight = 0.25. The significance of the correlation between gene expression module profiles and phenotypic traits (Ashcroft score, and % of Fibrosis) was evaluated using Pearson correlation.

For both the experiments the pathways enrichment analysis was performed on module gene lists using Metascape analysis resource available online[65]. Only pathways with a Log FDR < -4 were considered as significantly enriched.

3.3.4   Gene Set Enrichment Analysis (GSEA)

The GSEA can identify if, within a given gene set (called S), there are elements that are disposed toward the top or bottom of a ranked list of genes (called L)[67]. So, this analysis can tell us if a set of genes (for example genes significantly de-regulated in a specific human IPF study) are randomly distributed through our list of pre-ranked genes (for example list of DEG ranked based on the $\log_2$ FC values) or they are primarily found at the top or bottom. For each S-L relation, the analysis produces an enrichment score (ES) and a normalized enrichment score (NES, enrichment score normalized for each gene set taking in to account the size of the set) and a value of statistical significance adjusted for multiple hypothesis (FDR).

To define which subset of genes, have the highest influence in a specific GSEA analysis, the GSEA software provides a tool called leading edge analysis. Starting from the GSEA results, the leading edge analysis allows to identify who are the genes that drive the enrichment score of the GSEA[68].

In this work, the GSEA and the leading edge analysis were used to compare the transcription profiles produced by time course experiment with other published transcriptional signatures obtained in other rodent models[41,52] and in human IPF[69–77]. To this aim, gene lists of significant up- or down-regulated genes were created from these published studies using data provided directly by the authors in the supplemental material section or using the GEO2R, a tool available on the Gene Expression Omnibus (GEO) Website to obtain gene expression data comparing two or more groups

of samples from a specific dataset deposited in GEO. List of pre-ranked genes according to $\log_2$ FC or to MM values were generated by our data and used as input. Human orthologs of rat genes were identified with the BioMart tool in the Ensembl database (http://www.ensembl.org/biomart/martview).

GSEA was also used to compare the two WGCNA performed in this study. In this analysis, we used pre-ranked gene list derived from the most informative modules of the WGCNA performed in the curative experiment with nintedanib (see **Figure 4.30** for more details) and as a gene sets, we used genes derived from the most informative WGCNA modules of the time course experiment (see **Figure 4.11** for more details). The ranking was performed based on the MM value. In this case for each considered module we created two lists, one composed of correlated genes (gene MM ≥ 0.8) and one composed of anti-correlated genes (gene MM ≤ - 0.8).

4. RESULTS

4.1 Time Course Study

The first experiment performed during my PhD period, with the aim to acquire a deeper and comprehensive view of the rat model of BLM-induced lung fibrosis, was a time course study that allowed to evaluate the evolution of lung fibrosis induced by BLM over-time.

4.1.1 Body Weight Trend and Survival

The BLM administration induced a significant weight loss in the first days after treatment, with a peak of minimum body weight value around the seventh day, where animals treated with BLM lost on average ≃16% of their starting weight. In the following days, the BLM-treated animals recovered weight with a regular and progressive trend until the end of the experiment. The difference between the mean values of the weight of the animal treated with SAL and BLM lost the statistical significance after the 42nd day (**Figure 4.1 A)**. Moreover, after the 32nd day the slope of the two curves was comparable, indeed, the percentage of increase of the BLM group compared to the control group (SAL) remained almost the same from that day until the end of the experiment (**Figure 4.1 B**). These observations suggest that the effect of BLM on the weight of the animals was lost after 1 month from the first administration.
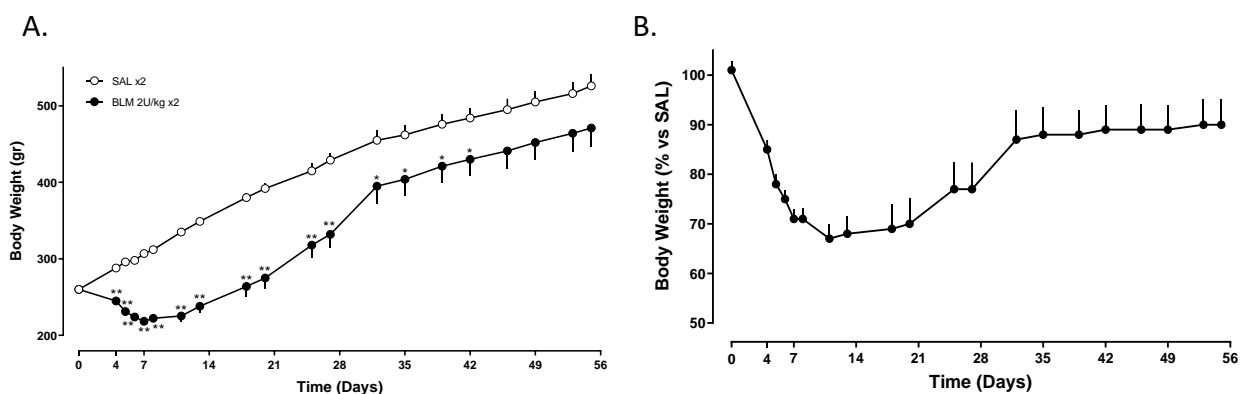
Figure 4.1 Body weight trend. *A.* The body weight was expressed as raw value (mean ± SEM) for both groups of animals. *p≤0.05, ** p≤0.01 vs SAL, statistical analysis performed by Student's t test (with Welch correction when variances are statistically different) or Mann-Whitney test. *B.* Body weight expressed as percentage of increase/decrease of the BLM group respect to the control group.

During the experiment, a 15% of mortality was observed in the group of animals treated with BLM until day 16, as showed in the survival graph in **Figure 4.2**.
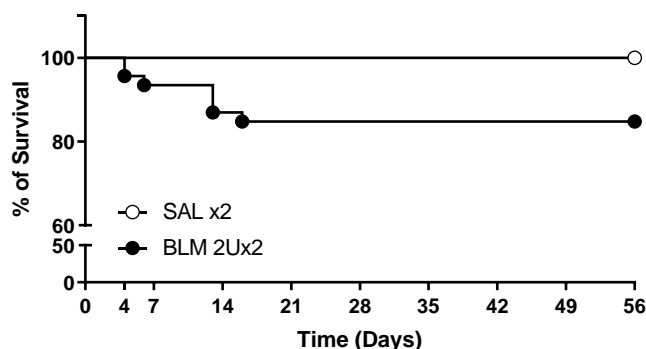
Figure 4.2 Survival. Each point represents a death and contributes to lowering the line of survival

4.1.2 Blood Analysis

The white blood cells (WBC) count, performed by the automated cell counting system (DASIT) in the blood, showed an increase of systemic inflammatory cells at day 7 and 14 in BLM treated rats respect to the SAL group (**Table 4.1**). Indeed, at day 7 despite a similar amount of the total WBC, the number of monocytes, neutrophils and eosinophils was doubled in BLM animals compared to their controls; moreover, at this time point in the BLM group the highest value of monocytes and neutrophils, compared to the following time points, was recorded. Except for the first time point, there are no significant differences between BLM and SAL in the number of monocytes. Neutrophilia and eosinophilia appeared increased in the BLM group at day 14, 21 and 28 as well, and in some cases the differences with SAL groups were statistically significant. Otherwise, the number of lymphocytes was reduced (not significantly) in the BLM group compared to control animals at all the analyzed time points. This information is better highlighted in **Figure 4.3** where each cellular population is represented as a percentage of the total WBC.

Table 4.1 *Number of total and differential WBC counts in SAL and BLM groups at each time-point expressed as mean value.*

Time Point	Group	Total WBC mean (10^6/ml)	Monocytes mean (10^6/ml)	Neutrophils mean (10^6/ml)	Lymphocytes mean (10^6/ml)	Eosinophils mean (10^6/ml)
T7	SAL	4.95	0.16	0.43	4.29	0.07
	BLM	4.41	**0.31***	**0.82***	3.12	0.15
T14	SAL	6.06	0.22	0.50	5.28	0.05
	BLM	7.56	0.28	**0.73***	6.20	**0.33**
T21	SAL	6.15	0.21	0.51	5.31	0.08
	BLM	4.48	0.18	0.62	3.57	0.11
T28	SAL	6.88	0.21	0.45	6.14	0.08
	BLM	6.91	0.26	**0.69****	5.78	**0.17**
T56	SAL	7.52	0.24	0.74	6.44	0.10
	BLM	5.26	0.17	0.51	4.48	0.09

*$*p \leq 0.05$, ** $p \leq 0.01$ vs SAL, statistical analysis performed by Student's t test (with Welch correction when variances are statistically different) or Mann-Whitney test.*
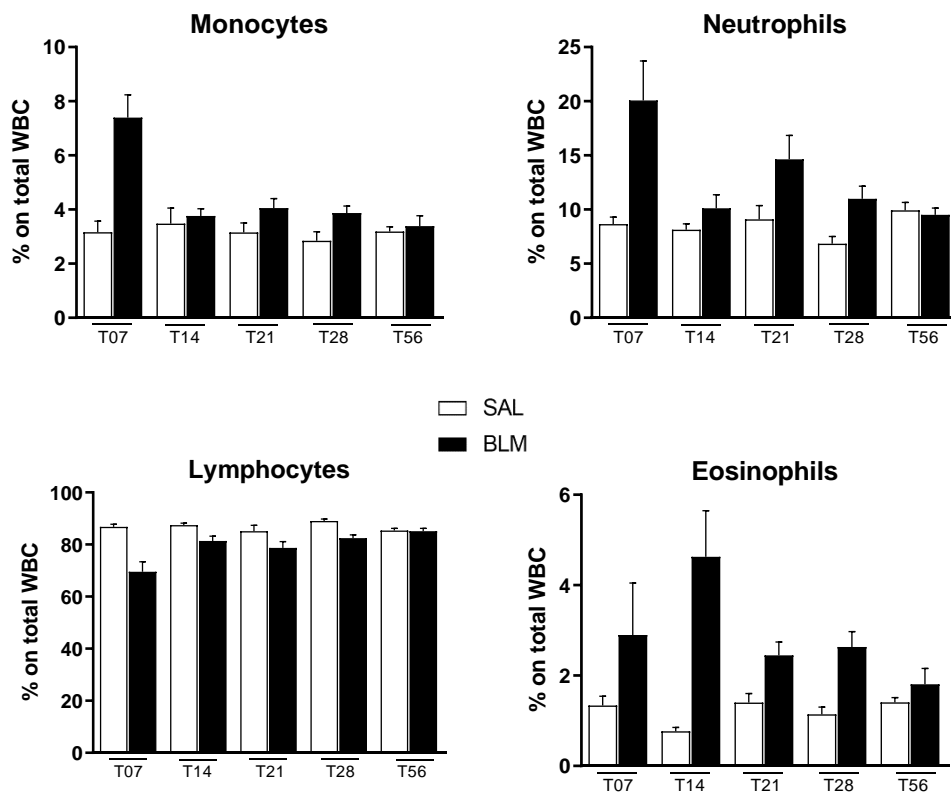
Figure 4.3 *WBC differential cells counts expressed as percentage (mean value ±SEM) of total WBC. See **Table 4.1** for statistical analysis*

4.2   Morphological and Molecular Characteristics of Lung Fibrosis Induced by BLM Over Time

In order to evaluate the morphological development of lung fibrosis during the time course and to understand the onset of specific pathological features induced by BLM, a series of analysis were conducted on histological images of rat left lungs. Moreover, an estimation of collagen content was conducted on right lung homogenates through the evaluation of hydroxyproline (HYP) content.

4.2.1   Histological Analysis

Two semi-quantitative analysis were performed for the quantification of lung fibrosis on Masson's trichrome stained lung slices in addition to a general qualitative histological evaluation of the lungs. Moreover, a pathologist performed a semi-quantitative analysis for the evaluation of different types of damage induced by BLM during the time. More technical details are described in the Materials and Methods section.

The **Figure 4.4** shows one representative image of BLM-treated lungs for each analysed time point, flanked by an image from one of the untreated animals as reference of the starting condition at T0. The staining revealed that BLM induced an acute and severe inflammatory reaction in the lung at day 7, with haemorrhage and alveolar infiltration of different inflammatory cells, like neutrophils and lymphocytes. Moreover, at this time point, there was an initial diffused collagen deposition, especially around large blood vessels and bronchi. At day 14, the tissue appeared less inflamed and damaged compared to the previous time point; this seemed to be related to the reduction of haemorrhage and inflammatory cells infiltration whereas the collagen deposition remained diffused through the tissue with the presence of thickened but still clearly visible alveoli. It was also observed the appearance of early emphysematous changes. At day 21, in most samples, fibrotic tissue started branching and large areas of lung parenchyma were replaced with dense collagen deposition in which alveoli were not clearly identifiable. Moreover, emphysematous lesions appeared larger and

extended in some samples displaying this type of lung remodelling. Tissue macrophages, that were absent or rare in the first two weeks post-bleomycin, were identified at T21 at the edges of fibrotic areas or distributed in the fibrotic tissue. At day 28, was observed a reduction of severity and dimension of total fibrosis, although collagen fibres appeared to be organised in less extended but more compact fibrotic areas. Moreover, compared to T21, macrophages appeared to increase in number. Finally, 56 days after the first BLM administration a more prominent reduction of collagen accumulation was observed, and the remaining fibrotic areas appeared thicker and denser than at the other time points (scar-like tissue). Moreover, a severe macrophage infiltration in proximity of large blood vessels and in fibrotic areas was observed.
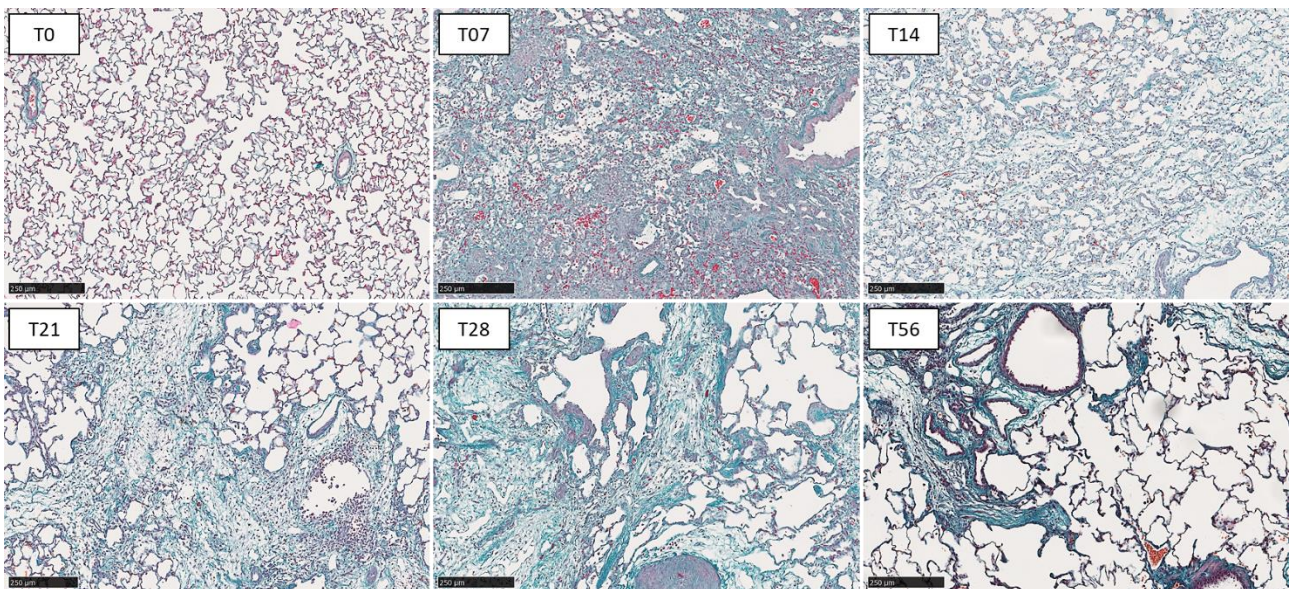
Figure 4.4 *Overtime histological appearance of the lung fibrosis induced by BLM. Representative Masson's Trichrome-stained lung tissue sections obtained at the starting time point of the protocol (untreated animals, T0) and 7, 14, 21, 28 and 56 days after the first BLM instillation (scale bar = 250 μm).*

All these qualitative observations were confirmed and supported by the two semi-quantitative analysis for the evaluation of lung fibrosis. The automated analysis performed using the Visiopharm software (**Figure 4.5 A**) reported that the area of fibrotic tissue observed at day 7 was about 55% of the total lung area. This area remained unchanged up to day 21 (≈50%) and gradually decreased at

day 28 and 56 (although remaining significantly higher than the control group, which had an average value of 5.8% for all the time points analysed, data not shown).

These results were confirmed by the Ashcroft score evaluation (**Figure 4.5 B**), which showed a frequency of distribution of the scores ≥2 (a damage more severe than an "isolated alveolar septa with gentle fibrotic changes" as defined by Hübner et al.[60]) around 50% up to 21 days after the first BLM injection. This percentage decreased in the last two time points reaching the 21% of fibrotic lung area at T56. The Ashcroft score evaluation also confirmed a decreased severity at day 14. Indeed, at this time point there were no fields with severe scores (≥6). Day 14, showing a reduced inflammatory response and first appearance of fibrotic lesions, may represent the switch point between the inflammation and the fibrotic phase of the model. The absence of score ≥6 was also reported at day 56, probably highlighting an initial attempt to fibrosis resolution and restoration of a physiological condition of the tissue.
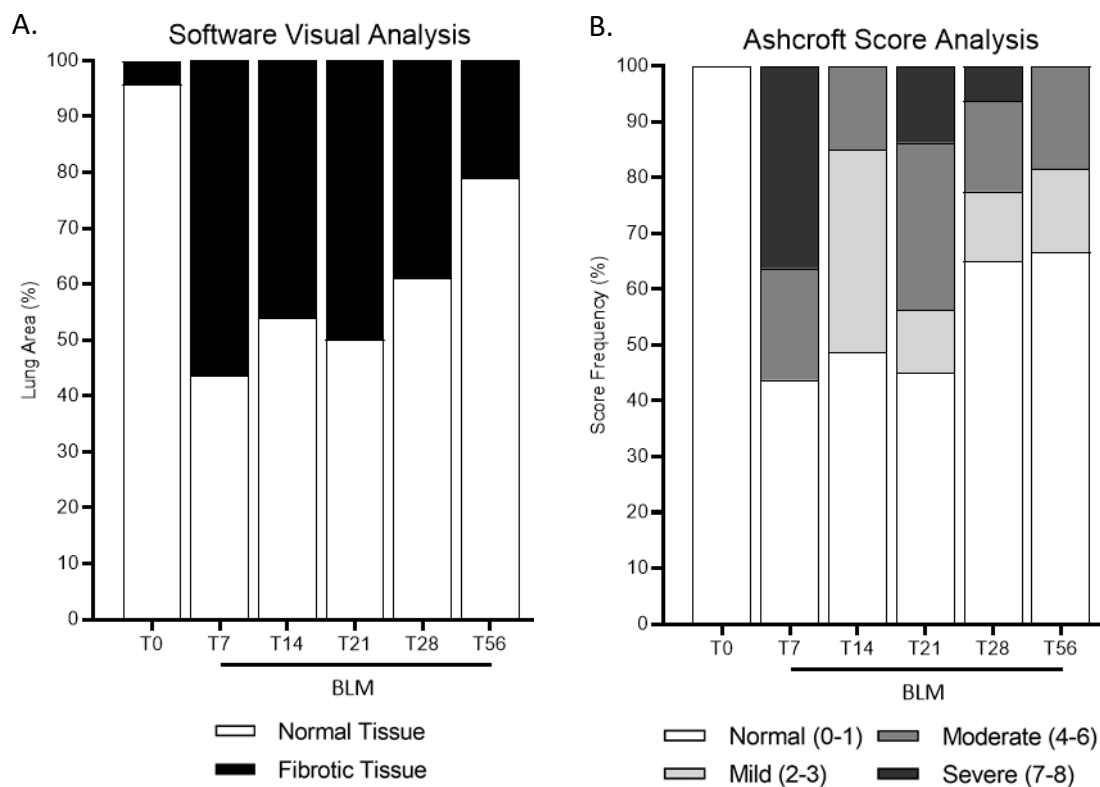
*Figure 4.5 Quantification of pulmonary fibrosis using the Software Visual Analysis (**A**) and the Ashcroft Score method (**B**) in BLM-treated animals and in naïve animals, which are used as a control of the starting point condition. Data are expressed as mean value.*

To better understand the evolution of the damage induced by BLM over time and to try to estimate the macroscopic variations occurring in the model, a pathologist evaluated a series of pathological conditions: alveolar haemorrhage; arterial medial hypertrophy; pleural fibrous adhesion; alveolar epithelialization (an example of these type of damage was reported in **Figure 4.6**); and assigned a grade of severity for each condition to each single rat lung slide classified as: 0 (absent); 1 (minimal); 2 (moderate); 3 (severe).
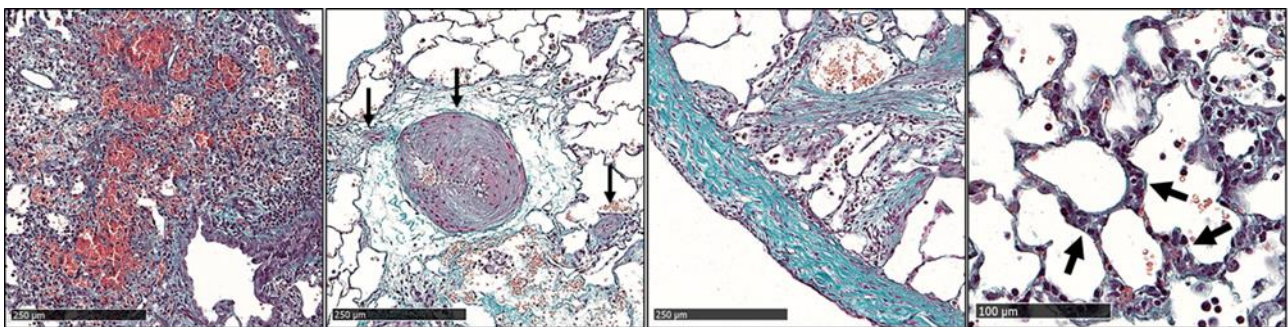
Figure 4.6 Representative Masson's trichrome stained lung sections. Photomicrographs of different types of damage: alveolar haemorrhage, arterial medial hypertrophy, pleural fibrous adhesion and alveolar epithelialization, from left to right. The black arrows highlight the area of interest with greater precision (scale bar = 250 µm for the first three images and scale bar = 100 µm for the last image).

After the evaluation, pie graphs were generated showing the frequency of distribution of the various scores attributed to each type of damage over time (all the graphs were reported in **Figure 4.7**). The graphs showed that the damages more related to an active wound healing process (alveolar haemorrhage, arterial medial hypertrophy and alveolar epithelialization) were more severe and distributed in the first time points, with a tendency to decrease over time and completely disappear at 56 days. Instead, the pleural fibrous adhesion was evident only in the three central time points of the time course.
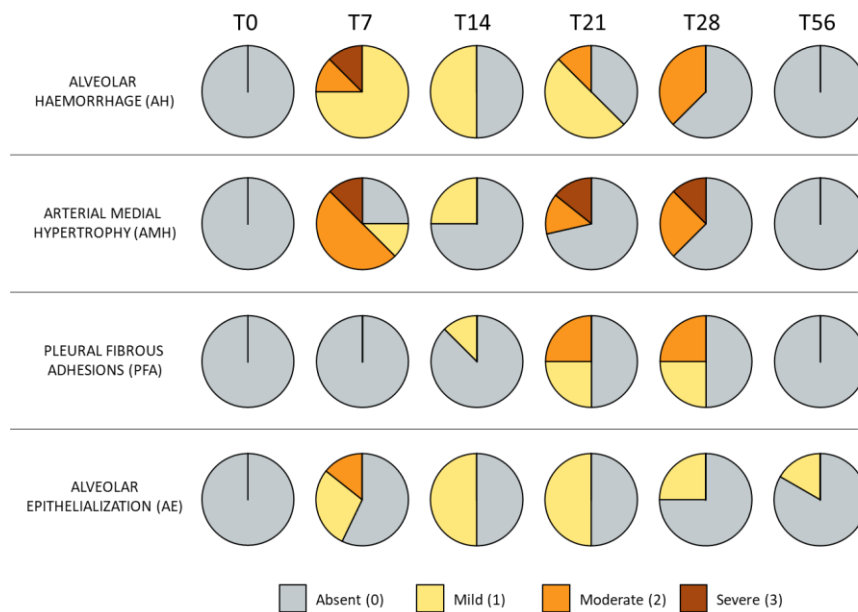
Figure 4.7 *Frequency distribution of the different types of damages induced by BLM.*

4.2.2 Estimated Quantification of Lung Collagen Content

Considering the high content of the HYP within the triple helix of collagen, its quantification was used to obtain an approximation of the amount of collagen in the lungs.

The HYP content was assessed in the right lung homogenate of animals not destined to the transcriptomic analysis in all the analysed time points. The level of the lung HYP measured in BLM and SAL groups increased over time compared to the untreated animals at T0 (**Figure 4.8**), probably due to the natural growth and aging of rats. However, a significant difference between the two groups of treatment was observed among the different time points, especially in the central ones where the hydroxyproline content significantly doubles in BLM group compared to SAL group. The fold of increase between SAL and BLM at day 56 was less than 2 and not statistically significant, suggesting a preliminary reduction of the collagen content of fibrotic lesions.
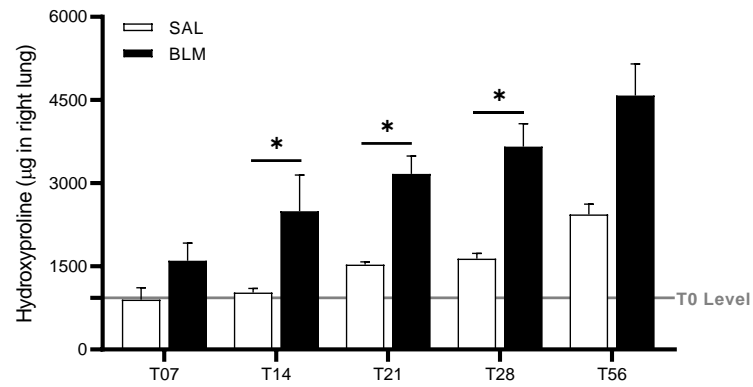
Figure 4.8 *Evaluation of HYP content in total right lung homogenate. Quantification of HYP level in lung tissue obtained at each time point for SAL and BLM group. Data are expressed as mean ±SEM (n=4 per group for each time point, except for BLM T56 were n=2). *p<0.05 vs SAL. Statistical analysis performed by Mann-Whitney test. The grey line represents the T0 Level (untreated condition).*

4.3   Whole Time Dependent Transcriptomic Analysis

The histopathological characterization described in the previous paragraph demonstrated that the BLM treatment resulted in the development of pulmonary fibrosis. The characterization of this model followed with a rat lung transcriptome analysis to understand the involvement of these molecular changes in the initial progression and the following regression of the fibrotic response. Finally, we integrated the transcriptomic analysis with the lung histological observations.

4.3.1   General Data

Transcriptome profiling was performed with at least two biological replicates for each time-point including the T0 untreated control condition (see Materials and Methods for more details). RNAseq analysis revealed a total of 25140 expressed genes: 22050 protein-coding and 3090 lincRNA genes. Principal Component Analysis (PCA) conducted on whole transcriptome dataset (**Figure 4.9**) revealed coherent transcription profiles for the biological replicates, with a clear separation between SAL group animals, which clustered close to the untreated animals (naïve) in the lower part of the PCA diagram, and BLM-treated animals on the mid-upper part of the diagram. The x-axis referred to time-dependent variability, and the observed distribution (from T07 to T56, left to right) was consistent with increasing time interval after SAL administration and progressive ageing and weight gain of the animals, with the exception of the T0 samples, which were both positioned in the mid-region of the SAL group data-points. Interestingly, the T07 SAL points were the most distant from untreated condition, indicating that the mere stress associated to intratracheal administration somehow contributed to transcription profile variability. As it might have been expected, the time dependent PCA distribution was more evident for the BLM than for the control SAL group.
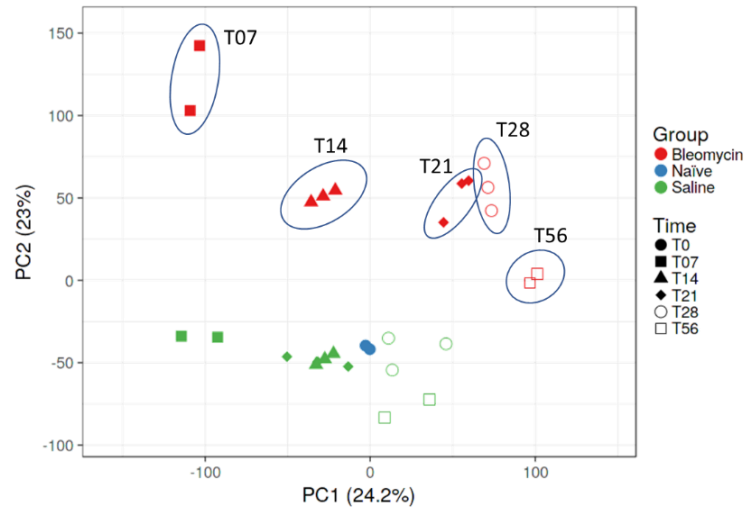
Figure 4.9 *Graphical representation of the PCA.*

4.3.2   Differential Expressed Genes Analysis

The number of Differentially Expressed Genes (DEGs) identified at each time-point ranged from 2221 (T07) to 1217 (T14), with a total of 4672 DEGs distributed across all the examined time-points (**Figure 4.10 A**). The number of up-regulated genes exceeded the number of down-regulated genes at T7 and T14, whereas the opposite trend was observed at later time-points. As shown in the heatmap in **Figure 4.10 B**, DEGs followed a time-dependent pattern and exhibited a rather specific expression signature, with very few instances of genes that changed the sign of their expression deregulation over the time-course of this study. Furthermore, hierarchical clustering of genes whose expression levels changed significantly across the different time-points highlighted the existence of three seemingly distinct response to BLM treatment, which can be described as an "early response", a "late response", and a "long-lasting response" (these three terms were a personal literary interpretation of what was observed in the heatmap). Based on these findings, and in agreement with the results of the histological analyses, T14 seemed to represent a transition time-point from an early inflammatory to a late, predominantly fibrotic phase.
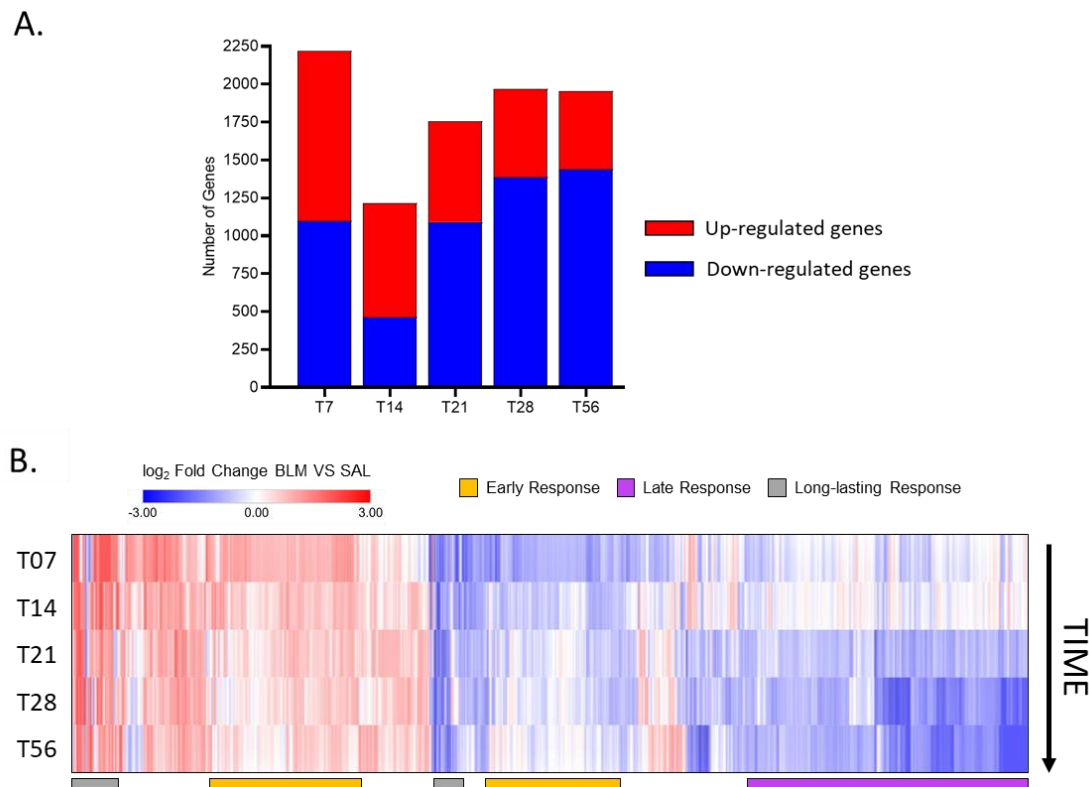
Figure 4.10 A. *Scale bar graphs representing the number of Up- and Down-regulated genes (BLM vs SAL) for each time point.* **B.** *Heatmap of all the genes that registered a statistically significant de-regulation in at least one time point. Each column represents a gene; up-regulated genes are in red; down-regulated genes are in blue. Hierarchical clustering for the columns was performed using a Euclidean distance metric.*

4.3.3   Pathway Analysis on Differentially Expressed Genes

The functional analysis conducted on differentially expressed genes revealed several pathways involved in the response to the BLM treatment during all the time course.

The Metascape online resource[65] identified multiple signalling pathways and several biological process enriched in differentially expressed genes, such as the cell cycle regulation and extracellular matrix organization process. A complete list of the Top 5 enriched pathways divided in UP and DOWN regulated is listed in **Table 4.2**. A pathway was considered statistically enriched in a list if its Log false discovery rate (FDR) was lower or equal to -4. Some of these pathways appeared to be significantly enriched throughout the entire time-course, especially in the up-regulated lists; to mention an example, the up-regulated gene lists "hallmark epithelial mesenchymal transition" and "extracellular matrix organization", both with the highest significance at time point 28. Other

pathways, instead, were significantly enriched only at specific post-BLM treatment time points; for example, "regulation of blood circulation", significantly enriched in genes down-regulated specifically at T07 and T14.

Table 4.2 *Pathways significantly enriched in DEGs lists at different post-BLM treatment time points.*

Top5 list	GO	DESCRIPTION	DN_T07	DN_T14	DN_T21	DN_T28	DN_T56	UP_T07	UP_T14	UP_T21	UP_T28	UP_T56	MAX
DOWN-REGULATED T07	GO:0003013	circulatory system process	-12	-7.6	-6.1	-3.9	-3.1	-3.8	-4.8	-6.8	-5.8	-3.2	-12
	GO:0005509	calcium ion binding	-8.7	-4.3	-2.8	-3	-1.8	-4.5	-4.8	-3.4	-6.9	-4.7	-8.7
	GO:0050878	regulation of body fluid levels	-7.7	-5.3	-4.5	-1.7		-3.9	-3.4	-2.5		-2.6	-7.7
	GO:1903522	regulation of blood circulation	-7.3	-4	-3.8	-3	-2.6			-2.2	-2.3	-2	-7.3
	GO:0043269	regulation of ion transport	-7.3	-4	-4.6	-1.7		-2.9	-3.3	-6.5	-3.9	-2.2	-7.3
DOWN-REGULATED T14	R-HSA-211945	Phase I - Functionalization of compounds	-5.3	-8.9									-8.9
	GO:0008015	blood circulation	-12	-7.8	-6.3	-4.1	-3.3	-3.6	-4.9	-6.6	-5.9	-3	-12
	GO:0009410	response to xenobiotic stimulus	-4.9	-6.5	-2.5	-2.2							-6.5
	GO:0006805	xenobiotic metabolic process	-4.5	-6.3									-6.3
	GO:0003018	vascular process in circulatory system	-3.8	-5.5	-4.1	-1.7	-1.9	-1.8	-3	-2.9			-5.5
DOWN-REGULATED T21	GO:0003779	actin binding	-5.1	-2.6	-12	-7.7	-8.5	-1.8					-12
	GO:0030029	actin filament-based process	-6	-2.7	-7.2	-7.7	-9.9	-2.5					-9.9
	R-HSA-109582	Hemostasis	-3.3	-3.6	-7	-5.6	-4	-12	-6.8	-3.3	-4.1	-2.4	-12
	GO:0030036	actin cytoskeleton organization	-4.2	-2.2	-6.4	-7.4	-11	-2					-11
	GO:0016773	phosphotransferase activity, alcohol group as acceptor		-2.1	-6.4	-12	-8.8						-12
DOWN-REGULATED T28	GO:0016773	phosphotransferase activity, alcohol group as acceptor		-2.1	-6.4	-12	-8.8						-12
	GO:0051345	positive regulation of hydrolase activity	-3.6	-2.8	-5.6	-8.2	-6.6	-3.1	-2.4	-3.3			-8.2
	GO:0004674	protein serine/threonine kinase activity			-5.3	-8.1	-7.6						-8.1
	GO:0097435	supramolecular fiber organization	-4.4		-6	-7.9	-12	-6.1	-3.3	-3.4	-3.6	-2.2	-12
	GO:0003779	actin binding	-5.1	-2.6	-12	-7.7	-8.5	-1.8					-12
DOWN-REGULATED T56	GO:0097435	supramolecular fiber organization	-4.4		-6	-7.9	-12	-6.1	-3.3	-3.4	-3.6	-2.2	-12
	GO:0016773	phosphotransferase activity, alcohol group as acceptor		-2.1	-6.4	-12	-8.8						-12
	GO:0019904	protein domain specific binding	-1.7		-3.7	-5.1	-8.8						-8.8
	GO:0016301	kinase activity		-1.8	-6.3	-11	-8.6						-11
	GO:0003779	actin binding	-5.1	-2.6	-12	-7.7	-8.5	-1.8					-12
UP-REGULATED T07	M5901	HALLMARK G2M CHECKPOINT				-2.1	-3.8	-30	-18	-5.8	-3.2		-30
	R-HSA-1640170	Cell Cycle					-2	-28	-12	-5.3			-28
	GO:0007059	chromosome segregation					-2.8	-27	-15	-5.2			-27
	M5925	HALLMARK E2F TARGETS						-27	-14	-11	-1.7		-27
	M5930	HALLMARK EPITHELIAL MESENCHYMAL TRANSITION						-26	-27	-25	-32	-12	-32
UP-REGULATED T14	M5930	HALLMARK EPITHELIAL MESENCHYMAL TRANSITION						-26	-27	-25	-32	-12	-32
	M5885	NABA MATRISOME ASSOCIATED	-3.2	-2.4				-20	-25	-15	-20	-10	-25
	M5901	HALLMARK G2M CHECKPOINT				-2.1	-3.8	-30	-18	-5.8	-3.2		-30
	GO:0051301	cell division			-2.9	-3.3	-5.1	-25	-18	-5.5	-2.7		-25
	GO:0030198	extracellular matrix organization	-1.7	-2.1			-2	-19	-18	-21	-27	-10	-27
UP-REGULATED T21	M5930	HALLMARK EPITHELIAL MESENCHYMAL TRANSITION						-26	-27	-25	-32	-12	-32
	GO:0030198	extracellular matrix organization	-1.7	-2.1			-2	-19	-18	-21	-27	-10	-27
	M5885	NABA MATRISOME ASSOCIATED	-3.2	-2.4				-20	-25	-15	-20	-10	-25
	R-HSA-1474244	Extracellular matrix organization		-2				-16	-16	-14	-20	-8.1	-20
	M5884	NABA CORE MATRISOME	-1.9	-1.9				-8.9	-13	-14	-21	-6.8	-21
UP-REGULATED T28	M5930	HALLMARK EPITHELIAL MESENCHYMAL TRANSITION						-26	-27	-25	-32	-12	-32
	GO:0030198	extracellular matrix organization	-1.7	-2.1			-2	-19	-18	-21	-27	-10	-27
	M5884	NABA CORE MATRISOME	-1.9	-1.9				-8.9	-13	-14	-21	-6.8	-21
	M5885	NABA MATRISOME ASSOCIATED	-3.2	-2.4				-20	-25	-15	-20	-10	-25
	R-HSA-1474244	Extracellular matrix organization		-2				-16	-16	-14	-20	-8.1	-20
UP-REGULATED T56	M5930	HALLMARK EPITHELIAL MESENCHYMAL TRANSITION						-26	-27	-25	-32	-12	-32
	hsa04610	Complement and coagulation cascades		-2.2				-8.8	-12	-9.5	-8.3	-11	-12
	GO:0030198	extracellular matrix organization	-1.7	-2.1			-2	-19	-18	-21	-27	-10	-27
	M5885	NABA MATRISOME ASSOCIATED	-3.2	-2.4				-20	-25	-15	-20	-10	-25
	GO:0002526	acute inflammatory response						-6.3	-9.4	-10	-9.9	-9.8	-10

Table reports the top 5 enriched pathways in terms of Log FDR for each single gene list. Each row represents a pathway/biological process, and its code, name, and significance (Log FDR) in each reported list. Green scale highlights increasing significance (Log FDR) (from light to dark), white colour highlights Log FDR values higher than the statistically significance cut-off (-4) and grey colour highlights non-calculable Log FDR values.

4.3.4 Time Dependent Transcription Profiles Analysis

A network-based approach (WeiGhted Correlation Network Analysis, WGCNA) was used to identify specific time-dependent transcriptional profiles and to integrate the results of DEGs analysis. Unsigned WGCNA revealed 16 modules of co-regulated (or anti-regulated) genes. The first five identified modules accounted for 63.9% of all the analysed genes, while the remaining 11 modules contained less than 5% genes each. A pathway enrichment analysis, performed with Metascape[65], was applied to the WGCNA modules in order to identify specific processes and pathways associated to the different, time-resolved responses to BLM. The expression profiles of Module Eigengenes (MEs) of the most informative module are reported in **Figure 4.11**, and **Table 4.3** shows the Top 5 enriched pathways of each of these modules. We consider these modules the most informative because modules 1 to 5 contain more than 63% of all the genes used for WGCNA, and module 8 for its strong correlation to both histological parameters (see below). For a complete view of all the modules identified in this experiment see **Figure 4.12**. As revealed by the WGCNA, and in agreement with the results of the PCA, only a minimal variation was highlighted by the SAL vs. naïve/T0 comparison. A much higher and consistent intra-group variation was, instead, revealed by BLM vs. naïve/T0 and BLM vs. SAL comparisons, which highlighted a predominant up-regulation for modules 2, 8 and 5, and an opposite trend for all the remaining modules.

This analysis also allowed to correlate specific groups of coherently expressed genes with phenotypic traits associated to each time-point of the BLM treatment, like the histopathological parameters. Therefore, for each module the correlation (Pearson) with the corresponding values of Ashcroft Score and % of fibrotic tissue measured on lung sections of the same animals was calculated. As shown in **Figure 4.11**, two modules (3 and 8) significantly correlated with the Ashcroft Score and the % of Fibrosis.

Modules 8, 4 and 1 were truly representative of the three main types of responses previously defined by DEGs analysis ("long-lasting", "early" and "late" responses respectively; see also **Figure 4.10 B**). No appreciable gene expression variation was apparent for the SAL samples in module 8, while a marked and persistent up-regulation, starting from the earliest (T07) time-point, was observed for the same module in the BLM-treated samples. Module 8 was enriched in multiple extracellular matrix-related pathways and positively correlated with lung fibrosis histological parameters (Pearson correlation p-val = $3.9*10^{-13}$ and p-val = $2.1*10^{-12}$ for the Ashcroft Score and % Fibrosis, respectively). The module 4, characterized by a strong down-regulation at early time-points, was enriched in pathways related to circulatory system probably reflecting the initial severe damage induced by BLM, characterized by haemorrhage and inflammatory alveolar infiltration as revealed by histological analysis. Module 1, which contained more than 2500 genes, was largely unaffected by BLM treatment at T07 and T14 but was characterized by a marked down-regulation (involving 84% of the genes of the module), in the last three time-points. Based on this quite peculiar expression profile, and the functional heterogeneity of the genes/pathways enriched in module 1 (ranging from kinase activity regulation, to cell division/projection and chromatin modification), it was reasonable to hypothesize that this module was not directly de-regulated in response to BLM treatment, but rather it resulted from an indirect effect associated to genes and pathways that were strongly dysregulated in the first, acute damage phase of the BLM response. Flanking these three main modules, which display distinct expression profiles, there were also other three modules (2, 3 and 5) that had a profile referable to the previous three but with some slight variations. ME2 was characterized by an expression pattern very close to the ME8, with a clear trend toward up-regulation at all the analysed time-points. The module 2 was enriched in cell cycle, cytoskeleton regulation and microtubules related pathways. Also, ME5 had an expression pattern similar to the ME8, but in this case the variation at T07 an T28 were not so marked as for other time points, which

reflected an increase in expression of the corresponding SAL conditions respect to T0, and it did not have a strong significance values of enrichment with the exception for Asparagine N-linked glycosylation pathway. The ME3, instead, was characterized by a marked and persistent down-regulation, which became more prominent in the latest time-points, thus this type of response was placed between late and long-lasting. Similarly to the module 8, the number 3, was enriched in processes related to the leucocyte system, cell adhesion and cellular trafficking, and was significantly anti-correlated with the histological parameters (Pearson correlation p-val = $5.0*10^{-12}$ and p-val $=1.2*10^{-7}$ for the Ashcroft Score and % Fibrosis respectively).
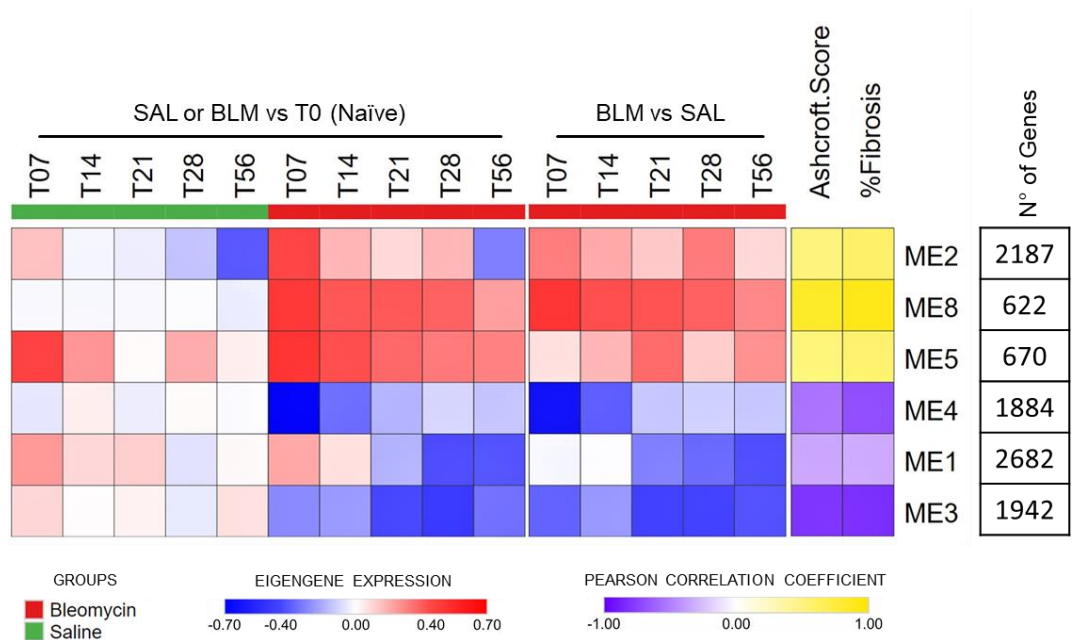
Figure 4.11 *Heatmap of the most informative modules (represented by their Module Eigengene, MEs). Each square represents the eigengene expression of a single biological condition (column) in a specific ME (rows). In the left part of the heatmap in column the biological condition is represented by the comparison of SAL and BLM at each time point vs T0 condition, while in the right part the biological condition refers to a direct comparison between SAL and BLM, as reported above the column label. The values are calculated averaging the values of eigengene expression of each biological replicate and relating them to the control group of interest (T0 or respective SAL). The two last right columns report the Pearson correlation value between each ME and the two histological parameters.*

Table 4.3 *Pathways enriched in gene lists derived from the most relevant modules.*

Top5 list	GO	DESCRIPTION	ME11	ME13	ME2	ME8	ME14	ME5	ME6	ME12	ME15	ME4	ME7	ME9	ME10	ME16	ME1	ME3	MAX
ME2	GO:0051301	cell division			-19												-8.6		-19
ME2	R-HSA-1640170	Cell Cycle			-16				-3.8								-6		-17
ME2	M5901	HALLMARK G2M CHECKPOINT			-16												-3.9		-18
ME2	R-HSA-69620	Cell Cycle Checkpoints			-14														-14
ME2	GO:0007017	microtubule-based process			-13							-7.5		-3			-7.5	-4.5	-13
ME8	GO:0002274	myeloid leukocyte activation			-4.4	-8.9						-3.6						-9.4	-9.4
ME8	M5930	HALLMARK EPITHELIAL MESENCHYMAL TRANSITION			-8.2	-7.2													-9.4
ME8	M5890	HALLMARK TNFA SIGNALING VIA NFKB				-6.6		-3.5											-6.6
ME8	M5885	NABA MATRISOME ASSOCIATED				-6.2													-6.2
ME8	GO:0030155	regulation of cell adhesion				-5.8						-3.5					-4.6	-5.1	-5.8
ME5	R-HSA-446203	Asparagine N-linked glycosylation						-6.1											-6.1
ME5	GO:0016050	vesicle organization			-3.6			-4.7									-4.2		-4.7
ME5	R-HSA-8953854	Metabolism of RNA		-5.3				-4.4	-15	-6.4			-8.8	-4.9			-10		-15
ME5	GO:0043632	modification-dependent macromolecule catabolic process			-6.2			-4.2	-6.4								-8.3		-8.3
ME5	GO:0051640	organelle localization			-7.1			-4.1									-6.1		-7.1
ME4	M5945	HALLMARK HEME METABOLISM										-8.8							-8.8
ME4	M5924	HALLMARK MTORC1 SIGNALING			-7.4							-6.6							-7.9
ME4	GO:0001944	vasculature development				-4.2						-6.1							-6.1
ME4	GO:0008015	blood circulation				-4.9						-5.6							-5.6
ME4	GO:0003013	circulatory system process				-5.5						-5.3							-5.5
ME1	GO:0045859	regulation of protein kinase activity			-8.5												-11		-11
ME1	R-HSA-8953854	Metabolism of RNA		-5.3				-4.4	-15	-6.4			-8.8	-4.9			-10		-15
ME1	GO:0016569	covalent chromatin modification															-10		-10
ME1	GO:0030031	cell projection assembly			-7.2						-7.2						-9.9	-4.4	-9.9
ME1	GO:0051301	cell division			-19												-8.6		-19
ME3	GO:0002274	myeloid leukocyte activation			-4.4	-8.9						-3.6						-9.4	-9.4
ME3	GO:0060627	regulation of vesicle-mediated transport			-3.9													-5.4	-5.4
ME3	GO:0030155	regulation of cell adhesion				-5.8						-3.5					-4.6	-5.1	-5.8
ME3	GO:0051129	negative regulation of cellular component organization			-3.9												-4.5	-4.9	-4.9
ME3	GO:0072657	protein localization to membrane			-3.4								-3.3					-4.7	-4.7

Table reports the top 5 enriched pathways in terms of Log FDR for each single gene list. Each row represents a pathway/biological process, and its code, name, and significance (Log FDR) in each reported list. Green scale highlights increasing significance (Log FDR) (from light to dark), white colour highlights Log FDR values higher than the statistically significance cut-off (-4) and grey colour highlights non-calculable Log FDR values.

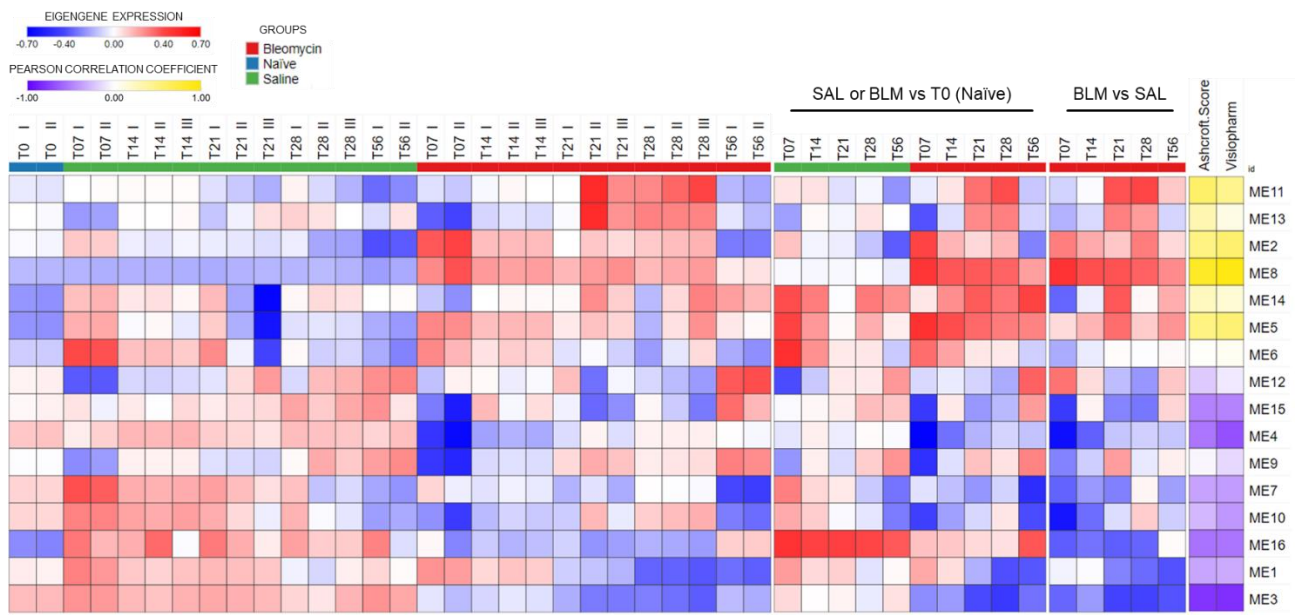***Figure 4.12*** *Heatmap of all the identified gene expression profiles. Each square represents the eigengene expression of a single biological condition (column) in a specific ME (rows). In the left part of the heatmap the eigengene expression for each biological replicate is reported, while in the right part the eigengene values are averaged and normalized vs the naïve animals (T0) or vs the corresponding SAL group, as reported above the column label. In the last two columns the Pearson correlation values between each ME and the two histological parameters are reported.*

4.3.5   Comparison with Other BLM-Induced Lung Fibrosis Murine Models and the Human Disease

To evaluate the strength and the overall consistency of the present transcriptome profiling, we compared our data with those of two time-course studies performed in other murine models of BLM-induced lung fibrosis. To achieve this aim, we applied the Gene Set Enrichment Analysis (GSEA) using different ranked lists based on $\log_2$ FC values for all the analysed time points or on the module membership (MM) values of the most informative MEs (see Materials and Methods section for further details).

GSEA analyses highlighted strong significant Normalised Enrichment Scores (NES) values between our model and the rat model described by Bauer et al. (2015)[52], especially regarding the up-regulated gene lists (upper-right panel in **Figure 4.13**). Statistically significant NES values were also obtained for the up-regulated gene lists reported in the mouse model published by Peng et al. (2013)[54] (lower-right panel in **Figure 4.13**). Some discrepancies were also evident, however, especially regarding the down-regulated gene lists (bottom part of the lower-right panel in **Figure**

4.13), thus pointing to as yet unexplained differences in the response to bleomycin between these two animal models. High statistically significant NES values were also obtained during the comparison of the list ranked based on MM with the list obtained from the rat model study, except for the module 1 that presented not statistically significant NES when compared with the down-regulated gene lists. Some differences were also identified comparing lists of down-regulated genes to lists derived from the reference mouse model. The ranked list that most of all reported high and significant NES in almost all the analysed lists was the module 8, the module that was associated with the long-lasting response to BLM and that was more correlated with histological parameters. These observations strongly suggest that, genes belonging to module 8 are the most representative of the fibrotic condition induced by BLM and this response was also preserved over time in other murine models, although they were treated with different experimental protocols.

The trend of the NES was consistent with the profile of eigengene expression of the modules when compared with the published up- and down- regulation gene lists, in fact, modules that had a profile mainly characterized by down-regulation had positive NES when compared with lists of down-regulated genes, while they had negative NES when compared with lists of up-regulated genes, the same concept was also true in opposite condition for those modules that had a profile mainly characterized by up-regulation (refer to **Figure 4.11** for the profile of the most informative MEs).
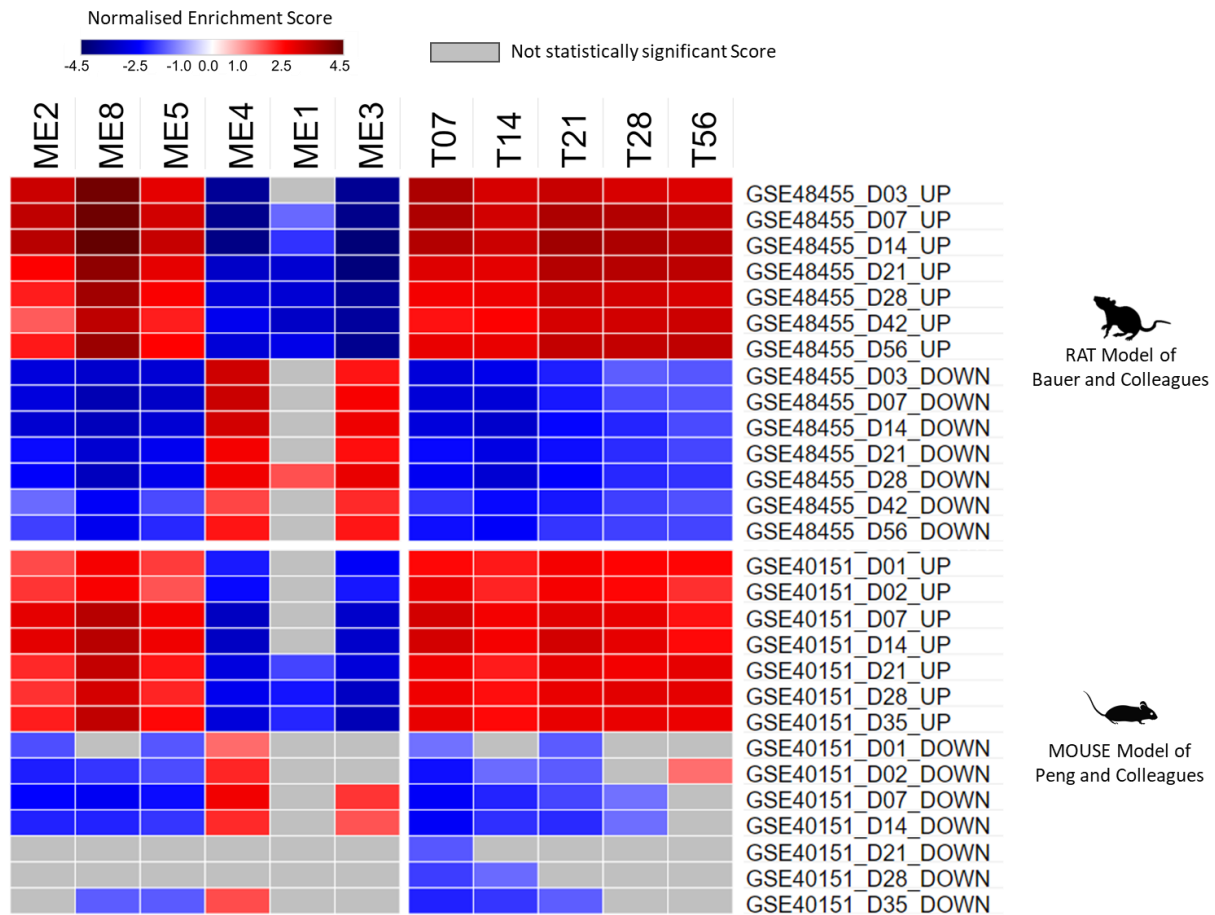
Figure 4.13 *Transcription profiles comparison with other BLM-induced lung fibrosis murine models. Results of Gene Set Enrichment Analysis of different BLM animal models in the identified time gene signatures. The degree of enrichment of each analysed gene set (reported in rows with the GeneOmnibus (GEO) accession number followed by a short description of the lists) was determined against a pre-ranked lists based on MM in the most informative MEs or on log_2 FC in each time point of the experiment (in column). The statistically significant (FDR ≤ 0.05) NES for each combination are plotted in the heatmap with a scale form dark blue to dark red as reported by the legend.*

A similar analysis was performed using list of de-regulated genes obtained from 9 different gene expression data human studies obtained on lung parenchyma samples from patients with IPF[69–77]. This analysis aimed to identify any analogies at the transcriptomic level between the animal model and human pathology, an essential step to evaluate the translational potential of the rat model characterised in this study. Also in this analysis, the comparison was performed using different ranked lists based on log_2 FC values for all the analysed time points or on the module membership (MM) values of the most informative MEs.

As already observed in the comparison with animal models, also in the comparison to human data, the GSEA highlighted high statistically significant NES, mainly with lists of up-regulated genes (right part of the **Figure 4.14**) and the highest values were relative to the ranked lists of the last 3 time points. However, in this case the NES values were generally lower respect to the previous analysis, and some lists did not demonstrate any statistically significant NES. This was expected considering the differences between animal model and human pathology and the extreme heterogeneity of sampling and analysis carried out on human samples. Moreover, a recent study reported on the heterogeneity in IPF-related transcriptomic studies[77]. Concerning the MM-based ranked lists, once again the module 8 is the one that got the highest and most significant NES for almost all the analysed human-lists emphasizing even more the importance of the genes included in this module, as can be seen in the left part of **Figure 4.14**. Similarly, the module 3 (the other module significantly correlated with histological parameters) provided good NES when compared with up-regulated gene lists, but, unlike ME8, it showed almost no match when compared with down-regulated gene lists.
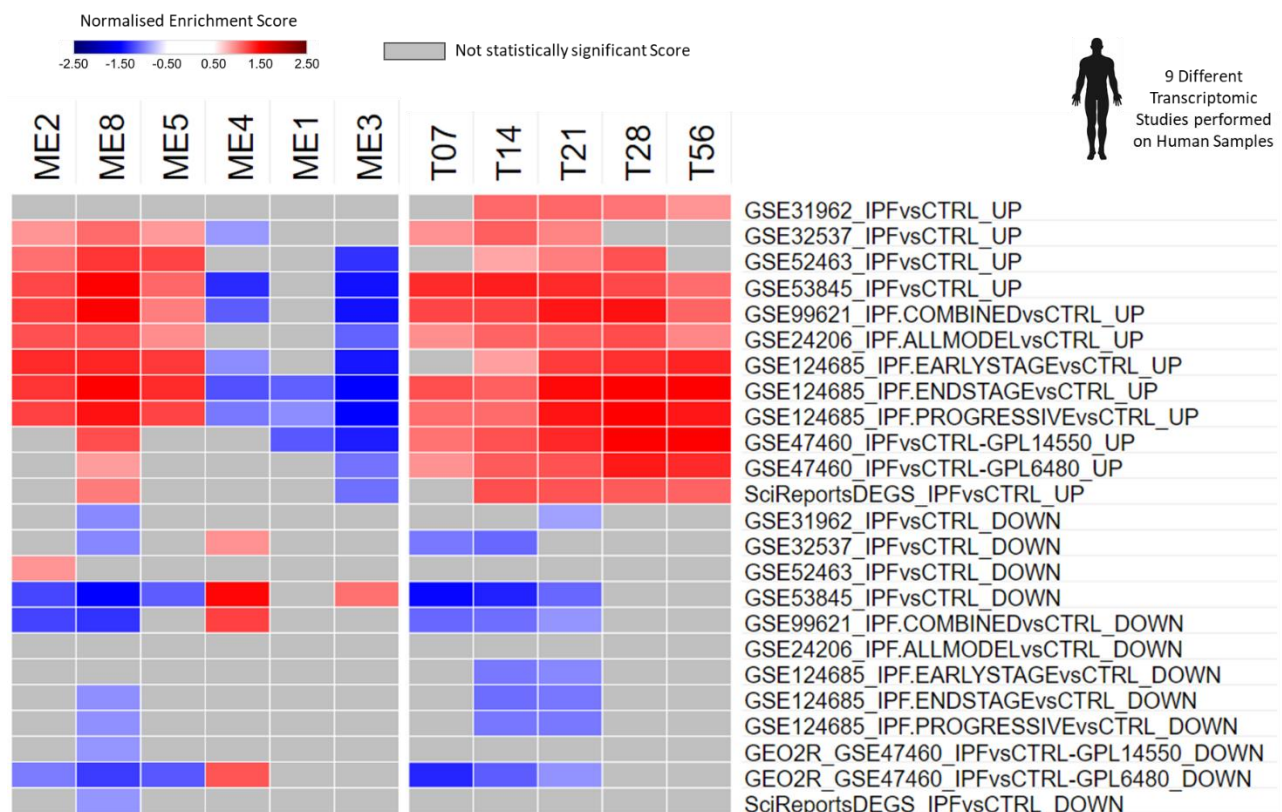
Figure 4.14 Transcription profiles comparison with IPF signatures. Gene Set Enrichment Analysis of different human IPF studies in the identified time gene signatures. The degree of enrichment of each analysed gene set (reported in rows with the GEO accession number followed by a short description of the lists) was determined against a pre-ranked lists based on MM in the most informative MEs or on log₂ FC in each time point of the experiment (in column). The statistically significant NES for each combination are plotted in the heatmap with a scale form dark blue to dark red as reported by the legend.

Considering the high information value of ME8 and its "affinity" with other IPF-related studies, especially those performed on human samples, we wanted to identify which genes of this module were the most important and translationally relevant. To do this, we used the leading-edge analysis of GSEA; this tool can identify subsets of the core genes that leads the enrichment score of the GSEA. From this analysis, we selected genes that more frequently contributed to the formation of NES during the comparison with human lists (genes identified in at least 7/12 lists of up or down-regulated genes). After, from this subset, we removed genes with a MM for the ME8 ranging from 0.7 and -0.7. The obtained gene list was subjected to GeneMania online source, to identify possible connections between the selected genes (gene with no connection were discarded). The obtained

network was elaborated with Cytoscape to highlight relevant information related to the selected genes. A complete list of these genes is reported in **Table 4.4**, while the network is showed in **Figure 4.15**.

Table 4.4 *Gene description of translationally relevant genes identified in Module 8 with a short description of the principal features.*

Gene Symbol	Gene Name	Protein Location	Protein Type
VCAM1	vascular cell adhesion molecule 1	Plasma Membrane	transmembrane receptor
CA4	carbonic anhydrase 4	Plasma Membrane	enzyme
COL3A1	collagen type III alpha 1 chain	Extracellular Space	other
TIMP4	TIMP metallopeptidase inhibitor 4	Extracellular Space	other
SULF1	sulfatase 1	Cytoplasm	enzyme
ASPN	asporin	Extracellular Space	other
COL1A1	collagen type I alpha 1 chain	Extracellular Space	other
CTHRC1	collagen triple helix repeat containing 1	Extracellular Space	other

| Gene Symbol	Gene Name	Protein Location	Protein Type
FHL2	four and a half LIM domains 2	Nucleus	transcription regulator
FNDC1	fibronectin type III domain containing 1	Plasma Membrane	other
GREM1	gremlin 1, DAN family BMP antagonist	Extracellular Space	other
IL13RA2	interleukin 13 receptor subunit alpha 2	Plasma Membrane	transmembrane receptor
COL1A2	collagen type I alpha 2 chain	Extracellular Space	other
SPP1	secreted phosphoprotein 1, or osteopontin	Extracellular Space	cytokine
THBS2	thrombospondin 2	Extracellular Space	other
TMEM100	transmembrane protein 100	Plasma Membrane	other
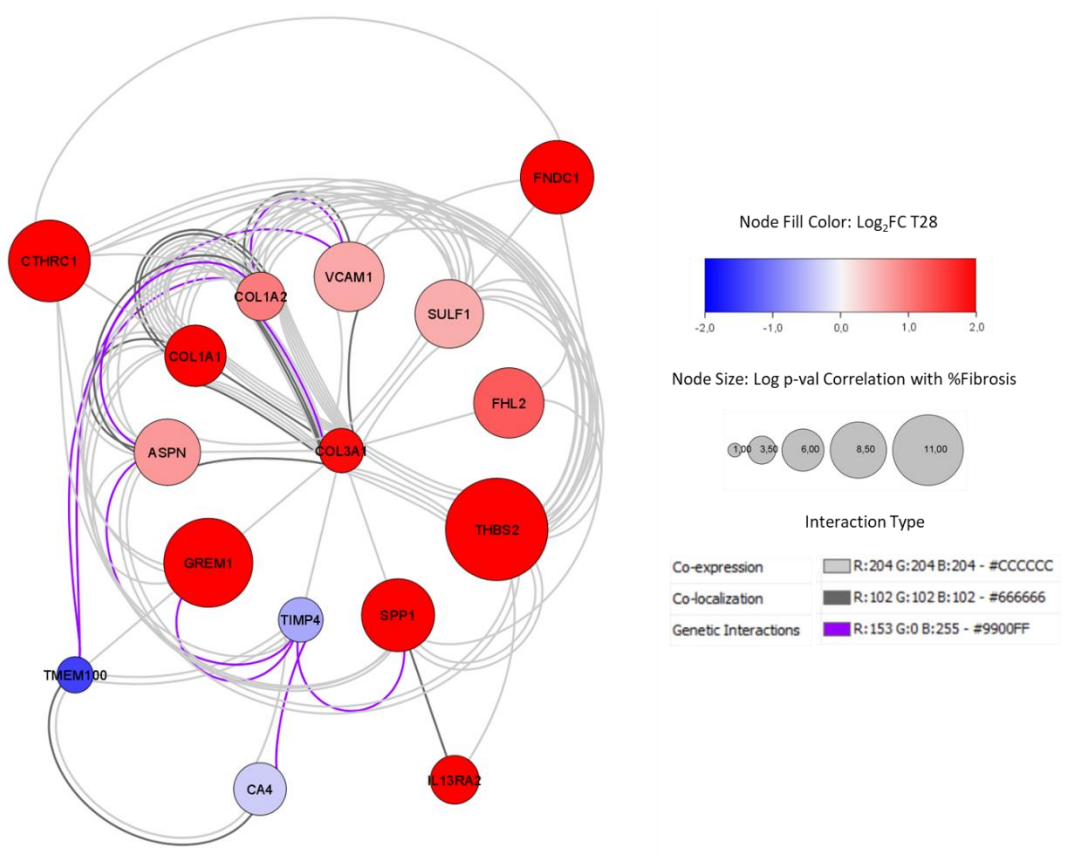
Figure 4.15 *Network realised using important genes in the association between ME8 and human studies. Characteristics of nodes and edge are reported in the legend.*

4.3.6 Validation of the RNA sequencing results

An accurate selection was made to select a set of 92 genes, which according to our results, were extremely representative of the crucial points of the development of lung fibrosis and could have a good diagnostic potential. These genes were selected based on the data obtained in the transcriptome profile analysis and on data published in the literature and the selection has been articulated in several points by applying increasingly stringent conditions, which will not be presented in the thesis for confidentiality reasons. The selection issued in the realization of an easy-to-assay qPCR Array (custom RT^2 Profiler PCR array provided by Qiagen), a reliable tool for analysing the expression of a focused panel of genes. Whenever it is necessary to evaluate the anti-fibrotic potential of a molecule in normalizing the gene expression levels altered by the fibrotic effect of the BLM this tool could be easier and faster than to perform an RNAseq analysis. The same PCR array was used for the validation of RNAseq data and even if it is not possible to publish the complete list of genes included in the array, an heatmap was made to compare the $\log_2$ FC values obtained with the two different techniques. Moreover, a similarity matrix to quantify the degree of similarity between the different list of $\log_2$ FC values is reported in the **Figure 4.16**. A high correlation between the data obtained with RNAseq and RT-PCR was observed even if this was more consolidated for the T07, T14 and T21 time points (Pearson Correlation values higher than 0.9). As an example, $\log_2$ FC values obtained with the two techniques for four genes, included in the PCR array, are reported in a bar graph (**Figure 4.17**).

Moreover, to further strengthen the validation, a couple of ELISA assays were performed to compare the protein levels with the mRNA. Two commercially available kits were chosen for this analysis since in the past they had given easily detectable and convincing results on the rat model experiments. The ELISA kit was performed using the same total right lung homogenate used for the HYP quantification. As reported in **Figure 4.18**, the proteins chosen for the analysis showed the same

deregulation profile reported by gene expression levels, with some slight variations, which were expected considering that the data were obtained starting from biological preparations of two different animals and that they refer to two diverse macromolecules with different half-lives and turnover.
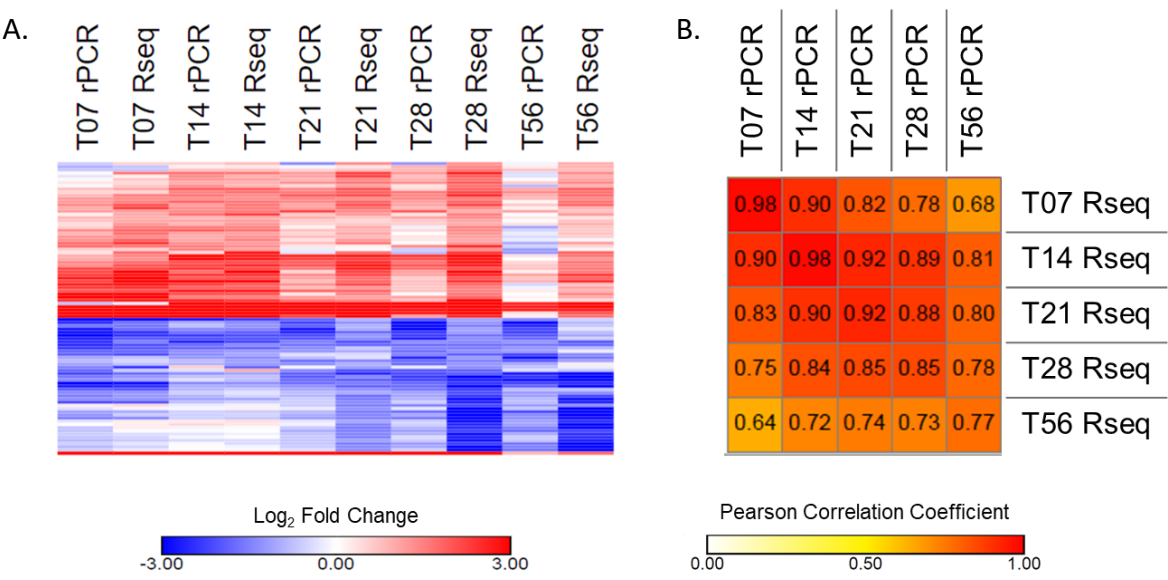
Figure 4.16 *log₂ FC comparison between the two techniques of RNA quantification. **A.** Heatmap of the gene expression level of all the selected genes obtained with RNAseq (Rseq) or RT-PCR (rPCR). **B.** Similarity matrix obtained using a Pearson Correlation metric.*
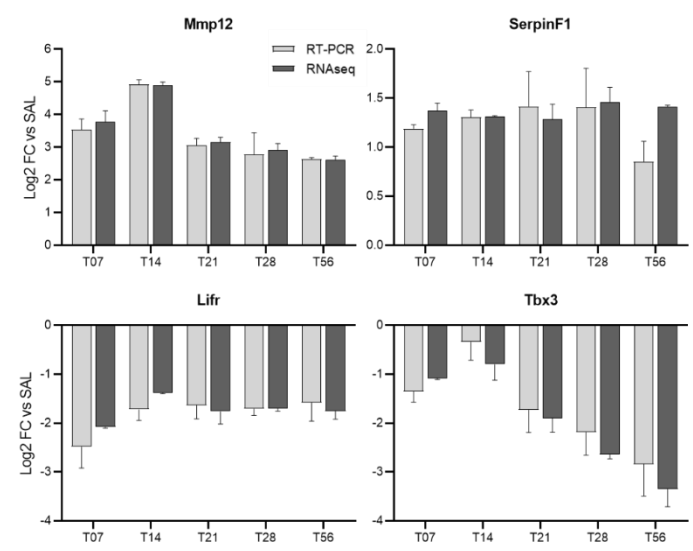
Figure 4.17 *log₂ FC comparison between the two techniques of RNA quantification of Matrix Metallopeptidase 12 (Mmp12, alias Macrophage Elastase (ME)), Serpin Family F Member 1 (SerpinF1, alias Pigment Epithelium-Derived Factor (PEDF), Leukaemia Inhibitory Factor Receptor (Lifr, alias Cluster of Differentiation 118 (CD118), and T-Box Transcription Factor 3 (Tbx3).*
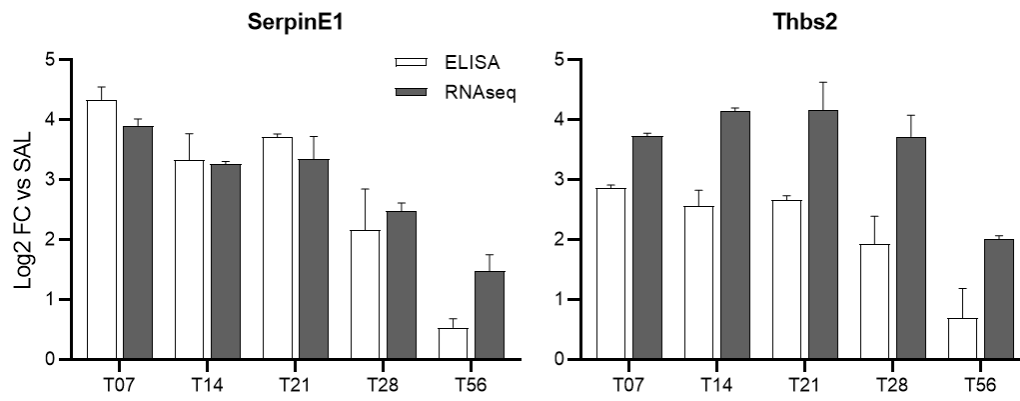
Figure 4.18 Differential quantification of Protein and RNA deriving from the same gene, Serpin Family E Member 1 (Serpine1, alias Plasminogen Activator Inhibitor Type 1 (PAI-1)) and Thrombospondin 2 (Thbs2).

4.4 Dose Response Study of a Clinically Approved BLM

Despite the information of considerable value collected in the time course experiment and the evident fibrotic response that developed over time, we observed a high mortality rate and the weight loss of the animal treated with BLM came very close to the minimum threshold tolerated by the regulatory rules for the treatment of laboratory animals, which is set at -20%. Moreover, from other internal experiments emerged that the BLM provided by Sigma-Aldrich even if carefully weighed and processed to give the desired dose, can be subject to incalculable variations and it may contain contaminants such as lipopolysaccharides, that could alter the specific activity of the molecule in a batch-dependent manner. For these reasons, and with the aim to set a BLM dosage able to induce a sub-maximal fibrotic response with an acceptable tolerability and in addition useful for analysing the potential anti-fibrotic effect of a molecule (this aspect will be more discussed in the next section "Discussion and Conclusion"), we decided to perform a dose response study using a BLM preparation for clinical use that does not present contaminants and does not have variations in terms of activity between different product batches (Good manufacturing practices (GMP) approved). T28 was the time point chosen to analyse the resulting pro-fibrotic effect, because according to the data obtained in the time course experiment at this time point the fibrotic response appeared to be stable, with dense and compact fibrosis and weak inflammatory component. Finally, this later time-point could allow a longer temporal window for a potential therapeutic treatment in the model.

4.4.1 Body weight trend, lung/body ratio and survival

BLM induced a dose-dependent effect on the weight of animals (**Figure 4.19**). Indeed the weight curve of the group treated with the highest dose of BLM was very far from that of the SAL-treated animals, showing a much slower weight recovery than the other groups, while for the two group of animals treated with the BLM doses of 0.5 and 1 U/Kg, although they have curves shifted from those

of control animals, the weight difference loses significance before the end of the experiment compared to the SAL group. The BLM administration of 2 U/Kg x2 induced a significant weight loss in the first days after treatment, with a peak of minimum body weight value around the sixth day, where the animals of this group lost on average $\simeq$8% of their original weight. Conversely, the animals treated with the two lower doses of BLM do not lose weight in the first days after treatment, but in these two groups the normal weight gain is slowed by the effect of BLM.

At the end of the experiment the weight of the lungs of the BLM groups were significantly higher respect to the control group in a dose-dependent manner.
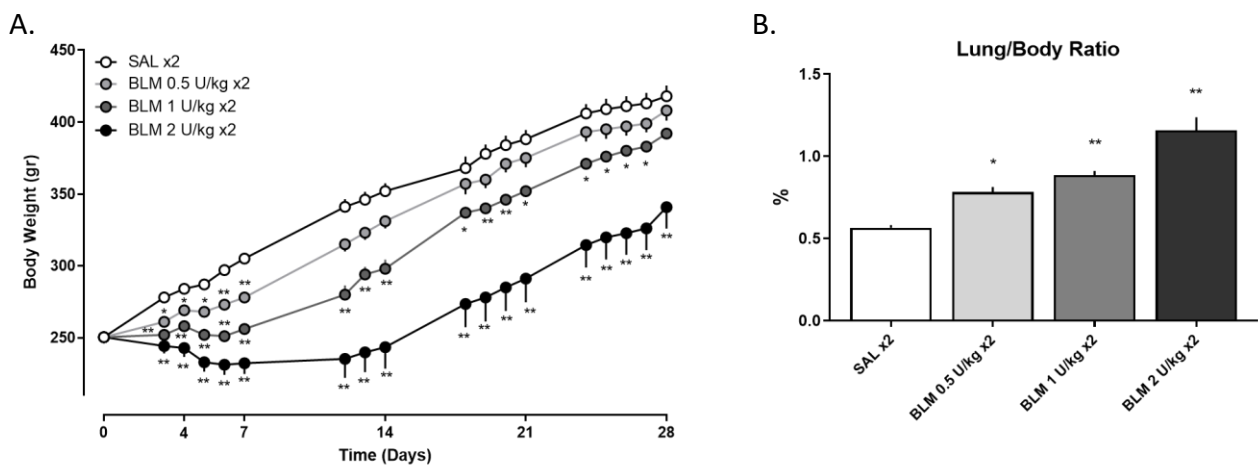
Figure 4.19 A. *Body weight trend. The weight was expressed as raw value (mean ± SEM) for each group of animals. *p<0.05, ** p<0.01 vs SAL.* ***B.*** *The lung/body ratio trend. Each column bar represents the mean value (± SEM) of the lung/body ratio (%). * p-val ≤ 0.05, ** p-val ≤ 0.01 vs SAL. For both the graphs the statistical analysis was performed using One-Way ANOVA or Kruskal-Wallis test followed by Dunnett or Dunn's test for multiple comparison.*

During the experiment, a $\simeq$17% of mortality was observed in the group of animals treated with the highest dose of BLM, similarly to what happened in the time course experiment as showed in the survival graph at **Figure 4.20**. No mortality was registered for the other two doses.
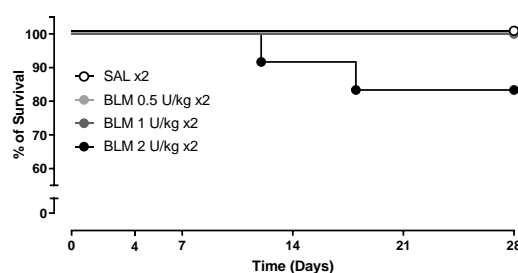
Figure 4.20 *Survival graph. Each point represents a death and contributes to lowering the line of survival.*

4.5   Histological and molecular Evaluation of lung fibrosis induced by increasing dose of clinical-approved BLM

4.5.1   Histological quantification of lung fibrosis

The software that performed the automatic quantification of lung fibrosis reported that the area of fibrotic tissue in the BLM-treated groups was significantly higher than the control group ($\simeq$ 27 % for the lowest dose, $\simeq$ 26% for the intermediate dose and $\simeq$ 35% for the highest dose, **Figure 4.21**). The analysis, performed using a score evaluation method based on Ashcroft scale, highlighted a higher median Ashcroft score for the BLM-treated animals which was dose-dependent (the value changed from 3.08 to 3.56 to 4.10, at 0.5, 1 and 2 U/Kg respectively, as showed by the left part of **Figure 4.21 B**). Despite this, the increase was not statistically significant for the BLM 0.5 U group. The severity of the scores also tended to increase as the dose of BLM increased, as reported in the right part of **Figure 4.21 B.**
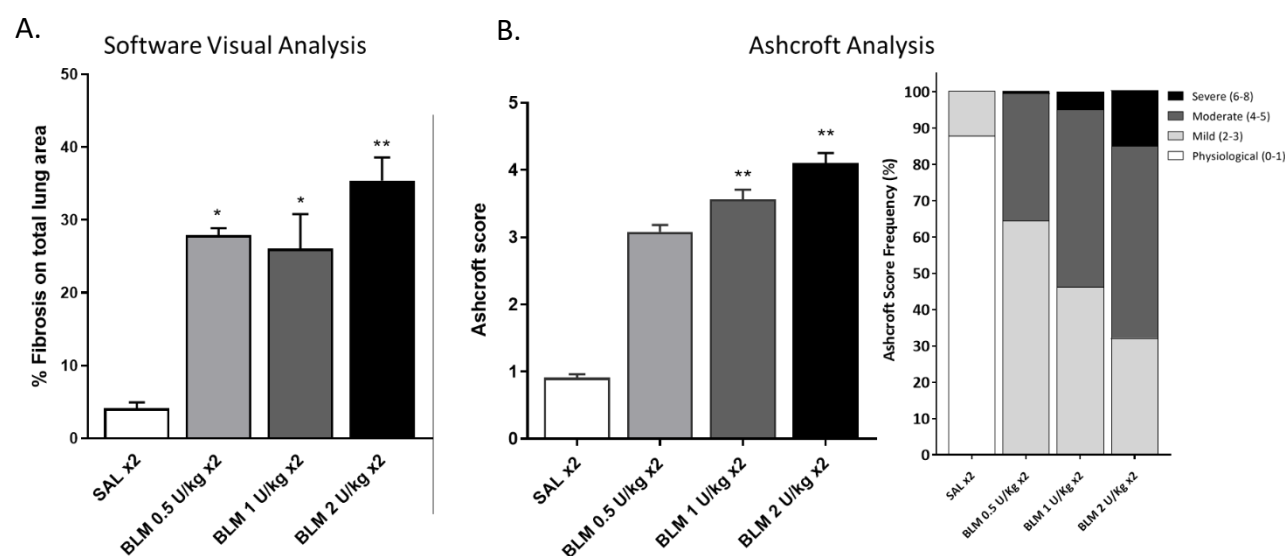
Figure 4.21 *Quantification of pulmonary fibrosis using the Software Visual Analysis (A) and the Ashcroft Score method (B) in all the analysed group.* ***A.*** *Bar chart representing the percentage of fibrosis on the total lung area identified with the software visual analysis, each bar is reported as mean ± SEM. *p<0.05, ** p<0.01 vs SAL.* ***B.*** *On the left: Bar chart representing the Ashcroft score mean values ± SEM. ** p<0.01 vs SAL. On the right: the frequency of distribution of the different score divided into four categories of severity as report in the legend. The statistical analysis was performed on A and left B using One-Way ANOVA or Kruskal-Wallis test followed by Dunnett or Dunn's test for multiple comparison.*

4.5.2 Estimated Quantification of Lung Collagen Content

The HYP content was assessed in the right lung homogenate and its level grew in a dose dependent manner (**Figure 4.22**). Indeed, the level of HYP is significantly increased in all the BLM group compared to SAL group.
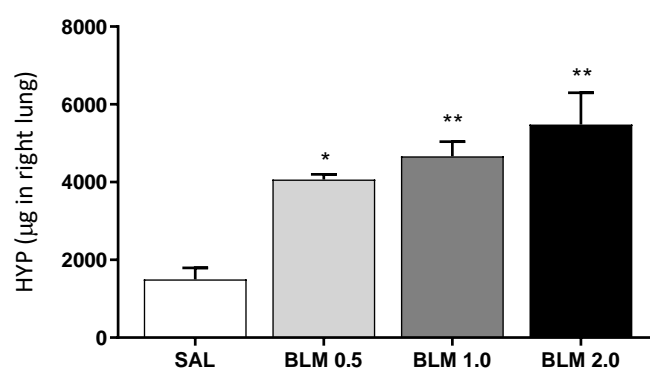
Figure 4.22 HYP content in total right lung homogenate. Data are expressed as mean ±SEM. *p<0.05, **p<0.01 vs SAL. Statistical analysis performed by One-Way ANOVA or Kruskal-Wallis test followed by Dunnett or Dunn's test for multiple comparison.

4.6 Curative protocol study with nintedanib

Once the time point and the correct dose of clinical-approved BLM were defined, the model was ready to test the effect of an anti-fibrotic drug. For this reason, it was decided to design a curative experiment using one of the two drugs approved for the treatment of IPF, nintedanib. This pharmacological study would provide, in case of a positive result from the molecule, the functional validation of the model and, at the same time, would allow a better understanding of the mechanisms underlying the curative effect of an anti-fibrotic drug, which produces on IPF patients an ameliorative effect on lung function parameters and leads to a slowdown in the disease progression (as described in section 1.5.2 "The New Paradigm of IPF - The Age of The Anti-Fibrotic Drugs")

4.6.1 Body weight trend, lung/body ratio and survival

The BLM administration induced a weight loss in the first days after treatment, with a peak of minimum body weight value around the seventh day, where the animals treated with BLM lost on average ≃4% of their original weight. In the following days, the BLM-treated animals recovered weight with a regular and progressive trend until the end of the experiment. The animals treated with nintedanib showed a faster weight recovery in the first week of treatment, however, starting from day 21 and until the end of the experiment, they tended to reduce considerable their weight recovery trend and their mean weight value was surpassed by that registered in animals treated with bleomycin alone (**Figure 4.23 A**).

At the end of the experiment the weight of the lungs of the BLM group were significantly higher respect to the control group (SAL); interestingly, the animals treated with nintedanib recorded a significant decrease in the weight of the lungs being the value very close to the control group (**Figure 4.23 B**).
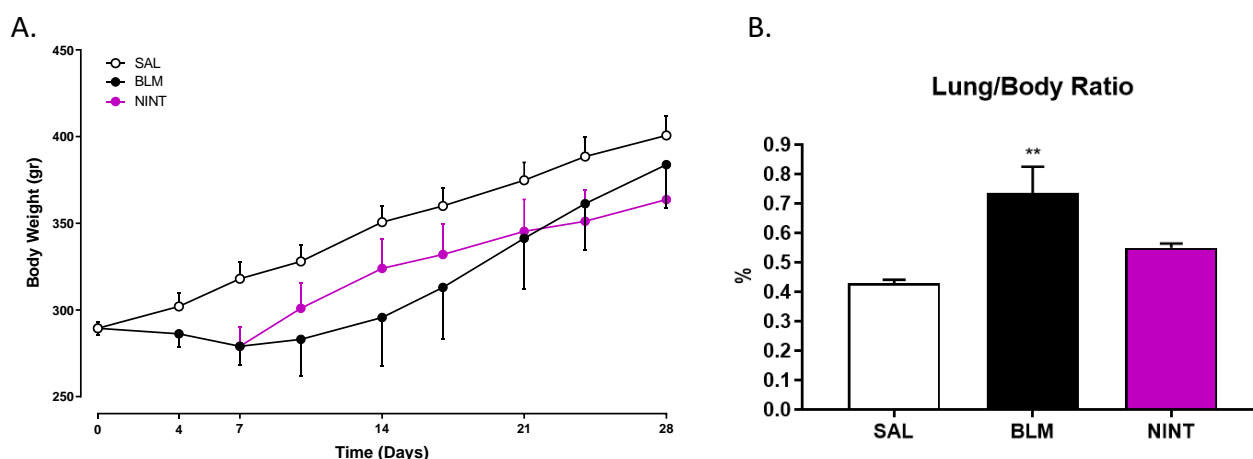
Figure 4.23 A. *The body weight trend. For each group of treatment, the values are expressed as a mean ± SEM.* **B.** *Each column bar represents the mean value (± SEM) of the lung/body ratio (%). ** p-val ≤ 0.01 vs SAL/VEH. Statistical analysis performed with Kruskal-Wallis test followed by Dunn's test for multiple comparison.*

During the experiment, no mortality was observed.

4.6.2   Blood analysis

As reported in **Table 4.5**, no great differences were observed in the total blood WBC counts among the different groups of treatment. However, a reduction of neutrophils and eosinophils in the nintedanib group has been observed, highlighting a possible systemic anti-inflammatory effect of the molecule. The effect is more clear looking at the percentages of the different cell populations compared to the total WBCs (**Figure 4.24**).

Table 4.5 Number of total and differential WBC of saline and bleomycin groups at each time-point expressed as mean value.

Group of Treatment	Total WBC mean (10^6/ml)	Monocytes mean (10^6/ml)	Neutrophils mean (10^6/ml)	Lymphocytes mean (10^6/ml)	Eosinophils mean (10^6/ml)
SAL	9.72	0.39	0.81	8.38	0.12
BLM	9.59	0.47	0.89	8.04	0.17
NINT	10.73	0.54	0.47	9.64	0.07**

*** p-val ≤ 0.01 vs BLM/VEH. Statistical analysis performed with Kruskal-Wallis test followed by Dunn's test for multiple comparison.*
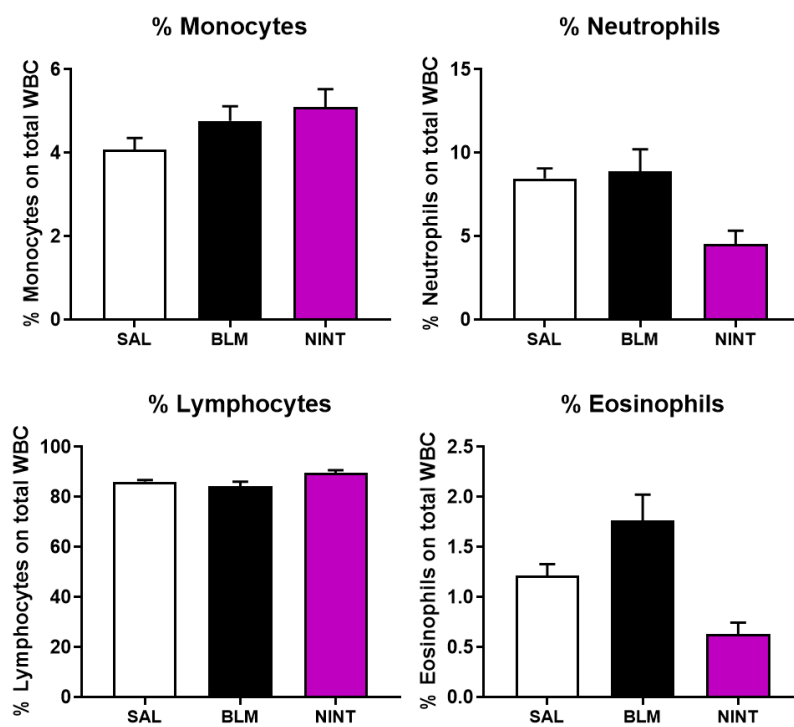
Figure 4.24 WBC differential cells count expressed as percentage (mean value ±SEM) respect to total WBC.

4.7 Histological Evaluation of the Therapeutic Potential of the Molecule on the BLM-Induced Lung Fibrosis

As shown in **Figure 4.25**, the Masson's trichrome stained lung slides obtained in this study revealed that at day 28 BLM induced lung fibrosis consisted of collagen deposition and dense clusters of inflammatory cells. In the BLM group, areas of normal lung parenchyma were replaced with dense collagen agglomerates where alveoli were not well identifiable. However, in the nintedanib group (for almost all the animals) the collagen deposition appeared diffuse through the tissue. Moreover, in this group the alveoli were clearly visible even if the septa were more thickened than in the control group.
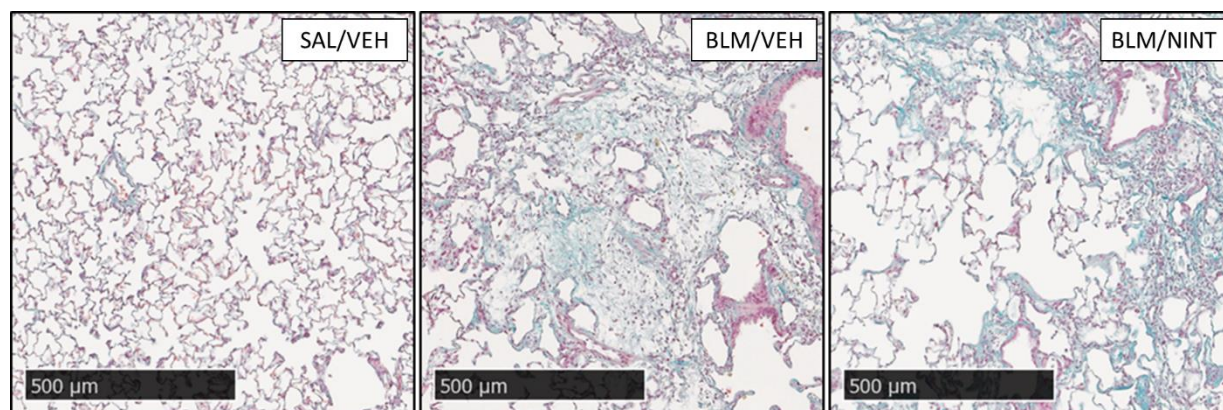
Figure 4.25 Representative Masson's trichrome stained lung sections details. All the images derive from different rats (the name of the group was reported in the upper right corner label). Scale bar = 500 µm.

These qualitative observations were confirmed and supported by the two semi-quantitative analysis performed in this study (**Figure 4.26 A-B**). Indeed, the software that performed an automatic quantification of lung fibrosis reported that the area of fibrotic tissue of the BLM group was significantly higher than the control group (25% of the total lung area). The fibrotic area quantified in the nintedanib group was lower than the BLM group ($\simeq$15% of the total lung area), even if the compound effect was not statistically significant. Moreover, the Ashcroft score analysis highlighted a substantial reduction of the median Ashcroft score of the nintedanib group respect to the BLM

group (the value changed from 3.62 to 2.94). The differences between these two groups were even more evident looking at the different degrees of severity of fibrosis (right part of **Figure 4.26 B**). Indeed, in the group treated with nintedanib there was a reduction in the percentage of moderate scores on behalf of mild scores compared with those obtained by the BLM group.
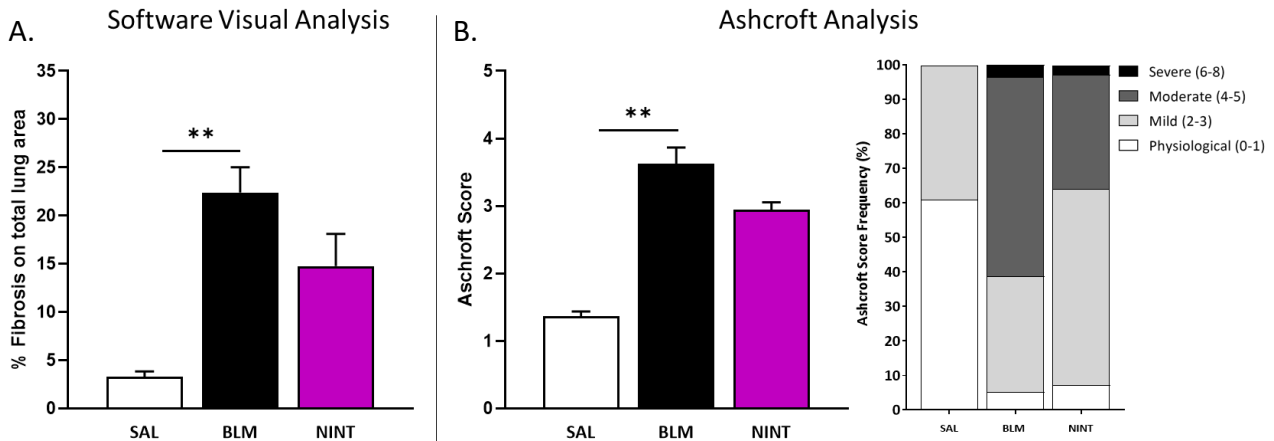
*Figure 4.26 Quantification of pulmonary fibrosis using the Software Visual Analysis (**A**) and the Ashcroft Score method (**B**) in all the analysed group. **A.** Bar chart representing the percentage of fibrosis on the total lung area identified with the automated quantification, each bar is reported as mean ± SEM. **B.** Bar chart representing the Ashcroft score mean values and the frequency of distribution of the different score divided into four categories of severity as report in the legend. The statistical analysis was performed on A and left B using Kruskal-Wallis test followed by Dunnett or Dunn's test for multiple comparison. ** p-val ≥ 0.01 vs SAL.*

4.8 Whole Transcriptomic Effect Induced by the Molecule on BLM-altered Lung Transcriptome

4.8.1 General Transcriptomic Data

A Principal Component Analysis (PCA) calculated on the RNAseq data of this study revealed a clear separation between samples represented by SAL-treated rats (green) on the left. Rats belonging to the nintedanib group (red) clustered together, while the 4 animals of the BLM group (light blue) were more dispersed with one sample (BLM2) closer to the nintedanib and SAL groups and one (BLM3) very far from the control group.
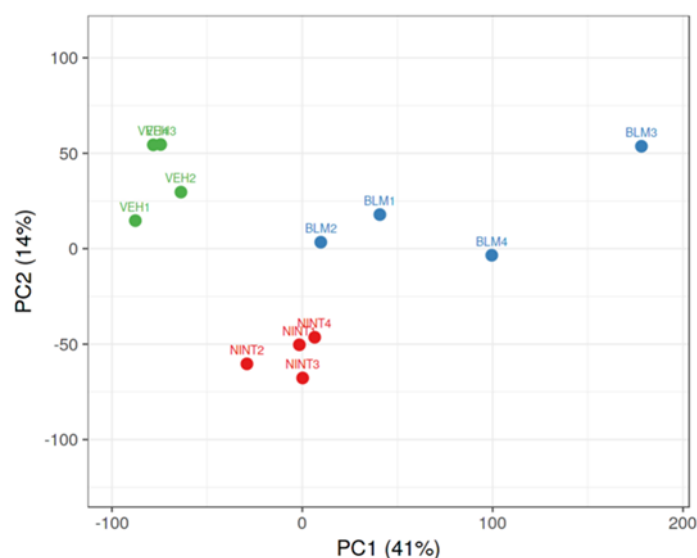
Figure 4.27 *Graphical representation of the PCA.*

4.8.2 Differentially Expressed Genes (DEGs) Analysis

The number of DEGs ranged from 815 (NINT vs SAL) to 1440 (BLM vs VEH), for a total of 1726 DEGs (**Figure 4.28 A**). Down-regulated genes prevailed over up-regulated genes, as already assessed at T28 in the transcriptomic analysis of the time course study. 133 of the 205 up-regulated genes identified in the comparison NINT vs SAL were shared with BLM vs SAL up-regulated list, but there were 172 up-regulated genes in the comparison BLM vs SAL that resulted not significantly modified in the comparison NINT vs SAL, as showed in the Venn diagram (**Figure 4.28 B**).

Similarly, 478 of the 610 down-regulated genes identified in the comparison NINT vs SAL were shared with BLM vs SAL down-regulated list, but there were 657 down-regulated genes in the comparison BLM vs SAL that resulted not significantly modified in the comparison NINT vs SAL (**Figure 4.28 C)**.
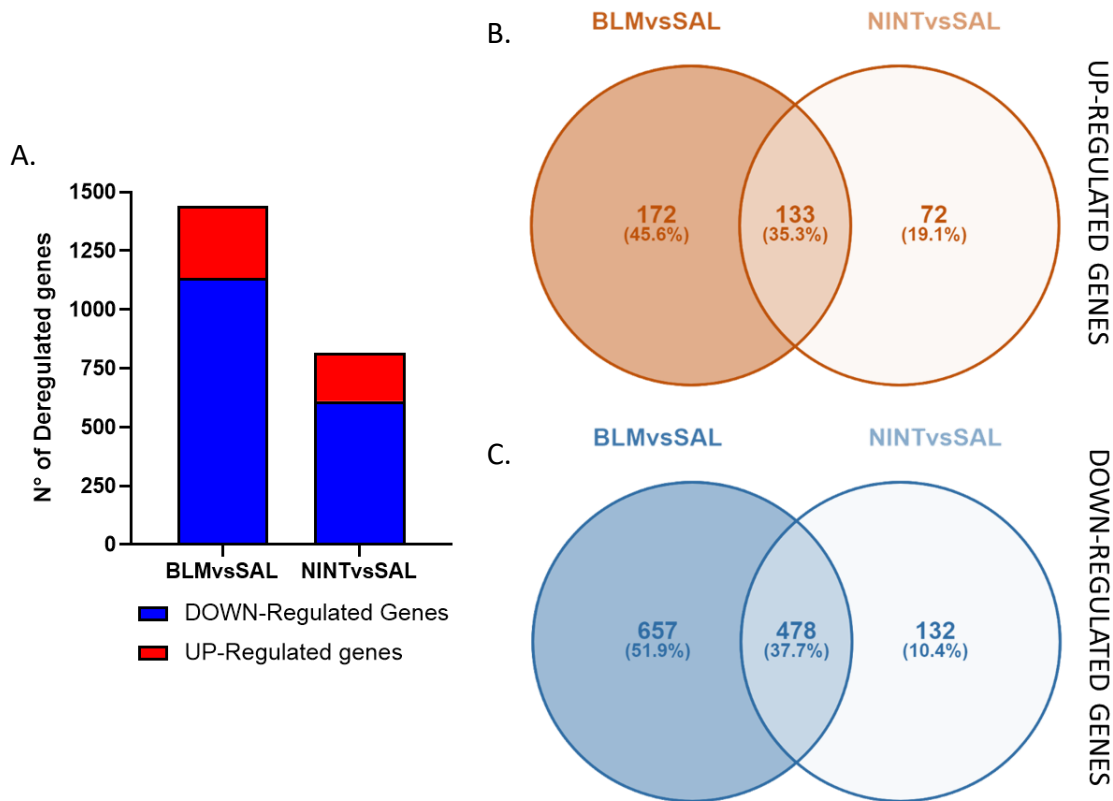
Figure 4.28 DEGs analysis. *A. Number of differentially expressed genes (DEGs) in different comparisons. B. Venn diagram showing the overlap of up-regulated genes between the indicated comparisons. C. Venn diagram showing the overlap of down-regulated genes between the indicated comparisons.*

Differentially expressed gene profiles showed a milder dysregulation in BLM-replicate 2 (BLM2), as already suggested by the PCA analysis. As it happened for the time course experiment, the hierarchical clustering of genes whose expression levels changed significantly across the different groups of treatment highlighted a specific transcriptomic profile, which characterize the various effect of nintedanib on the BLM model. In detail, as showed in **Figure 4.29**, it was possible to identify genes modified in expression levels by the effect of BLM which were then cured by the nintedanib treatment (this effect could demonstrate an anti-BLM effect of nintedanib), genes which were

unchanged in expression levels in the BLM-SAL comparison but instead modified by the effect of nintedanib (this profile could be related to the effect of nintedanib on genes not influenced by BLM) and genes on which nintedanib had no ameliorative effect (no effect of nintedanib). Moreover, in terms of variability in the response of animals, the heatmap showed in the left part of **Figure 4.29** displayed a milder dysregulation in BLM replicate 2 and a stronger dysregulation in BLM replicate 3 as already suggested by the PCA analysis.
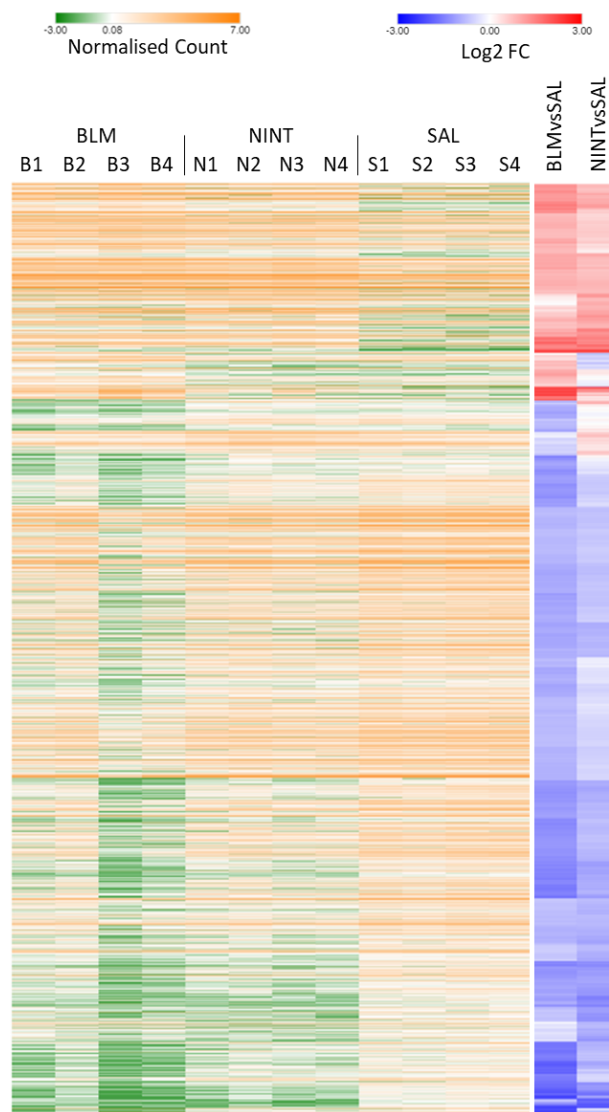
Figure 4.29 Left part: *Heat map of average normalized genes, showing all replicate samples over and under expressed genes are in orange and green respectively.* ***Right part:*** *Heat map of fold change values of the indicated comparisons, up regulated genes are shown in red and down regulated genes are in blue.*

4.8.3 Pathway Analysis on DEGs

Several pathways emerged as significantly enriched in the BLM vs SAL comparison list, and some of them were not significative anymore in the NINT vs SAL comparison, suggesting that Nintedanib was effective in modulation of some up- and down-regulated pathways. For example, "NABA Matrisome Associated" among the up-regulated pathways, and "Supramolecular Fiber Organization" among the down-regulated. Other pathways, like positive regulation of organelle organization and regulation of peptidase activity, were specifically up-regulated or down-regulated only in NINT vs SAL comparison. The Top 5 significant pathways and processes for each up- and down-regulated lists are reported in **Table 4.6**. A pathway was considered statistically enriched in a list if its Log FDR was higher or equal to -4.

*Table 4.6 Pathways enriched in DEGs lists derived from BLM vs SAL and NINT vs SAL comparison.*

TOP5	GO	DESCRIPTION	DN_BLMvsSAL	DN_NINTvsSAL	UP_BLMvsSAL	UP_NINTvsSAL	MAX
DOWN-REGULATED BLMvsSAL	GO:0097435	supramolecular fiber organization	-6.7	-2.4			-6.7
	GO:0032990	cell part morphogenesis	-6.5				-6.5
	R-HSA-109582	Hemostasis	-5.9	-4.4	-2.7	-2.2	-5.9
	GO:0033044	regulation of chromosome organization	-5.1	-3.8			-5.1
	R-HSA-422475	Axon guidance	-4.9	-2.8			-4.9
DOWN-REGULATED NINTvsSAL	GO:0010638	positive regulation of organelle organization	-2.3	-6.5			-6.5
	GO:0042692	muscle cell differentiation	-3.3	-5.4			-5.4
	GO:0044057	regulation of system process	-2.7	-4.9			-4.9
	R-HSA-109582	Hemostasis	-5.9	-4.4	-2.7	-2.2	-5.9
	R-HSA-112040	G-protein mediated events	-2.7	-4.4			-4.4
UP-REGULATED BLMvsSAL	GO:0045055	regulated exocytosis			-16	-9	-16
	M5885	NABA MATRISOME ASSOCIATED			-7.8	-3.7	-7.8
	hsa04610	Complement and coagulation cascades			-6.5	-6.1	-6.5
	GO:0002526	acute inflammatory response			-5.3	-6.8	-6.8
	GO:0002576	platelet degranulation			-4.6	-1.6	-4.6
UP-REGULATED NINTvsSAL	GO:0045055	regulated exocytosis			-16	-9	-16
	GO:0002526	acute inflammatory response			-5.3	-6.8	-6.8
	hsa04610	Complement and coagulation cascades			-6.5	-6.1	-6.5
	GO:0052547	regulation of peptidase activity			-2.7	-5.6	-5.6
	GO:0043062	extracellular structure organization	-1.8	-1.1	-2.2	-5.3	-5.3

Table reports the top 5 enriched pathways in terms of Log FDR for each single gene list. Each row represents a pathway/biological process, and its code, name, and significance (Log FDR) in each reported list. Green scale highlights increasing significance (Log FDR) (from light to dark), white colour highlights Log FDR values higher than the statistically significance cut-off (-4) and grey colour highlights non-calculable Log FDR values.

A network-based approach (WGCNA) was used to identify significant and specific transcriptional profiles and to convert the results of DEGs analysis into functionally relevant information for the model and for the effect of nintedanib. Unsigned WGCNA revealed 14 modules of co-regulated (or anti-regulated) genes, moreover, for each single module, the Pearson correlation with the corresponding values of Ashcroft Score and % of fibrotic tissue measured on lung sections of the same animals was calculated. The first four identified modules accounted for 83.4% of all the analysed genes, and module 1 alone included about half of them, while the remaining 10 modules contained less than 5% genes each. A pathway enrichment analysis, performed with Metascape, was applied to the WGCNA modules in order to identify specific genes and pathways associated to the effect of nintedanib. The individual expression profiles MEs of the most informative module are reported in **Figure 4.30**, while **Table 4.7** reports the TOP 5 enriched pathways of each of these modules. For a complete view of all the module identified in this experiment see **Figure 4.31.**

Only the module 1 significantly correlated with one of the two histological parameters, the Ashcroft Score, moreover, as noted in previous analyses, there was a discrete variability within the BLM group replicates. Among the most informative profiles, and as highlighted by the DEG analysis, there are two modules where the genes were modified by the BLM treatment and at the same time, they were responsive to the effect of Nintedanib despite with a different grade of impact: modules 1 and 2, which together contained nearly 70% of all genes used in WGCNA analysis. In the ME2 there was a strong deregulation, mainly focused towards the up-regulation, in the BLM vs SAL comparison and it was totally reduced by the nintedanib. Pathways enriched in this module were related to the cellular respiration and metabolism. Despite the significance values of the correlation with the external traits were not as high as those obtained for the time course experiment, however the Person values were greater than 0.75 for both histological parameters and both had a p-val lower than 0.01 (Pearson correlation p-val = 0.00053 and p-val = 0.0047 for the Ashcroft Score and %

Fibrosis respectively). In the ME1 there was a strong deregulation, mainly focused towards the down-regulation, in the BLM vs SAL comparison which was partially reduced by the effect of nintedanib. Pathways enriched in this module were related to cellular protein catabolic process, negative regulation of cellular component organization and cell projection assembly. This module registered a strong statistically significant negative correlation with the Ashcroft score, however the Person correlation with the % of fibrosis, even if it had a good correlation value (-0.79) did not have as high a level as that recorded for the other parameter (Pearson correlation p-val = 0.0023).

Considering the expression values, on modules 2 and 1 nintedanib had respectively a strong and mild effect in restoring the gene levels altered by BLM.

In addition to these two modules, other modules characterized by specific gene signatures were identified, one of these was represented by the effect of the molecule on genes not influenced by the BLM effect (module 3) and another one (module 4) was represented by a worse effect on genes affected by the effect of BLM.

In the module 3 the comparison between the levels of expression of the BLM group and the control group did not lead to any dysregulation, but a strong dysregulation, mainly focussed towards a down-regulation, was reported in the comparison NINT-SAL. This could be an evidence of the broad-spectrum effect of the molecule that doesn't necessarily affects only pro-fibrotic mechanisms induced by BLM. Interesting pathways enriched in this module were related to the morphogenesis of an epithelium and embryonic development.

In the ME4 there was a mild deregulation, mainly focussed towards the up-regulation, in the BLM vs SAL comparison which is worsen by the effect of nintedanib. Pathways and process enriched in this module were related to the protein degradation and modification and cell projection assembly.
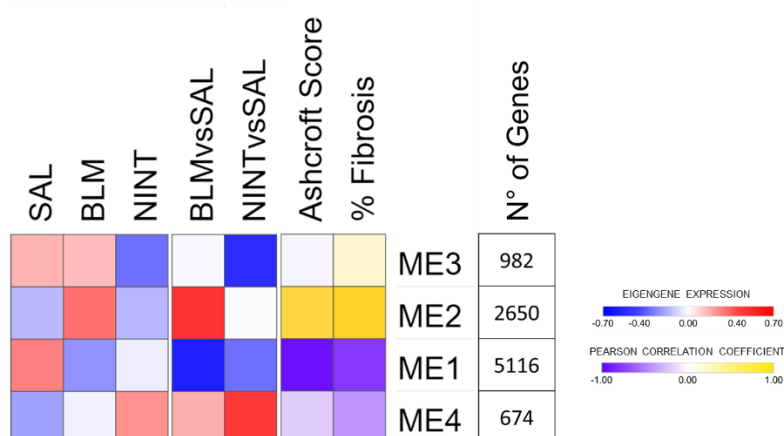
Figure 4.30 Heatmap of the most informative modules (represented by their MEs). We consider these MEs the most informative because modules 1 to 4 contain more than 83% of all the genes used for WGCNA. In the left part of the heatmap in column the biological condition is represented by the mean value of single biological replicates eigengene expression, while in the right part the biological conditions referrers to a direct comparison between SAL and the other groups as reported above the column label. The values are calculated averaging the values of eigengene expression of biological replicate and relating them to the control group (SAL). The two last right columns report the Pearson correlation value between each ME and the two histological parameters.
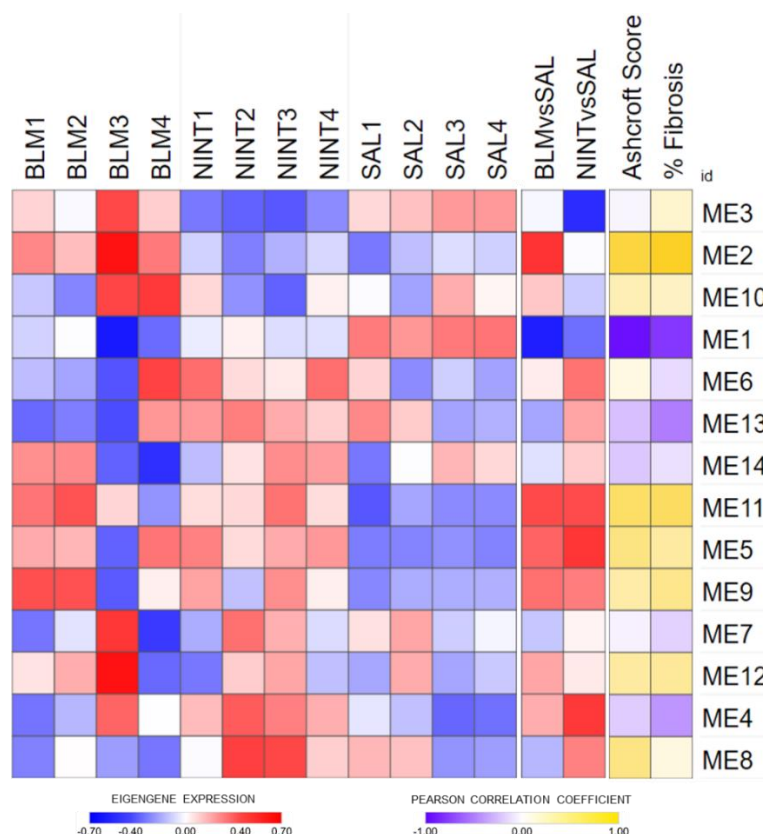
Figure 4.31 Heatmap of all the identified gene expression profiles. Each square represents the eigengene expression of a single biological conditions (column) in a specific MEs (rows). In the left part of the heatmap the eigengene expression for each biological replicate is reported, while in the right part the eigengene values are averaged and normalized vs the control group (SAL), as reported above the column label. In the last two columns the Pearson correlation values between each ME and the two histological parameters are reported.

Table 4.7 *Pathways enriched in gene list derived from the most relevant MEs.*

	GO	DESCRIPTION	ME3	ME2	ME10	ME1	ME6	ME13	ME14	ME11	ME5	ME9	ME7	ME12	ME4	ME8	MAX
ME3	GO:0044257	cellular protein catabolic process	-8.3	-11		-24	-3.5								-4.8		-24
	GO:0043009	chordate embryonic development	-7.5	-2.5		-8.7							-1.9				-8.7
	R-HSA-8953854	Metabolism of RNA	-7.4	-24		-22		-4.1			-3.7		-3.1	-1.6	-4		-24
	GO:0002009	morphogenesis of an epithelium	-6.8	-6.1		-6.3	-1.6						-2.2				-6.8
	GO:0034470	ncRNA processing	-6.4	-12		-2.6					-2.9				-2.7		-12
ME2	M5936	HALLMARK OXIDATIVE PHOSPHORYLATION		-32													-32
	GO:0007005	mitochondrion organization	-2.4	-29		-4.2	-2.3				-1.6		-1.8			-1.7	-29
	R-HSA-1428517	The citric acid (TCA) cycle and respiratory electron transport		-29			-2.1		-1.8								-29
	GO:0006091	generation of precursor metabolites and energy	-2.5	-27		-5.6			-2.5				-1.9	-1.6			-27
	GO:0045333	cellular respiration		-27					-2.5								-27
ME1	GO:0044257	cellular protein catabolic process	-8.3	-11		-24	-3.5								-4.8		-24
	R-HSA-8953854	Metabolism of RNA	-7.4	-24		-22		-4.1			-3.7		-3.1	-1.6	-4		-24
	GO:0051129	negative regulation of cellular component organization	-1.9	-4		-20	-2.4				-1.8				-2		-20
	GO:0030031	cell projection assembly		-4.5		-20	-3.2				-5.1			-1.8	-5.4		-20
	GO:0006397	mRNA processing	-5.2	-8.7		-19		-2.7									-19
ME4	R-HSA-8951664	Neddylation	-3.5	-4.5		-1.8									-6.7		-6.7
	GO:0030031	cell projection assembly		-4.5		-20	-3.2				-5.1			-1.8	-5.4		-20
	GO:0043687	post-translational protein modification	-3	-5.7		-4.8						-1.7			-5.3		-5.7
	GO:0044257	cellular protein catabolic process	-8.3	-11		-24	-3.5								-4.8		-24
	R-HSA-983169	Class I MHC mediated antigen processing & presentation	-3.6	-4.9		-4.6	-1.7						-2.1	-2.1	-4.3		-4.9

Table reports the top 5 enriched pathways in terms of Log FDR for each single gene list. Each row represents a pathway/biological process, and its code, name, and significance (Log FDR) in each reported list. Green scale highlights increasing significance (Log FDR) (from light to dark), white colour highlights Log FDR values higher than the statistically significance cut-off (-4) and grey colour highlights non-calculable Log FDR values.

4.8.4 Validation of the RNA sequencing results

In order to validate RNAseq results, gene expression of four genes modulated by BLM and normalized by nintedanib was evaluated. Even if in some cases there was not a perfect matching of the up and down-regulation values obtained with the two RNA-detecting techniques, the trend was confirmed for all 4 genes, as reported in **Figure 4.32.**
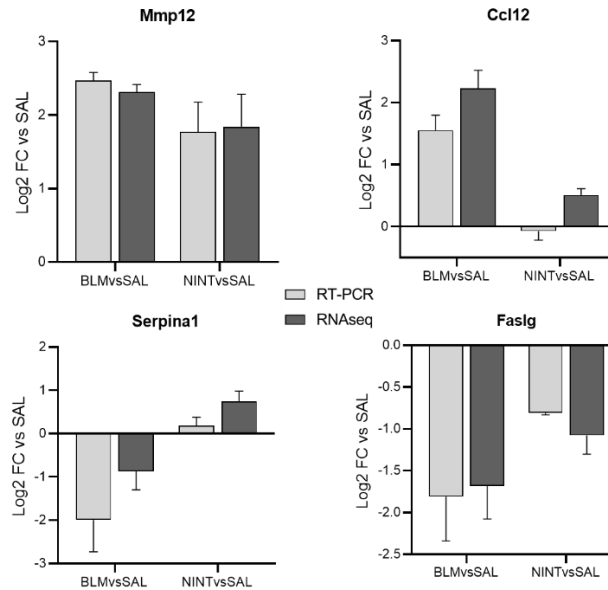
Figure 4.32 *log$_2$ FC comparison of Matrix Metallopeptidase 12 (Mmp12, alias Macrophage Elastase (ME)), Chemokine (C-C motif) ligand 12 (Ccl12, alias monocyte chemotactic protein 5 (Mcp-5)), Serpin Family A Member 1 (SerpinA1, alias Alpha-1-Antitrypsin (A1at)) and Fas Ligand (Faslg) between the two techniques of RNA quantification.*

4.8.5 Data comparison between the Time Course Study and the Curative protocol study with nintedanib

Considering the differences in terms of type and dose of BLM used in the two experimental protocols subjected to transcriptomic analysis, the similarity of the gene expression profiles induced by BLM was verified limited at the common time point, the T28. A direct comparison was made between all the genes identified in both experiments (13.965) and as showed in the first heatmap of **Figure 4.33**, a not complete overlap was observed between the two experiments (Pearson correlation value of 0.69). However if we look at the comparison of all common DEGs (821), it is evident that the transcriptional profile was conserved between the two experiments (Pearson correlation value of 0.89), even if in the time course experiment the levels of up and down-regulation seemed to be more marked.

Gene list	Heatmap			Similarity Matrix Pearson correlation Value
All common genes		Log2FC_TC Log2FC_CUR	Log2 Fold Change -1.50 0.00 1.50	0.69
All common DEGs		Log2FC_TC Log2FC_CUR	Log2 Fold Change -3.00 0.00 3.00	0.89

Figure 4.33 *Heatmaps and correlation results of the data comparison between the log2 FC of the T28 BLM vs SAL time Course Study (TC) and the Curative protocol (CUR) study with nintedanib*

Another comparison was made on WGCNA results of the two transcriptomic experiments to understand if modules characterized by genes modulated and normalized by ninted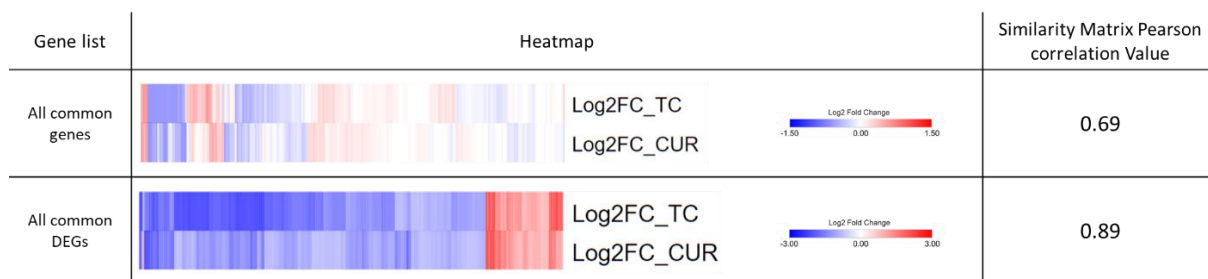anib were enriched in genes belonging to a specific temporal development profile of the fibrotic condition induced by BLM. The genes of the module 3 CUR (module characterized by genes affected by nintedanib and not modulated by BLM) did not have very strong and highly significant NES for any gene list obtained from the time course modules (**Figure 4.34**). Instead, the modules 2 and 1 CUR which were related respectively to the strong and mild effect of nintedanib, exhibit highly significant NES when compared with the list of gene with positive MM of the module 1 and 3 of the time course experiment (both modules with a marked de-regulation in the last 3 time points). Significant NES also emerged from the comparison with the ME8-related lists. Therefore, these results suggest that the most representative genes of the module 1 and 2 of the experiment with nintedanib were highly enriched with genes belonging to the module 1 and 3 of the time course.

A similar condition was also observed for ME4Cur, even if in this case the NES was slightly lower than in the previous example. Moreover, it is important to note that the NES were found to be consistent with the direction of the specific match from which they derive, therefore, for example, the ME1Cur (a module eigengene of the experiment with nintedanib, principally characterized by a down-regulation) produces positive NES when compared with ME1_posMM, a list of genes with

positive MM for the ME1 of the time course experiment (module eigengene principally characterized by down-regulation).
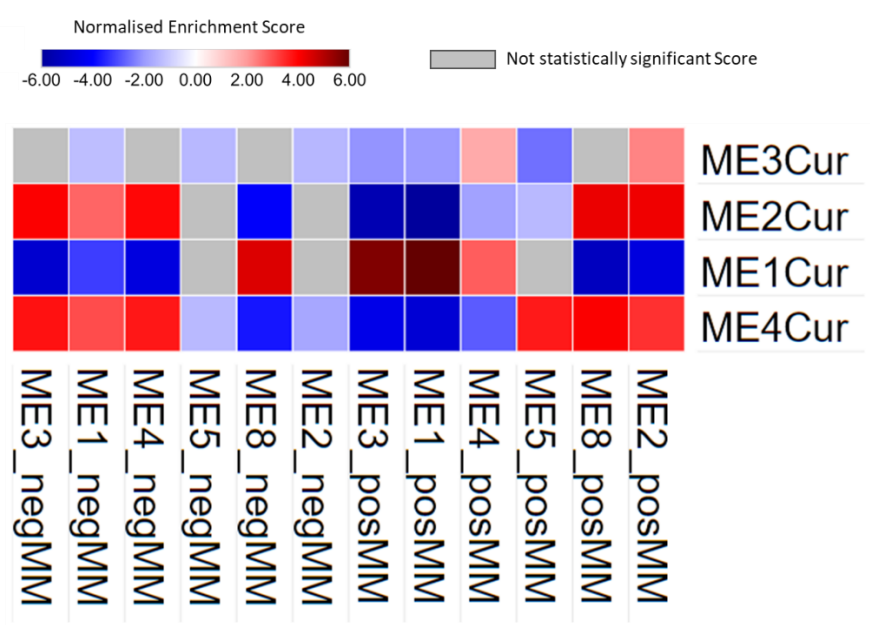

Figure 4.34 Heatmap of the WGCNA comparison performed using GSEA. NES derived from pre-ranked list (in rows) and gene lists obtained applying a cut-off of ≥ 0.8 and ≤ -0.8 on MM of genes of the time course experiment (name of the list is reported in column).

5. DISCUSSION AND CONCLUSION

5.1 The Rat Model of BLM-Induced Lung Fibrosis

Idiopathic pulmonary fibrosis is a chronic, debilitating and irreversible lung disease with a high clinical need, that includes the reduction of the diagnosis time and the amelioration of clinical management improving drug safety and efficacy[1]. To study a complex disease, such as IPF, basic research and the initial phases of the drug development process critically rely on the availability of a well characterized and optimized animal model. As largely explained in the introduction, the most used and best characterized and recommended model for preclinical testing of anti-IPF drugs is the murine intratracheal BLM model[3]. Among the models available today, the murine BLM model is low-cost, easy to perform, relatively reproducible and produces results in a short period of time, all advantages that overlook the relative disadvantages[4]. Moreover, this model was employed in the preclinical stages of drug development for pirfenidone and nintedanib, the only two drugs approved for IPF. For these reasons, in the Chiesi Farmaceutici laboratories several murine models of BLM-induced lung fibrosis had been developed and employed in projects related to the study of IPF.

In the model used in this study, pulmonary fibrosis was induced by a double administration of BLM. In literature are reported many studies that employ a series of repetitive multiple doses of BLM over time with, however, a consequent lengthening of the fibrotic stage and longer time investment[39]. For example, Peng and colleagues reported irreversible fibrotic features in the lungs of mice subjected to repetitive intratracheal administration of low dose of BLM for 24 weeks, but it involved a significant amount of time and had high management cost[54]. So the choice to adopt a double administration was dictated by the possibility to mimic the recurrent episodes of lung injury that occur in IPF and to reproduce the chronic aspect of the disease more effectively, without resorting to more complicated models with a longer time of fibrotic development. Indeed, a double administration of BLM produces a more robust and reproducible lung fibrosis with longer resolution times with respect to models that employ a single dose[78].

Although mouse is the most recommended model for preclinical testing in the context of lung fibrosis, the guidelines for the preclinical assessment of potential therapies for pulmonary fibrosis suggest to use rats if a second species is required[3]. In the laboratory where I performed my Ph.D. project, both mouse and rat models are typically used, especially in the target validation and identification phases. The availability of a second well characterized species is very important during the evaluation of an anti-fibrotic effect of a specific pharmacological treatment, to complement the understanding of mechanisms of action and to confirm the related outcome.

In the last years, the experiments conducted by Chiesi Farmaceutici demonstrated differences between the mouse and the rat model, especially in the appearance of histological lesions and in progression/resolution of the pulmonary fibrosis induced by BLM. However, while the development of lung fibrosis is highly studied in mice, also at the transcriptomic level, a complete characterization of the model developed in rat does not exist. So, there was a need to have a clear and broad picture of the rat model to understand its translational potential to the human IPF and to identify new therapeutic targets and biomarkers that clearly define the disease progression and resolution.

5.2   Time Course Study

The first experiment performed during my PhD project was a time course study of a BLM-induced lung fibrosis rat model. This experiment represented an important step to understand the key points of development, progression, consolidation and resolution of lung fibrosis induced by BLM. Furthermore, this experiment allowed to identify the best therapeutic window to test potential anti-fibrotic molecules, in order to detect a pharmacological effect in terms of pulmonary fibrosis reduction.

The BLM administration induced a significant weight loss in the first days of treatment. This outcome reflected the cytotoxic effect of BLM and allowed to assess the animal fitness and understand the extent of the damage caused by BLM during the whole experiment. The weight loss in animals is actually an indication of a stress and pain conditions and is considered as a parameter for severity assessment[79]. The highest weight reduction was reached on day 7, with an average weight loss of ≃16%, which indicates a quite severe BLM effect, considering that local authorities define a body-weight reduction of 20% or more, as a parameter of severe suffering that requires a human endpoint decision[79]. Despite the initial weight loss, after day 7 the BLM-treated rats tended to regain weight very quickly, up to day 32, where the daily weight increase was comparable to that of the control group. A weight loss induced by BLM in lung-fibrosis experiments is a well-known effect from literature[52,80] and in our experiment the effect could have been enhanced by the type of intratracheal administration of the BLM (see **paragraph 3.1.3** of Material and Methods for more details). Indeed, the intratracheal administration with an aerosol method could induce a higher general damaging effect on the lung, as demonstrated by Robbe and colleagues[81]. In their study, the authors compared two method of intratracheal administration of BLM, one performed by a flowing instillation and one by aerosolization with a microsprayer, and their reported a higher weight loss in animals treated with the aerosol method. Despite this possible collateral effect, the

intratracheal aerosolization method allows the development of a homogeneous fibrosis throughout the lung tissue, reducing sample-dependent variability and represent the best instillation method when compared to other intratracheal instillation[81,82].

Another sign of an evident severity of the model was highlighted by the high mortality rate recorded, an aspect that had a negative impact on the experiment, affecting the number of animals in treatment groups. The survival decrease was also observed in other experiments reported in literature with this model[54,80]. However, fluctuations in the survival rate and degree of severity of the model was already noted in several experiments of BLM-induced lung fibrosis performed by Chiesi Farmaceutici. In addition to the investigator-dependent variability, this could be related to specific properties of the BLM used in this first experiment, as mentioned in the **paragraph 4.4**. These aspects led to the selection of a more controlled and contaminant-free BLM for the second curative model experiment (see below).

To evaluate the potential systemic inflammatory effect induced by BLM, differential cell counts of WBC were measured in the blood. The WBC differential counts showed a doubling of the number of monocytes, neutrophils and eosinophils in rats treated with BLM compared to the control group on day 7, demonstrating the presence of a strong systemic inflammation in the BLM-treated animals that could be responsible of the weakness conditions of the animals in the first days. As confirmed by the histological analysis (**Figure 4.4**), the inflammation is also evident at lung level. A similar increase in all types of inflammatory cells was usually observed in the Broncho-alveolar lavage (BAL) fluid recovered from BLM treated animals, especially in the first days after the insult and the observation is also similar in different animal species[54,83,84].

Interestingly, the eosinophils levels remain higher in the animals treated with BLM in all the analysed time points. This type of cells have been shown to increase in tissues during many fibrotic conditions,

and has been evaluated as possible biomarker for fibrosis, but the relationship between this WBC population and fibrosis is still under evaluation[85,86].

5.2.1 Time-Dependent Histopathological and Hydroxyproline Content Changes

Morphological and molecular characterization of lung fibrosis is an important endpoint for preclinical assessment in a BLM-model of pulmonary fibrosis. The assessment of HYP content in lung homogenate is the fastest and easiest way to estimate collagen content, because HYP is one of the key components of this complex protein and it is estimated that each milligram of HYP is equivalent to 6.94 milligrams of collagen[3]. Indeed, HYP and proline have an important role in the 3D structure and stability of collagen, because they allow the sharp twisting of the collagen helix[87]. Given these considerations, the guidelines for the use of animal models in the study of lung fibrosis report that the measurement of HYP in lung homogenate represents the optimal primary endpoint for preclinical assessment of novel therapeutic agents[3]. In the time-course experiment, an elevated HYP concentration was observed in BLM-treated rats starting from day 7 with a steady upward trend over-time. However, the direct comparison between the HYP level of SAL and BLM groups was not statistically significant at day 7. Levels of HYP further increased at all the following time points, being the difference statistically significant between the two groups starting from day 14 and until day 28. Also in other time course studies of murine models of BLM-induced lung fibrosis, an increase in HYP concentration was reported, specially starting from time points subsequent to day 7[52,88]. The HYP data reflects the features observed in the histological analysis, in fact, 7 days after the first administration of BLM, the amount of extracellular matrix and collagen, marked by the green/blue colour, was visually lower than at the other time points and it was largely confused and hidden by the massive presence of inflammatory cells and haemorrhages. The HYP measure was important for the time course experiment, because it was the only parameter that evaluates the amount of collagen as component of the extracellular matrix. Indeed, the two histological analyses carried out

in this study were able to evaluate the area of the pulmonary parenchyma occupied by fibrosis, without discriminate against cellular hyperproliferation and alteration of alveolar/architectural structures (see **paragraph 3.2.4** to more details). Indeed, at T07, the highest values for Ashcroft score and % of lung fibrosis were registered, and this was principally related to the presence of wound healing associated to an active damage response as partially highlighted by the graph in **Figure 4.7**, showing the frequency of distribution of different type of damage. However, at day 14, when the wound healing process and inflammation were decreasing, the histological images displayed a less severe pathologic appearance and showed the beginning of the fibrotic process with production of components of the extracellular matrix, still maintaining the architectural structure of the lung. The fibrotic process continued in the following two time points leading to the formation of dense fibrotic agglomerates and initial alteration of the pulmonary structure. This framework clearly describes the classical development of the BLM model, as reported by other studies, that indicate a phase switch from inflammation to fibrosis around the seventh day post-BLM with fibrotic lesions appearance starting from day 14 and with a peak of response found at day 21-28 (**Figure 5.1 A**)[3,39,89]. In the present time course experiment, the lesion development seemed to be lightly shifted compared to that reported by the other studies. Based on data depicted in **Figure 5.1 B**, the fibrosis establishment could be across the T14 rather than the T7. These findings may be explained by the fact that the model used in this experiment employed a double administration of BLM.

In the time course experiment, fibrotic structures were detected until day 56 after the first BLM instillation, suggesting that in this model the fibrotic process induced by BLM needed more time to resolve, even if its area was decreasing. This highlights the possibility of identifying, in this specific time point, possible processes related to the natural resolution of the pathologic condition induced by BLM. Evidence in literature reports that generally the fibrosis resolves within 4–8 weeks, leading to almost complete regeneration of the lung structure[3,90,91]. As in this case, no signs of fibrotic

resolution were observed at day 56 in relevant time course study of BLM-induced lung fibrosis performed in mice and rats[52,54,55,81].
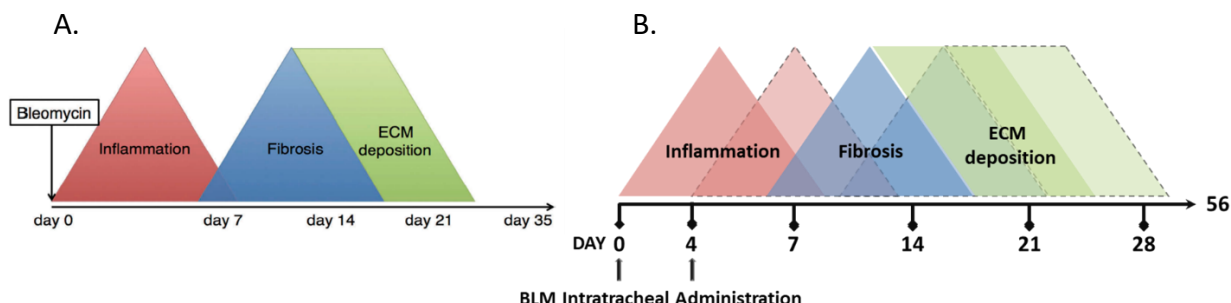
*Figure 5.1 A. Schematic image of BLM-induced pulmonary fibrosis reported by Yanagihara and colleagues **B.** A possible schematic representation of our model based on the scheme proposed by Yanagihara[39].*

5.2.2   Differential Gene Expression Analysis Highlights Diverse Time-Dependent Transcriptional Responses to BLM

The transcriptomic analysis performed on the time course experiment provided a very clear and detailed overview of the fibrotic development process of the rat model of BLM-induced pulmonary fibrosis and highlighted some interesting biological processes which deserve a deeper evaluation for the identification of new therapeutic targets and diagnostic biomarker for IPF. For confidentiality some of these results will not be showed in this thesis.

As in the Results **paragraph 4.3.1**, the PCA analysis showed that a profound transcriptomic profile alteration in response to BLM was already evident at T07. Indeed, at this time point, the maximum transcriptomic variation induced by BLM, respect to the control condition, was recorded. This effect could be related to the combination of the acute inflammatory response, wound healing activation and the initial onset of fibrosis, unique pathological condition of this specific time point, that also emerged from the other analyses already described. Among the most significant pathways/processes enriched within the list in up-regulated genes at T07 were the cell cycle, cell division and epithelial to mesenchymal transition (EMT). The activation of these pathways and

processes reflected the suffering state of the pulmonary epithelium. In fact, as explained in the introduction, BLM, through its mode of action, leads to the programmed death of the AEC type I and consequently to the exposure of basal lamina that, as physiological response, leads to the proliferation and differentiation of the AECs type II, to repair the damaged alveolar epithelium[4,24]. This repair process has been reported to be dysregulated also in the human disease, although it does not occur as rapidly as with BLM[23]. In fact, inflammation also emerged from the significantly up-regulated pathways at T07 (even if inflammatory pathways were not found among the Top 5 list reported in **Table 4.2**). Indeed, pathways like myeloid leukocyte activation, leukocyte chemotaxis, cytokine-cytokine receptor interaction and regulation of inflammatory response, were significantly enriched (Log FDR < -9). The pathways connected to the inflammation remained significatively enriched throughout the entire time course even if with lower statistical significance, while the pathways linked to the cell cycle lost the statistical significance in the later stages of the study.

The effect of haemorrhagic processes, observed at T07, emerged at the level of the significantly down-regulated pathways, together with other biological processes linked to the circulatory system. The transcriptomic effect was also described in other studies, where it was reported a first pronounced inflammatory phase, with a lot of differentially expressed genes related to inflammatory disease, immune response and wound healing, including various cytokines and chemokines[52,54]. Also genes associated with the cell cycle were reported to be altered in this preliminary phase of the model[54].

In correspondence of the T14, the minimum peak of DEGs was registered. Probably an explanation of this data could be ascribed to the reduction of the inflammatory process and the lack of extensive structures of fibrotic material and distortion of the lung structure, typical features of the subsequent time points. However, the pathways and processes significantly enriched of the up-regulated genes at this time point were similar to the previous one, but with a greater presence of processes linked

to the ECM, a sign that at this moment of the time course the ECM components and their biological management were more involved. Pathways mainly involved in the composition, organization and degradation of the ECM were also identified among the significantly up-regulated pathways in the following time points, until T56. The same thing was observed by Cabrera and colleagues[55] in their time course study of BLM-induced lung fibrosis in the mice, indeed after an intratracheal administration of BLM the authors reported a series of genes up-regulated for up to 8 weeks that belonged to ECM or extracellular region.

However, all these matrix-related pathways had very low values of Log FDR in the T21 and T28, but at T56 those values were much higher, a sign of a reduction in statistical significance and therefore of a possible beginning of resolution of the pathological condition, as highlighted by the histological analysis. Also Schiller and colleagues[90], in their proteomic system biology study performed on a BLM-induced lung fibrosis mouse model, reported evidences of resolution of tissue repair on ECM-related proteins within 8 weeks post-BLM treatment.

For the later phases of the time course (T21, T28, and T56), among the down-regulated pathways, we found many biological processes related to the actin cytoskeleton and its remodelling and organization. This could highlight the activity of fibroblasts and its related stress fibres, one of the principal cytoskeletal structures of this cell-type that allow the physical connection between fibroblast cell membrane and focal adhesions[92]. A dysregulation of the stress fibres and actin related proteins was reported to be involved in the fibrotic process especially in later phases of IPF, where there was already a huge deposition of the ECM. Indeed, after stimulation with TGF-β, fibroblasts altered their morphology and structure through the formation of protuberant actin stress fibres and modified focal adhesion complexes, process extremely necessary to provide the mechanical connection to the ECM[93].

Despite these time point-related considerations, we decided to obtain a more panoramic and complete view of our model to better understand the different pathological transcriptomic signatures of the lung that develop fibrosis. Gene screening methods based on network of correlation were increasingly being used in bioinformatics applications to identify candidate biomarkers or therapeutic targets[66], so we decided to use WGCNA to identify time-dependent transcriptional profiles which correlate with the histological parameters and the human disease, with the final goal to highlight extremely relevant genes to be analysed for activities of target and biomarker identification.

Among the most informative modules identified in the WGCNA, three of them had drawn our attention because they represented three clearly defined types of response to BLM: module 4, 1 and 8, respectively called "early", "late" and "long-lasting" response. Therefore, WGCNA allowed to obtain additional information that were only partially emerged by the DEGs analysis.

The M8, and so the "long-lasting" response, was certainly the most characteristic representation of the fibrotic condition, because it correlated with the histological parameters and contained the most common genes related to fibrotic disease, such as collagen type I alpha 1 chain (Col1a1), collagen type III alpha 1 chain (Col3a1), Osteopontin (alias Secreted PhosphoProtein 1, Spp1), Fibronectin 1 (Fn1) and nearly all matrix metalloproteases (MMPs). Moreover, the simultaneous presence of two temporally different gene signatures ("early response" and "late response"), highlighted the possibility of understanding something more about the mechanisms of development of the pathological condition. Indeed, the transition between the early and the late response represented an important shift point for the model, emerging also from the histological analysis, and it requires more in-depth work. Based on these observations, it is reasonable to hypothesize that, between the T14 and T21, the chain of events started from the direct damage of BLM reached

specific characteristics able to trigger a series of processes and mechanisms that characterize the large production and deposition of ECM components.

5.2.3 Comparison with Other Studies in The Context of Lung Fibrosis

To evaluate the strength and overall consistency of the transcriptome profiling performed on the time course study, we compared our data with those of the two time-course studies performed in other murine models of BLM-induced lung fibrosis as well as with available data on human IPF.

The data originated from the comparative analysis between our data and those obtained in other murine models of BLM-induced lung fibrosis showed a high grade of reproducibility of the effect induced by BLM. Indeed, even if these experiments were performed by different laboratories, applying different protocols and types of administration of BLM, the transcriptomic profiles induced by BLM were largely preserved.

Regarding the species employed for the model, the greatest degree of reproducibility of the data was obtained by comparing our study with a study performed in the rat, while more differences, especially on the down-regulated genes were observed during the comparison with the study performed in the mouse. Although the response of these two species to BLM were similar, this comparison confirmed that the differences between transcriptomic profile in rat and mouse model, could be relevant to evaluate the response to potential anti-fibrotic treatment during preclinical studies, and therefore require more in-depth analysis. The major difference between our model and the rat model of Bauer et al.[52] was enclosed in the down-regulated genes of the representative module of the "late response" (module 1), highlighting a possible uniqueness of our model, that could be linked to the double administration of BLM performed in our study instead of one as in the study performed by Bauer and colleagues[52].

An analogous comparison was performed using data obtained from 9 different gene expression studies performed on lung samples of IPF patients[69–77] (see **paragraph 3.3.4** of Materials and

Methods for more details), with the aim to identify any analogies at the transcriptomic level between our animal model and human pathology and so evaluate the translational potential of the murine model performed in this work. During the comparison analysis, a strong correlation pointed out in the up-regulated genes, demonstrating a good translational potential of our model. In detail, the M8 was significantly enriched in almost all the gene lists deriving from human studies. This information indicated that the genes involved in the long-lasting response of our model and significantly correlated with the histological data, appeared up-regulated in human IPF studies. The module 8 enclosed the most translationally relevant genes for the evaluation of a new pharmacological entities in IPF preclinical studies. Subsequently, the leading-edge analysis of GSEA, allowed to select within the M8 an even more restricted set of genes with very high translational potential (**Figure 4.15** and **Table 4.4**). This core set of translationally relevant genes was principally composed by elements that constitute the ECM, such as fibrillar collagens (collagen type 1 and 3), and genes that play a role in the plasma membrane and extracellular space. Moreover, it is important to note that these genes were highly connected each other by relations of co-expression, co-localization and genetic interactions. These genes were already widely known both in IPF and in fibrosis-related animal models. Cabrera and colleagues in their study reported that several genes encoding for ECM components (like collagen type 1 genes) and ECM remodelling enzymes, were significantly increased during the fibrotic response of their BLM model and these data were consistent with the histopathological scores[55]. It is also well known the role of Spp1 (Secreted Phosphoprotein 1, or Osteopontin) in restoration of tissues and angiogenesis, and for these reasons it was reported to be involved in many pulmonary diseases[94]. Grem1 (gremlin 1), a bone morphogenetic protein involved in tissue regeneration, was increased in IPF fibroblasts and lung biopsies compared to controls due to the TGF-β1-mediated activation of myofibroblasts[95]. Also

Thbs2 (thrombospondin 2), a glycoprotein involved in cell-cell and cell-matrix interactions, was identified as differentially expressed in the lung of IPF and fibrotic NSIP patients[96].

An important aim of this time course experiment, in addition to all the considerations on the various transcriptomic profiles and on the similarities between the model and the IPF, was to identify the best time window to attempt a curative approach to the pathological condition induced by BLM in our model. Pharmacological interventions before and during the inflammatory phase would act only at level of BLM-induced inflammation and could have a preventive effect on the establishment of lung fibrosis. Many drugs that have been proven to be effective with this protocol (defined "preventive protocol treatment") have failed in clinical trials[39]. So, many published papers in the context of BLM preclinical models suggested to investigate the effects of an antifibrotic agent in a protocol that consisted in administering drugs 7 days post-BLM and so at the beginning of the histological evidence of fibrosis and after the peak of the inflammatory phase ("curative protocol treatment")[3,39,97]. In our model, at T07, we registered a still high inflammatory response, as a consequence of the double administration of BLM, as mentioned before and schematized in **Figure 5.1 B.** However, at the same time, we found the first signals of fibrosis establishment, both at the morphological (histology and hydroxyproline) and transcriptional level (highlighted by high enrichment of the epithelial to mesenchymal transition process). So, we decided to start the treatment at this specific time point to interfere on a fibrotic process that is already active, even if there were still signs of inflammation. The end-point of the protocol was set at T28, because according to overall the obtained data, the fibrotic response appeared to be stable, with dense and compact fibrosis. Moreover, treatment for three weeks could allow a longer temporal window for a potential therapeutic treatment.

5.3   Dose Response Study of a Clinically Approved BLM

As mentioned earlier in the discussion, a moderate grade of variability in terms of severity of the model was registered throughout the several *in-vivo* BLM-related experiments conducted within the animal facility of Chiesi Farmaceutici. This variability may be partially related to specific properties of the batch of BLM used in each experiment. Indeed, we observed that different batches of BLM provided by Sigma-Aldrich (R&D use only) can differ, in terms activity (express in units/mg) and presence of endotoxin. Although there are no published studies that associate the inter-experiment variability to different batch of BLM, we investigated the different types of BLM reported in literature and we found that several experiments were performed with a clinically approved BLM[56,89]. So, in order to overcome the variability issues in the following studies, we started to use a BLM approved for clinical use, which is contaminant-free and extremely controlled within different batches. Given the positive and highly reproducible results reported by other Chiesi groups, starting from this study it was decided to switch to a clinically approved BLM. Therefore, before moving on to a curative experiment in order to test a pharmacological treatment, it was decided to perform a dose-response study of the new chosen BLM to evaluate its effect and select the correct dose to move forward with. The experiment highlighted a good dose-dependent effect for many analysed readouts, such as the body-weight trend, the lung histological analysis and lung hydroxyproline level. Otherwise, the % of fibrosis on total lung area didn't increase with the increasing of the dose but it showed very similar levels between of 0.5 and 1.0 U/Kg. Considering the data all together, the dose of 1.0 U/Kg was selected for subsequent studies, because it represented a good compromise between efficacy and toxicity. Indeed, the lung level of HYP and the fibrosis severity measured by histological analysis were sufficiently elevated to confirm that BLM 1.0 U/Kg was able to induce a sub-maximal fibrotic response with an acceptable tolerability and adequate to reveal a potential therapeutic effect of a drug in a curative protocol study.

5.4   Curative Protocol Study with Nintedanib

Once the definition of the correct therapeutic window for intervening with anti-fibrotic drugs was set and after the selection of the adequate dose and type of BLM, it was possible to proceed with a curative experiment using a known anti-fibrotic drug. This experiment was needed for the functional validation of the model and provided the bases to evaluate the whole transcriptomic effect of an anti-fibrotic drug on our rat model of BLM-induced lung fibrosis. Both the two anti-fibrotic treatment approved for IPF, pirfenidone and nintedanib, showed efficacy in different animal models, although the effect was only marginal as mentioned in the introduction of this thesis (**paragraphs 1.5.2** and **1.6.3**)[3,98].

During the curative experiment, the animals of the NINT group showed a faster weight recovery in the first week of treatment, which could be an evidence of a positive effect of the molecule. However, in the last week of treatment, the animals treated with nintedanib showed a trend of reduction of their body-weight recovery, compared to BLM group. The difference in the body weight trend between BLM and NINT group, could be related to the adverse effect of the drug at gastro-intestinal level, that was also observed in clinical trials[99], even if these data were not mentioned in preclinical validation studies for nintedanib[100]. The mean lung/body ratio measured in this experiment was significantly increased in BLM group compared to control group, this aspect was reported by other studies[100–102] and might be related to the massive matrix deposition[102]. In the NINT group a trend towards the reduction of this ratio was evident, even if not statistically significant. A similar effect was reported by Surber and colleagues[100] in a curative BLM protocol with nintedanib administered by different types of administration routes: oral and inhaled. This effect could be associated to a reduction of ECM deposition induced by BLM and related to the anti-fibrotic effect of the molecule. Moreover, the lung/body ratio trend observed with nintedanib treatment was supported by the histological analysis, that highlighted a trend in reducing the

percentage and the severity of the fibrotic lesions after the treatment with nintedanib. However, as expected, the treatment failed to completely revert the fibrotic process limiting to a partial effect as observed in clinical treatment. Indeed, as I mentioned in the "Introduction", this drug is able to slow down the progression of IPF, improving some functional respiratory parameters of the lung[1,2] without resolve the disease, moreover the efficacy reported in different lung fibrosis animal model was limited[3], as evidenced by Wollin and colleagues[102] that reported a partial reduction in a series of fibrotic parameters exerted by nintedanib on different mouse model of pulmonary fibrosis.

Finally, the reduction of the amount of some types of WBC in blood, induced by nintedanib, highlighted a possible systemic anti-inflammatory effect of the molecule. Even if inflammatory cells count was not previously measured in the blood of experimental animals treated with nintedanib, an inflammatory effect of this drug was largely described[96] in literature, especially through the evaluation of the amount of lymphocytes and neutrophils in the BAL fluid[102].

5.4.1 Whole Transcriptomic Effect of an Anti-Fibrotic Drug on The Developed BLM-Induced Lung Fibrosis Rat Model

The transcriptomic effect of nintedanib on animal models of lung fibrosis has never been investigated. Gene expression changes induced by nintedanib treatment were investigated, until now, only in human cells derived from IPF patients through the employment of next-gen technology and bioinformatic tools[103]. Therefore, it didn't provide an overall view of the nintedanib effect on multiple cell types together.

The PCA analysis performed on RNAseq data highlighted a clear separation of the different groups of treatment, even if a high variability within the BLM group was evident. Otherwise, the profile of the NINT group showed more uniform data and less variability.

The transcriptomic profile associated to nintedanib administration revealed a reduction in the number of significant DEGs (NINT vs SAL), compared to BLM treatment alone (BLM vs SAL). Indeed,

among the total DEGs identified in the BLM vs SAL comparison, 859 genes (172 up and 657 down) were no longer significantly de-regulated in the NINT vs SAL comparison, as showed in **Figure 4.28**. The WGCNA applied to the gene expression dataset derived from the curative treatment of nintedanib allowed to better appreciate the key set of genes and related pathways associated with the nintedanib effect. Indeed, this analysis identified two clusters of genes (M1 and M2) characterized by a de-regulation induced by BLM that was partially or totally restored to the levels of control groups by nintedanib and they were correlated with the histological parameters. In detail, the M2 (characterized by a strong effect of nintedanib treatment on gene mainly up-regulated by the effect of BLM) was enriched in genes belonging to the cellular respiration and mitochondria-related processes. This suggested that the major effect of nintedanib was related to genes involved in these distinctive mechanisms, which were also commonly dysregulated in human IPF. Indeed, pathologic metabolic reprograming and mitochondrial dysfunction were reported in IPF. As a consequence, they affect the efficiency of electron transport chain, which results in an increased production of reactive oxygen species (ROS), that lead to apoptosis and senescence with a subsequent activation of fibrotic responses[104,105]. The antioxidant effect of nintedanib was demonstrated both *in-vivo* and *in-vitro*, indeed this molecule is able to decrease the levels of ROS, although the mechanism by which it produces this effect has not yet been fully explained[106]. Pathways related to the cellular respiration and up-regulated by the effect of BLM, was not emerged from the analysis of the time course study, perhaps because they were masked by the overabundance of up-regulated genes linked to the ECM and its remodelling.

The other cluster of genes on which nintedanib showed an effect, albeit partial, was the M1 (characterized by a mild effect of nintedanib treatment on gene principally down-regulated by the effect of BLM) enriched of gene belonging to various pathways and processes. Among them, I would mention the cellular protein catabolic process, a gene ontology term that included pathways

resulting in the breakdown proteins. As reported by Emblom-Callahan and colleagues[107], within data derived from IPF fibroblasts there was a significant deregulation on catabolic processes that resulted in an abnormal "degradome".

The genes of this pathway, according to the ME1, were mainly down-regulated by the effect of BLM, and we supposed that this effect could be related to the lack of matrix protein turnover typical of fibrotic processes[24]. This down-regulation was partially reduced after treatment with nintedanib and we could therefore assume that the positive effect of nintedanib influenced, albeit in a slight way, the processes of protein catabolism bringing it back to a partial control condition. Not surprisingly this module correlated with the histological parameters. Indeed, the histological analysis showed that the ECM deposition in the NINT group appeared less thickened and dense than the BLM group.

Despite the positive effect exerted by nintedanib on the BLM-altered lung transcriptome, the M3 showed a possible undesirable or not related to the anti-fibrotic effect and which could be partially responsible for the failure of resolving the fibrotic process. This cluster of genes presented a profile mainly focused toward a down-regulation in the NINT vs SAL comparison, without any modification in BLM vs SAL. M3 was enriched in genes related to the morphogenesis of an epithelium, probably caused by the attenuation of the major growth factor[108]. Indeed, as explained by Warburton and colleagues[109] in their review about the roles of growth factor signalling in lung morphogenesis, the Epidermal Growth Factor (EGF), Fibroblast Growth Factor (FGF), Hepatocyte Growth Factor (HGF) and Platelet-Derived Growth Factor (PDGF) through their transmembrane tyrosine kinase receptors exert a positive effect on lung morphogenesis. In our opinion, a down-regulation of this pathway could negatively affect the restoration of the damaged epithelium, a process that obviously was not activated by the pathological condition induced by BLM.

5.4.2   Comparison Between the Two Transcriptomic Analysis

Considering the BLM dose reduction from the time course study to the curative experiment with nintedanib, it was expected to note a general reduction of the fold change levels in the experiment with nintedanib (BLM vs SAL) at T28.

The comparison between the WGCNA results performed in these two experiments was essential to understand if modules characterized by genes modulated and normalized by nintedanib were related to a specific temporal development profile of the fibrotic condition induced by BLM. From this analysis emerged that the modules which highlighted a curative effect of nintedanib were principally enriched in genes belonging to a late response profile (M1: marked down-regulation only in the last three time points and M3: marked down-regulation in all the time points which became more prominent in the latest three). This suggested that nintedanib probably had a more marked effect on the late-response of the BLM model and therefore it less affected the most translationally relevant BLM-response (M8: marked up-regulation in all the analysed time point).

All these observations from our model suggest that to obtain an anti-fibrotic effect and at the same time revert the fibrotic process (and therefore to act better than nintedanib) it is necessary to identify a molecule capable of acting on oxidative stress, matrix turnover and also affecting the core genes of the long-lasting response of the BLM-model, which were found to be the genes with the highest translational potential with human disease.

5.5   Conclusion and Next Steps

The multilevel analysis performed on the time course study showed that, in this BLM-induced lung fibrosis rat model, the animals developed a pathological condition that appeared to be more stable and consistent between 21 and 28 days post-BLM, where the initial acute inflammatory reaction left the place to fibrotic response and deposition of the ECM components. Moreover, 56 days after the BLM induction, a series of evidences of resolution of the fibrotic process began to arise. All these aspects of the BLM model were extensively validated by the data available in the literature, confirming the strength of our model.

The model developed and perfected in this study, after the selection of the correct therapeutic window to be used in the test of pharmacological agents, was proved to be responsive to the anti-fibrotic effect induced by nintedanib, one of the two drugs approved for the treatment of IPF providing a further functional validation of our model. Indeed, the lung histological analysis highlighted a trend in reducing the percentage and the severity of the fibrotic lesions after treatment with nintedanib, even if it failed to completely revert the fibrotic process, as reported in the literature both at clinical and preclinical level. The rat model described in these studies proved to have a pharmacological intervention window of 3 weeks, unlike the mouse model employed during drug discovery studies in Chiesi Farmaceutici laboratories[110], and some published therapeutic studies[108,111,112], that are characterized by a therapeutic window of only 2 weeks due to an earlier resolution of fibrosis. Therefore, this rat model is suited to test various types of therapeutic molecules, even those that require a longer period to perform their therapeutic effect.

From the transcriptomic analysis emerged that, in our model, genes followed specific signatures over time revealing the presence of three important biological response to BLM, which could be simplified in: early response, late response and long-lasting response.

The long-lasting response included genes with a high translational potential with human IPF, given its strong correlation with histological parameters and with data obtained from studies made on human IPF samples. The genes belonging to this type of response, given their characteristics, will be investigated to select a series of candidate biomarkers with translational value, that could be useful for evaluating the therapeutic effect of new pharmacological treatments through the employment of rapid biomolecular techniques, like for example the RT^2 PCR Array.

The genes and pathways belonging to the early and late responses will be investigated to identify new therapeutic targets, because on the basis of the obtained data, it was reasonable to hypothesize that, between the early and the late response something happened that could be important for understanding the pathogenesis of the fibrotic process and so provided interesting key points to be modulated to reduce or eliminate the development of lung fibrosis.

The transcriptomic analysis performed on the curative protocol study with nintedanib identified clusters of genes whose expression was partially or totally restored to the levels of control groups by the treatment and sets of genes on which this anti-fibrotic drug did not show an effect on the resolution of the pathological condition induced by BLM. This analysis allowed to understand which parts of the broad-spectrum effect of nintedanib were beneficial in resolving the fibrotic process developed in our model, in order to test new pharmacological entities proposed for the treatment of IPF.

6. <u>REFERENCES</u>

(1)   Spagnolo, P.; Tzouvelekis, A.; Bonella, F. The Management of Patients With Idiopathic Pulmonary Fibrosis. *Front Med (Lausanne)* **2018**, *5*, 148. https://doi.org/10.3389/fmed.2018.00148.

(2)   Saito, S.; Alkhatib, A.; Kolls, J. K.; Kondoh, Y.; Lasky, J. A. Pharmacotherapy and Adjunctive Treatment for Idiopathic Pulmonary Fibrosis (IPF). *J Thorac Dis* **2019**, *11* (Suppl 14), S1740–S1754. https://doi.org/10.21037/jtd.2019.04.62.

(3)   Jenkins, R. G.; Moore, B. B.; Chambers, R. C.; Eickelberg, O.; Königshoff, M.; Kolb, M.; Laurent, G. J.; Nanthakumar, C. B.; Olman, M. A.; Pardo, A.; et al. An Official American Thoracic Society Workshop Report: Use of Animal Models for the Preclinical Assessment of Potential Therapies for Pulmonary Fibrosis. *Am J Respir Cell Mol Biol* **2017**, *56* (5), 667–679. https://doi.org/10.1165/rcmb.2017-0096ST.

(4)   Tashiro, J.; Rubio, G. A.; Limper, A. H.; Williams, K.; Elliot, S. J.; Ninou, I.; Aidinis, V.; Tzouvelekis, A.; Glassberg, M. K. Exploring Animal Models That Resemble Idiopathic Pulmonary Fibrosis. *Front Med (Lausanne)* **2017**, *4*, 118. https://doi.org/10.3389/fmed.2017.00118.

(5)   King, T. E. Clinical Advances in the Diagnosis and Therapy of the Interstitial Lung Diseases. *Am J Respir Crit Care Med* **2005**, *172* (3), 268–279. https://doi.org/10.1164/rccm.200503-483OE.

(6)   Mikolasch, T. A.; Garthwaite, H. S.; Porter, J. C. Update in Diagnosis and Management of Interstitial Lung Disease . *Clin Med (Lond)* **2017**, *17* (2), 146–153. https://doi.org/10.7861/clinmedicine.17-2-146.

(7)   Idiopathic Pulmonary Fibrosis: Diagnosis and Treatment: International Consensus Statement. *Am J Respir Crit Care Med* **2000**, *161* (2), 646–664. https://doi.org/10.1164/ajrccm.161.2.ats3-00.

(8)   Travis, W. D.; Costabel, U.; Hansell, D. M.; King, T. E.; Lynch, D. A.; Nicholson, A. G.; Ryerson, C. J.; Ryu, J. H.; Selman, M.; Wells, A. U.; et al. An Official American Thoracic Society/European Respiratory Society Statement: Update of the International Multidisciplinary Classification of the Idiopathic Interstitial Pneumonias. *Am J Respir Crit Care Med* **2013**, *188* (6), 733–748. https://doi.org/10.1164/rccm.201308-1483ST.

(9)   Agusti, C. American Thoracic Society/European Respiratory Society International Multidisciplinary Consensus Classification of the Idiopathic Interstitial Pneumonias (Vol 165, Pg 277, 2002). *Am J Respir Crit Care Med* **2002**, *166* (3), 426.

(10)   Smith, M.; Dalurzo, M.; Panse, P.; Parish, J.; Leslie, K. Usual Interstitial Pneumonia-Pattern Fibrosis in Surgical Lung Biopsies. Clinical, Radiological and Histopathological Clues to Aetiology. *J Clin Pathol* **2013**, *66* (10), 896–903. https://doi.org/10.1136/jclinpath-2013-201442.

(11)   Jeffrey L. Myers. Histopathology of IPF and Related Disorders. In *Idiopathic Pulmonary Fibrosis: A Comprehensive Clinical Guide*; Sharon I.S. Rounds, Keith C._Meyer, Steven _D. Nathan, Eds.; Respiratory Medicine; HUMANA PRESS, 2014. https://doi.org/10.1007/978-1-62703-682-5.

(12)   Lynch, J. P.; Huynh, R. H.; Fishbein, M. C.; Saggar, R.; Belperio, J. A.; Weigt, S. S. Idiopathic Pulmonary Fibrosis: Epidemiology, Clinical Features, Prognosis, and Management. *Semin Respir Crit Care Med* **2016**, No. 3, 331–357. https://doi.org/10.1055/s-0036-1582011.

(13)   Raghu, G.; Collard, H. R.; Egan, J. J.; Martinez, F. J.; Behr, J.; Brown, K. K.; Colby, T. V.; Cordier, J.-F.; Flaherty, K. R.; Lasky, J. A.; et al. An Official ATS/ERS/JRS/ALAT Statement: Idiopathic Pulmonary Fibrosis: Evidence-Based Guidelines for Diagnosis and Management. *Am J Respir Crit Care Med* **2011**, *183* (6), 788–824. https://doi.org/10.1164/rccm.2009-040GL.

(14)   Raghu, G.; Brown, K. K.; Bradford, W. Z.; Starko, K.; Noble, P. W.; Schwartz, D. A.; King, T. E.

J. A Placebo-Controlled Trial of Interferon Gamma-1b in Patients with Idiopathic Pulmonary Fibrosis. *N Engl J Med* **2004**, *350* (2), 125–133. https://doi.org/10.1056/NEJMoa030511.

(15)   Richeldi, L.; Costabel, U.; Selman, M.; Kim, D. S.; Hansell, D. M.; Nicholson, A. G.; Brown, K. K.; Flaherty, K. R.; Noble, P. W.; Raghu, G.; et al. Efficacy of a Tyrosine Kinase Inhibitor in Idiopathic Pulmonary Fibrosis. *N Engl J Med* **2011**, *365* (12), 1079–1087. https://doi.org/10.1056/NEJMoa1103690.

(16)   Olga Tourin, J. J. S. Idiopathic Pulmonary Fibrosis: The Epidemiology and Natural History of Disease. In *Idiopathic Pumnoary Fibrosis: A Comprehensive Clinical Guide*; Sharon I.S. Rounds, Keith C._Meyer, Steven_D. Nathan, Eds.; Respiratory Medicine; HUMANA PRESS, 2014. https://doi.org/10.1007/978-1-62703-682-5.

(17)   Zaman, T.; Lee, J. Risk Factors for the Development of Idiopathic Pulmonary Fibrosis: A Review. *Curr Pulmonol Rep* **2018**, *7* (4), 118–125. https://doi.org/10.1007/s13665-018-0210-7.

(18)   Sonye K. Danoff and Cheilonda Johnson. The Genetics of Pulmonary Fibrosis. In *Idiopathic Pulmonary Fibrosis: A Comprehensive Clinical Guide*; Sharon I.S. Rounds, Keith C. Meyer, Steven D. Nathan., Eds.; HUMANA PRESS, 2014; pp 207–220. https://doi.org/10.1007/978-1-62703-682-5.

(19)   Barratt, S. L.; Creamer, A.; Hayton, C.; Chaudhuri, N. Idiopathic Pulmonary Fibrosis (IPF): An Overview. *J Clin Med* **2018**, *7* (8). https://doi.org/10.3390/jcm7080201.

(20)   Coultas, D. B.; Zumwalt, R. E.; Black, W. C.; Sobonya, R. E. The Epidemiology of Interstitial Lung Diseases. *Am J Respir Crit Care Med* **1994**, *150* (4), 967–972. https://doi.org/10.1164/ajrccm.150.4.7921471.

(21)   Raghu, G.; Weycker, D.; Edelsberg, J.; Bradford, W. Z.; Oster, G. Incidence and Prevalence of Idiopathic Pulmonary Fibrosis. *Am J Respir Crit Care Med* **2006**, *174* (7), 810–816. https://doi.org/10.1164/rccm.200602-163OC.

(22)   Strongman, H.; Kausar, I.; Maher, T. Incidence, Prevalence, and Survival of Patients with Idiopathic Pulmonary Fibrosis in the UK. *Adv Ther* **2018**, *35* (5), 724–736. https://doi.org/10.1007/s12325-018-0693-1.

(23)   Nathan Sandbo. Mechanisms of Fibrosis in IPF. In *Idiopathic Pulmonary Fibrsosis: A Comprehensive Clinical Guide*; Sharon I.S. Rounds, K. C. _Meye. and S. N., Ed.; Respiratory Medicine; HUMANA PRESS, 2014. https://doi.org/10.1007/978-1-62703-682-5.

(24)   Geiser, T. Idiopathic Pulmonary Fibrosis--a Disorder of Alveolar Wound Repair? *Swiss Med Wkly* **2003**, *133* (29–30), 405–411. https://doi.org/2003/29/SMW-09986.

(25)   Wolters, P. J.; Blackwell, T. S.; Eickelberg, O.; Loyd, J. E.; Kaminski, N.; Jenkins, G.; Maher, T. M.; Molina-Molina, M.; Noble, P. W.; Raghu, G.; et al. Time for a Change: Is Idiopathic Pulmonary Fibrosis Still Idiopathic and Only Fibrotic? *Lancet Respir Med* **2018**, *6* (2), 154–160. https://doi.org/10.1016/S2213-2600(18)30007-9.

(26)   The Editors of Encyclopaedia Britannica. Fibroblast. **2018**.

(27)   Kendall, R. Fibroblasts in Fibrosis: Novel Roles and Mediators. *Front Pharmacol* **2014**, *5*, 1–13. https://doi.org/10.3389/fphar.2014.00123.

(28)   Hinz, B.; Phan, S. H.; Thannickal, V. J.; Galli, A.; Bochaton-Piallat, M.-L.; Gabbiani, G. The Myofibroblast: One Function, Multiple Origins. *Am J Pathol* **2007**, *170* (6), 1807–1816. https://doi.org/10.2353/ajpath.2007.070112.

(29)   Yamaguchi Miki; Hirai Sachie; Tanaka Yusuke; Sumi Toshiyuki; Miyajima Masahiro; Mishina Taijiro; Yamada Gen; Otsuka Mitsuo; Hasegawa Tadashi; Kojima Takashi; et al. Fibroblastic Foci, Covered with Alveolar Epithelia Exhibiting Epithelial–Mesenchymal Transition, Destroy Alveolar Septa by Disrupting Blood Flow in Idiopathic Pulmonary Fibrosis. *Lab Invest* **2017**, *97* (3), 232–242. https://doi.org/10.1038/labinvest.2016.135.

(30) Martinez, F. J.; Collard, H. R.; Pardo, A.; Raghu, G.; Richeldi, L.; Selman, M.; Swigris, J. J.; Taniguchi, H.; Wells, A. U. Idiopathic Pulmonary Fibrosis. *Nat Rev Dis Primers* **2017**, *3*, 17074. https://doi.org/10.1038/nrdp.2017.74.

(31) Thannickal, V. J.; Henke, C. A.; Horowitz, J. C.; Noble, P. W.; Roman, J.; Sime, P. J.; Zhou, Y.; Wells, R. G.; White, E. S.; Tschumperlin, D. J. Matrix Biology of Idiopathic Pulmonary Fibrosis: A Workshop Report of the National Heart, Lung, and Blood Institute. *Am J Pathol* **2014**, *184* (6), 1643–1651. https://doi.org/10.1016/j.ajpath.2014.02.003.

(32) Heukels; Moor; von der Thüsen; Wijsenbeek; Kool. Inflammation and Immunity in IPF Pathogenesis and Treatment. *Respir Med* **2019**, *147*, 79–91. https://doi.org/10.1016/j.rmed.2018.12.015.

(33) Wuyts, W. A.; Agostini, C.; Antoniou, K. M.; Bouros, D.; Chambers, R. C.; Cottin, V.; Egan, J. J.; Lambrecht, B. N.; Lories, R.; Parfrey, H.; et al. The Pathogenesis of Pulmonary Fibrosis: A Moving Target. *Eur Respir J* **2013**, *41* (5), 1207–1218. https://doi.org/10.1183/09031936.00073012.

(34) Bringardner, B. D.; Baran, C. P.; Eubank, T. D.; Marsh, C. B. The Role of Inflammation in the Pathogenesis of Idiopathic Pulmonary Fibrosis. *Antioxid Redox Signal* **2008**, *10* (2), 287–302. https://doi.org/10.1089/ars.2007.1897.

(35) Datta, A.; Scotton, C. J.; Chambers, R. C. Novel Therapeutic Approaches for Pulmonary Fibrosis. *British Journal of Pharmacology* **2011**, *163* (1), 141–172. https://doi.org/10.1111/j.1476-5381.2011.01247.x.

(36) Izumi, S.; Iikura, M.; Hirano, S. Prednisone, Azathioprine, and N-Acetylcysteine for Pulmonary Fibrosis. *N Engl J Med* **2012**, *367* (9), 870–871. https://doi.org/10.1056/NEJMc1207471.

(37) Raghu G; Rochwerg B; et al. An Official ATS/ERS/JRS/ALAT Clinical Practice Guideline: Treatment of Idiopathic Pulmonary Fibrosis. An Update of the 2011 Clinical Practice Guideline. *Am J Respir Crit Care Med* **2015**, *192* (2), E3–E19. https://doi.org/10.1164/rccm.201506-1063ST.

(38) Grimminger Friedrich; Schermuly Ralph T.; Ghofrani Hossein A. Targeting Non-Malignant Disorders with Tyrosine Kinase Inhibitors. *Nature Reviews Drug Discovery* **2010**, *9* (12), 956–970. https://doi.org/10.1038/nrd3297.

(39) Yanagihara, T.; Chong, S. G.; Vierhout, M.; Hirota, J. A.; Ask, K.; Kolb, M. Current Models of Pulmonary Fibrosis for Future Drug Discovery Efforts. *Expert Opin Drug Discov* **2020**, *15* (8), 931–941. https://doi.org/10.1080/17460441.2020.1755252.

(40) Chen Ya-Wen; Huang Sarah Xuelian; de Carvalho Ana Luisa Rodrigues Toste; Ho Siu-Hong; Islam Mohammad Naimul; Volpi Stefano; Notarangelo Luigi D.; Ciancanelli Michael; Casanova Jean-Laurent; Bhattacharya Jahar; et al. A Three-Dimensional Model of Human Lung Development and Disease from Pluripotent Stem Cells. *Nature cell biology* **2017**, *19* (5), 542–549. https://doi.org/10.1038/ncb3510.

(41) Sundarakrishnan; Chen; Black; Aldridge; Kaplan. Engineered Cell and Tissue Models of Pulmonary Fibrosis. *Adv Drug Deliv Rev* **2018**, *129*, 78–94. https://doi.org/10.1016/j.addr.2017.12.013.

(42) Vandamme. Rodent Models for Human Diseases. *Eur J Pharmacol* **2015**, *759*, 84–89. https://doi.org/10.1016/j.ejphar.2015.03.046.

(43) Iannaccone, P. M.; Jacob, H. J. Rats! *Dis Model Mech* **2009**, *2* (5–6), 206–210. https://doi.org/10.1242/dmm.002733.

(44) Degryse, A. L.; Lawson, W. E. Progress Toward Improving Animal Models for Idiopathic Pulmonary Fibrosis. *Am J Med Sci* **2011**, *341* (6), 444–449. https://doi.org/10.1097/MAJ.0b013e31821aa000.

(45) Murray, L. A. Targeting IL-13 with Tralokinumab Attenuates Lung Fibrosis and Epithelial

Damage in a Humanized SCID IPF Model. *Am J Respir Cell Mol Biol* **prepub**. https://doi.org/10.1165/rcmb.2013-0342OC.

(46) Naikawadi, R. P.; Disayabutr, S.; Mallavia, B.; Donne, M. L.; Green, G.; La, J. L.; Rock, J. R.; Looney, M. R.; Wolters, P. J. Telomere Dysfunction in Alveolar Epithelial Cells Causes Lung Remodeling and Fibrosis. *JCI Insight* **2016**, *1* (14), E86704. https://doi.org/10.1172/jci.insight.86704.

(47) Williamson, J. D.; Sadofsky, L. R.; Hart, S. P. The Pathogenesis of Bleomycin-Induced Lung Injury in Animals and Its Applicability to Human Idiopathic Pulmonary Fibrosis. *Experimental Lung Research* **2015**, *41* (2), 57–73. https://doi.org/10.3109/01902148.2014.979516.

(48) B Moore, B.; Lawson, W. E.; Oury, T. D.; Sisson, T. H.; Raghavendran, K.; Hogaboam, C. M. Animal Models of Fibrotic Lung Disease. *Am J Respir Cell Mol Biol* **2013**, *49* (2), 167–179. https://doi.org/10.1165/rcmb.2013-0094TR.

(49) Casamassimi, A.; Federico, A.; Rienzo, M.; Esposito, S.; Ciccodicola, A. Transcriptome Profiling in Human Diseases: New Advances and Perspectives. *Int J Mol Sci* **2017**, *18* (8). https://doi.org/10.3390/ijms18081652.

(50) Vukmirovic, M.; Kaminski, N. Impact of Transcriptomics on Our Understanding of Pulmonary Fibrosis. *Front Med (Lausanne)* **2018**, *5*, 87. https://doi.org/10.3389/fmed.2018.00087.

(51) Park, H.-J.; Yang, M.-J.; Oh, J.-H.; Yang, Y.-S.; Kwon, M.-S.; Song, C. W.; Yoon, S. Genome-Wide Transcriptional Response during the Development of Bleomycin-Induced Pulmonary Fibrosis in Sprague-Dawley Rats. *Toxicol Res* **2010**, *26* (2), 137–147. https://doi.org/10.5487/TR.2010.26.2.137.

(52) Bauer, Y.; Tedrow, J.; de Bernard, S.; Birker-Robaczewska, M.; Gibson, K. F.; Guardela, B. J.; Hess, P.; Klenk, A.; Lindell, K. O.; Poirey, S.; et al. A Novel Genomic Signature with Translational Significance for Human Idiopathic Pulmonary Fibrosis. *Am J Respir Cell Mol Biol* **2015**, *52* (2), 217–231. https://doi.org/10.1165/rcmb.2013-0310OC.

(53) Shichino, S.; Ueha, S.; Hashimoto, S.; Otsuji, M.; Abe, J.; Tsukui, T.; Deshimaru, S.; Nakajima, T.; Kosugi-Kanaya, M.; Shand, F. H.; et al. Transcriptome Network Analysis Identifies Protective Role of the LXR/SREBP-1c Axis in Murine Pulmonary Fibrosis. *JCI Insight* **2019**, *4* (1). https://doi.org/10.1172/jci.insight.122163.

(54) Peng, R. Bleomycin Induces Molecular Changes Directly Relevant to Idiopathic Pulmonary Fibrosis: A Model for "Active" Disease. *PLoS One* **2013**, *8* (4), 178–192. https://doi.org/10.1371/JOURNAL.PONE.0059348.

(55) Cabrera, S.; Selman, M.; Lonzano-Bolaños, A.; Konishi, K.; Richards, T. J.; Kaminski, N.; Pardo, A. *Gene Expression Profiles Reveal Molecular Mechanisms Involved in the Progression and Resolution of Bleomycin-Induced Lung Fibrosis*; edsbas; 2013.

(56) Kaminski, N.; Allard, J. D.; Pittet, J. F.; Zuo, F.; Griffiths, M. J.; Morris, D.; Huang, X.; Sheppard, D.; Heller, R. A. Global Analysis of Gene Expression in Pulmonary Fibrosis Reveals Distinct Programs Regulating Lung Inflammation and Fibrosis. *Proc Natl Acad Sci U S A* **2000**, *97* (4), 1778–1783. https://doi.org/10.1073/pnas.97.4.1778.

(57) Nawata, S.; Abolhoda, A.; Ross, H. M.; Brooks, A.; Burt, M. E. Sequential Bilateral Isolated Lung Perfusion in the Rat: An Experimental Model. *Ann Thorac Surg* **1997**, *63* (3), 796–799. https://doi.org/10.1016/S0003-4975(96)01372-0.

(58) Pontis S., B. F. Automated Histological Image Analysis for the Assessment of Bleomycin-Induced Pulmonary Fibrosis in Rodents; European Respiratory Journal : Madrid, 2019. https://doi.org/10.1183/13993003.congress-2019.PA2420.

(59) Ashcroft, T.; Simpson, J. M.; Timbrell, V. Simple Method of Estimating Severity of Pulmonary Fibrosis on a Numerical Scale. *J Clin Pathol* **1988**, *41* (4), 467–470. https://doi.org/10.1136/jcp.41.4.467.

(60) Hübner, R.-H.; Gitter, W.; Eddine El Mokhtari, N.; Mathiak, M.; Both, M.; Bolte, H.; Freitag-Wolf, S.; Bewig, B. Standardized Quantification of Pulmonary Fibrosis in Histological Samples. *Biotechniques* **2008**, *44* (4), 507–517. https://doi.org/10.2144/000112729.

(61) Jolliffe, I. T.; Cadima, J. Principal Component Analysis: A Review and Recent Developments. *Philos Trans A Math Phys Eng Sci* **2016**, *374* (2065), 20150202. https://doi.org/10.1098/rsta.2015.0202.

(62) Metsalu, T.; Vilo, J. ClustVis: A Web Tool for Visualizing Clustering of Multivariate Data Using Principal Component Analysis and Heatmap. *Nucleic Acids Res* **2015**, *43* (W1), W566–W570. https://doi.org/10.1093/nar/gkv468.

(63) Warde-Farley, D.; Donaldson, S. L.; Comes, O.; Zuberi, K.; Badrawi, R.; Chao, P.; Franz, M.; Grouios, C.; Kazi, F.; Lopes, C. T.; et al. The GeneMANIA Prediction Server: Biological Network Integration for Gene Prioritization and Predicting Gene Function. *Nucleic Acids Res* **2010**, *38* (Web Server issue), W214–W220. https://doi.org/10.1093/nar/gkq537.

(64) Shannon, P.; Markiel, A.; Ozier, O.; Baliga, N. S.; Wang, J. T.; Ramage, D.; Amin, N.; Schwikowski, B.; Ideker, T. Cytoscape: A Software Environment for Integrated Models of Biomolecular Interaction Networks. *Genome Res* **2003**, *13* (11), 2498–2504. https://doi.org/10.1101/gr.1239303.

(65) Zhou Yingyao; Zhou Bin; Pache Lars; Chang Max; Khodabakhshi Alireza; Tanaseichuk Olga; Benner Christopher; Chanda Sumit. Metascape Provides a Biologist-Oriented Resource for the Analysis of Systems-Level Datasets. *Nature Communications* **2019**, *10* (1), 1523. https://doi.org/10.1038/s41467-019-09234-6.

(66) Langfelder, P.; Horvath, S. WGCNA: An R Package for Weighted Correlation Network Analysis. *BMC Bioinformatics* **2008**, 559. https://doi.org/10.1186/1471-2105-9-559.

(67) Subramanian, A.; Kuehn, H.; Gould, J.; Tamayo, P.; Mesirov, J. P. GSEA-P: A Desktop Application for Gene Set Enrichment Analysis. *Bioinformatics* **2007**, No. 23, 3251–3253. https://doi.org/10.1093/bioinformatics/btm369.

(68) Fleming, D. S.; Miller, L. C. Leading Edge Analysis of Transcriptomic Changes during Pseudorabies Virus Infection. *Genom Data* **2016**, *10*, 104–106. https://doi.org/10.1016/j.gdata.2016.09.014.

(69) McDonough, J. E.; Ahangari, F.; Li, Q.; Jain, S.; Verleden, S. E.; Herazo-Maya, J.; Vukmirovic, M.; DeIuliis, G.; Tzouvelekis, A.; Tanabe, N.; et al. Transcriptional Regulatory Model of Fibrosis Progression in the Human Lung. *JCI Insight* **2019**, *4* (22). https://doi.org/10.1172/jci.insight.131597.

(70) DePianto, D. J. Heterogeneous Gene Expression Signatures Correspond to Distinct Lung Pathologies and Biomarkers of Disease Severity in Idiopathic Pulmonary Fibrosis. *Thorax* **prepub**. https://doi.org/10.1136/thoraxjnl-2013-204596.

(71) Meltzer, E. Bayesian Probit Regression Model for the Diagnosis of Pulmonary Fibrosis: Proof-of-Principle. *BMC Med Genomics* **2011**, *4*, 1–13. https://doi.org/10.1186/1755-8794-4-70.

(72) Yang, I. V.; Coldren, C. D.; Leach, S. M.; Seibold, M. A.; Murphy, E.; Lin, J.; Rosen, R.; Neidermyer, A. J.; McKean, D. F.; Groshong, S. D.; et al. Expression of Cilium-Associated Genes Defines Novel Molecular Subtypes of Idiopathic Pulmonary Fibrosis. *Thorax* **2013**, *68* (12), 1114–1121. https://doi.org/10.1136/thoraxjnl-2012-202943.

(73) Luzina; Salcedo; Rojas-Peña; Wyman; Galvin; Sachdeva; Clerman; Kim; Franks; Britt; et al. Transcriptomic Evidence of Immune Activation in Macroscopically Normal-Appearing and Scarred Lung Tissues in Idiopathic Pulmonary Fibrosis. *Cell Immunol* **2018**, *325*, 1–13. https://doi.org/10.1016/j.cellimm.2018.01.002.

(74) Steele, M. Relationship between Gene Expression and Lung Function in Idiopathic Interstitial Pneumonias. *BMC Genomics* **2015**, *16*, 104–115. https://doi.org/10.1186/S12864-015-2102-

3.

(75)   Yang, I. V.; Burch, L. H.; Steele, M. P.; Savov, J. D.; Hollingsworth, J. W.; McElvania-Tekippe, E.; Berman, K. G.; Speer, M. C.; Sporn, T. A.; Brown, K. K.; et al. Gene Expression Profiling of Familial and Sporadic Interstitial Pneumonia. *Am J Respir Crit Care Med* **2007**, *175* (1), 45–54. https://doi.org/10.1164/rccm.200601-062OC.

(76)   Nance, T. Transcriptome Analysis Reveals Differential Splicing Events in IPF Lung Tissue. *PLoS One* **2014**, *9* (3), 878–892. https://doi.org/10.1371/JOURNAL.PONE.0092111.

(77)   Gangwar, I.; Kumar Sharma, N.; Panzade, G.; Awasthi, S.; Agrawal, A.; Shankar, R. Detecting the Molecular System Signatures of Idiopathic Pulmonary Fibrosis through Integrated Genomic Analysis. *Sci Rep* **2017**, *7* (1). https://doi.org/10.1038/s41598-017-01765-6.

(78)   Ruscitti, F.; Ravanetti, F.; Essers, J.; Ridwan, Y.; Belenkov, S.; Vos, W.; Ferreira, F.; KleinJan, A.; van Heijningen, P.; Van Holsbeke, C.; et al. Longitudinal Assessment of Bleomycin-Induced Lung Fibrosis by Micro-CT Correlates with Histological Evaluation in Mice. *Multidisciplinary Respiratory Medicine* **2017**, *12*, 8. https://doi.org/10.1186/s40248-017-0089-0.

(79)   Talbot, S. R.; Biernot, S.; Bleich, A.; van Dijk, R. M.; Ernst, L.; Häger, C.; Helgers, S. O. A.; Koegel, B.; Koska, I.; Kuhla, A.; et al. Defining Body-Weight Reduction as a Humane Endpoint: A Critical Appraisal. *Lab Anim* **2020**, *54* (1), 99–110. https://doi.org/10.1177/0023677219883319.

(80)   Cowley, P. M.; Roberts, C. R.; Baker, A. J. Monitoring the Health Status of Mice with Bleomycin-Induced Lung Injury by Using Body Condition Scoring. *Comp Med* **2019**, *69* (2), 95–102. https://doi.org/10.30802/AALAS-CM-18-000060.

(81)   Robbe, A.; Tassin, A.; Carpentier, J.; Declèves, A.-E.; Mekinda Ngono, Z. L.; Nonclercq, D.; Legrand, A. Intratracheal Bleomycin Aerosolization: The Best Route of Administration for a Scalable and Homogeneous Pulmonary Fibrosis Rat Model? *BioMed Research International* **2015**, *2015*, 198418. https://doi.org/10.1155/2015/198418.

(82)   Abidi, A.; Bahri, S.; Ben Khamsa, S.; Legrand, A. A Comparative Study of Intratracheal and Aerosolization Instillations of Bleomycin Inducing Experimental Lung Fibrosis in Rat. *Toxicol Mech Methods* **2019**, *29* (2), 75–85. https://doi.org/10.1080/15376516.2018.1512181.

(83)   Giri, S. N.; Hyde, D. M.; Nakashima, J. M. Analysis of Bronchoalveolar Lavage Fluid from Bleomycin-Induced Pulmonary Fibrosis in Hamsters. *Toxicol Pathol* **1986**, *14* (2), 149–157. https://doi.org/10.1177/019262338601400202.

(84)   Thrall, R. S.; Barton, R. W. A Comparison of Lymphocyte Populations in Lung Tissue and in Bronchoalveolar Lavage Fluid of Rats at Various Times during the Development of Bleomycin-Induced Pulmonary Fibrosis. *Am Rev Respir Dis* **1984**, *129* (2), 279–283.

(85)   Hao, H.; Cohen, D. A.; Jennings, C. D.; Bryson, J. S.; Kaplan, A. M. Bleomycin-Induced Pulmonary Fibrosis Is Independent of Eosinophils. *J Leukoc Biol* **2000**, *68* (4), 515–521.

(86)   Sato, E.; Koyama, S.; Robbins, R. A. Bleomycin Stimulates Lung Fibroblast and Epithelial Cell Lines to Release Eosinophil Chemotactic Activity. *Eur Respir J* **2000**, *16* (5), 951–958.

(87)   Nelson, D. L. and C. *Lehninger's Principles of Biochemistry*, 4th ed.; W. H. Freeman and Company, Ed.

(88)   Izbicki, G.; Segel, M. J.; Christensen, T. G.; Conner, M. W.; Breuer, R. Time Course of Bleomycin-induced Lung Fibrosis. *International Journal of Experimental Pathology* **2002**, *83* (3), 111–119. https://doi.org/10.1046/j.1365-2613.2002.00220.x.

(89)   Chaudhary, N. I.; Schnapp, A.; Park, J. E. Pharmacologic Differentiation of Inflammation and Fibrosis in the Rat Bleomycin Model. *Am J Respir Crit Care Med* **2006**, *173* (7), 769–776. https://doi.org/10.1164/rccm.200505-717OC.

(90)   Schiller, H. Time- and Compartment-Resolved Proteome Profiling of the Extracellular Niche in Lung Injury and Repair. *Mol Syst Biol* **2015**, *11* (7), 63–81.

https://doi.org/10.15252/MSB.20156123.

(91) Moore, B. B.; Hogaboam, C. M. Murine Models of Pulmonary Fibrosis. *Am J Physiol Lung Cell Mol Physiol* **2008**, *294* (2), L152–L160. https://doi.org/10.1152/ajplung.00313.2007.

(92) Ridley, A. J.; Hall, A. The Small GTP-Binding Protein Rho Regulates the Assembly of Focal Adhesions and Actin Stress Fibers in Response to Growth Factors. *Trends Cell Biol* **1992**, *2* (11), 324. https://doi.org/10.1016/0962-8924(92)90173-K.

(93) Sandbo, N.; Lau, A.; Kach, J.; Ngam, C.; Yau, D.; Dulin, N. O. Delayed Stress Fiber Formation Mediates Pulmonary Myofibroblast Differentiation in Response to TGF-. *Am J Physiol Lung Cell Mol Physiol* **2011**, *301* (5), L656–L666. https://doi.org/10.1152/AJPLUNG.00166.2011.

(94) Gui, X.; Qiu, X.; Xie, M.; Tian, Y.; Min, C.; Huang, M.; Hongyan, W.; Chen, T.; Zhang, X.; Chen, J.; et al. Prognostic Value of Serum Osteopontin in Acute Exacerbation of Idiopathic Pulmonary Fibrosis. *BioMed Research International* **2020**, *2020*, 3424208. https://doi.org/10.1155/2020/3424208.

(95) Koli, K.; Myllärniemi, M.; Vuorinen, K.; Salmenkivi, K.; Ryynänen, M. J.; Kinnula, V. L.; Keski-Oja, J. Bone Morphogenetic Protein-4 Inhibitor Gremlin Is Overexpressed in Idiopathic Pulmonary Fibrosis. *Am J Pathol* **2006**, *169* (1), 61–71. https://doi.org/10.2353/ajpath.2006.051263.

(96) Shichino, S.; Abe, J.; Ueha, S.; Otsuji, M.; Tsukui, T.; Kosugi-Kanaya, M.; Shand, F. H. W.; Hashimoto, S.; Suzuki, H. I.; Morikawa, T.; et al. Reduced Supply of Monocyte-Derived Macrophages Leads to a Transition from Nodular to Diffuse Lesions and Tissue Cell Activation in Silica-Induced Pulmonary Fibrosis in Mice. *Am J Pathol* **2015**, *185* (11), 2923–2938. https://doi.org/10.1016/j.ajpath.2015.07.013.

(97) Bonniaud, P.; Fabre, A.; Frossard, N.; Guignabert, C.; Inman, M.; Kuebler, W. M.; Maes, T.; Shi, W.; Stampfli, M.; Uhlig, S.; et al. Optimising Experimental Research in Respiratory Diseases: An ERS Statement. *Eur Respir J* **2018**, *51* (5), 1702133. https://doi.org/10.1183/13993003.02133-2017.

(98) Myllärniemi, M.; Kaarteenaho, R. Pharmacological Treatment of Idiopathic Pulmonary Fibrosis – Preclinical and Clinical Studies of Pirfenidone, Nintedanib, and N-Acetylcysteine. *Eur Clin Respir J* **2015**, *2* (1). https://doi.org/10.3402/ecrj.v2.26385.

(99) Richeldi, L.; du Bois, R. M.; Raghu, G.; Azuma, A.; Brown, K. K.; Costabel, U.; Cottin, V.; Flaherty, K. R.; Hansell, D. M.; Inoue, Y.; et al. Efficacy and Safety of Nintedanib in Idiopathic Pulmonary Fibrosis. *N Engl J Med* **2014**, *370* (22), 2071–2082. https://doi.org/10.1056/NEJMoa1402584.

(100) Surber; Beck; Pham; Marsden; Gandi; Baily; McElroy. Inhaled Nintedanib Is Well-Tolerated and Delivers Key Pharmacokinetic Parameters Required to Treat Bleomycin-Induced Pulmonary Fibrosis. *Pulm Pharmacol Ther* **2020**, *63*. https://doi.org/10.1016/j.pupt.2020.101938.

(101) Gilhodes, J.-C.; Julé, Y.; Kreuz, S.; Stierstorfer, B.; Stiller, D.; Wollin, L. Quantification of Pulmonary Fibrosis in a Bleomycin Mouse Model Using Automated Histological Image Analysis. *PLoS One* **2017**, *12* (1), E170561. https://doi.org/10.1371/journal.pone.0170561.

(102) Wollin, L.; Maillet, I.; Quesniaux, V.; Holweg, A.; Ryffel, B. Antifibrotic and Anti-Inflammatory Activity of the Tyrosine Kinase Inhibitor Nintedanib in Experimental Models of Lung Fibrosis<inline-Graphic Xmlns:Xlink="http://Www.W3.Org/1999/Xlink" Href="sbox" Xlink:Type="simple"/>. *J Pharmacol Exp Ther* **2014**, *349* (2). https://doi.org/10.1124/jpet.113.208223.

(103) Sheu, C.-C.; Chang, W.-A.; Tsai, M.-J.; Liao, S.-H.; Chong, I.-W.; Kuo, P.-L. Gene Expression Changes Associated with Nintedanib Treatment in Idiopathic Pulmonary Fibrosis Fibroblasts: A Next-Generation Sequencing and Bioinformatics Study. *J Clin Med* **2019**, *8* (3).

https://doi.org/10.3390/jcm8030308.

(104) Zank, D. C.; Bueno, M.; Mora, A. L.; Rojas, M. Idiopathic Pulmonary Fibrosis: Aging, Mitochondrial Dysfunction, and Cellular Bioenergetics. *Front Med (Lausanne)* **2018**, *5*, 10. https://doi.org/10.3389/fmed.2018.00010.

(105) Rangarajan, S.; Bernard, K.; Thannickal, V. J. Mitochondrial Dysfunction in Pulmonary Fibrosis. *Ann Am Thorac Soc* **2017**, *14* (Suppl), S383–S388. https://doi.org/10.1513/AnnalsATS.201705-370AW.

(106) Boxhammer, E.; Lehle, K.; Schmid, C.; von Suesskind-Schwendi, M. Anti-Oxidative Effect of the Tyrosine Kinase Inhibitor Nintedanib: A Potential Therapy for Chronic Lung Allograft Dysfunction? *Experimental Lung Research* **2020**, *46* (5), 128–145. https://doi.org/10.1080/01902148.2020.1738594.

(107) Emblom-Callahan, M. C.; Chhina, M. K.; Shlobin, O. A.; Ahmad, S.; Reese, E. S.; Iyer, E. P. R.; Cox, D. N.; Brenner, R.; Burton, N. A.; Grant, G. M.; et al. Genomic Phenotype of Non-Cultured Pulmonary Fibroblasts in Idiopathic Pulmonary Fibrosis. *Genomics* **2010**, *96* (3), 134–145. https://doi.org/10.1016/j.ygeno.2010.04.005.

(108) Wollin, L.; Wex, E.; Pautsch, A.; Schnapp, G.; Hostettler, K. E.; Stowasser, S.; Kolb, M. Mode of Action of Nintedanib in the Treatment of Idiopathic Pulmonary Fibrosis. *Eur Respir J* **2015**, *45* (5), 1434–1445. https://doi.org/10.1183/09031936.00174914.

(109) Warburton, D.; Bellusci, S.; Del Moral, P.-M.; Kaartinen, V.; Lee, M.; Tefft, D.; Shi, W. Growth Factor Signaling in Lung Morphogenetic Centers: Automaticity, Stereotypy and Symmetry. *Respir Res* **2003**, *4*, 5. https://doi.org/10.1186/1465-9921-4-5.

(110) Mecozzi, L.; Mambrini, M.; Ruscitti, F.; Ferrini, E.; Ciccimarra, R.; Ravanetti, F.; Sverzellati, N.; Silva, M.; Ruffini, L.; Belenkov, S.; et al. In-Vivo Lung Fibrosis Staging in a Bleomycin-Mouse Model: A New Micro-CT Guided Densitometric Approach. *Sci Rep* **2020**, *10* (1), 18735. https://doi.org/10.1038/s41598-020-71293-3.

(111) Sato, N.; Takasaka, N.; Yoshida, M.; Tsubouchi, K.; Minagawa, S.; Araya, J.; Saito, N.; Fujita, Y.; Kurita, Y.; Kobayashi, K.; et al. Metformin Attenuates Lung Fibrosis Development via NOX4 Suppression. *Respir Res* **2016**, *17* (1). https://doi.org/10.1186/s12931-016-0420-x.

(112) Conforti, F.; Davies, E. R.; Calderwood, C. J.; Thatcher, T. H.; Jones, M. G.; Smart, D. E.; Mahajan, S.; Alzetani, A.; Havelock, T.; Maher, T. M.; et al. The Histone Deacetylase Inhibitor, Romidepsin, as a Potential Treatment for Pulmonary Fibrosis. *Oncotarget* **2017**, *8* (30), 48737–48754. https://doi.org/10.18632/oncotarget.17114.